The Development of Orogenic Plateaus: Case Studies Examining Relationships between Tectonics, Crustal Strength, Surface Deformation, and Plateau Morphology

By

Kristen Lee Cook
B.S., Geology, California Institute of Technology

Submitted to the Department of Earth, Atmospheric, and Planetary Sciences, in partial fulfillment of the requirements for the degree of

Doctor of Philosophy

at the

MASSACHUSETTS INSTITUTE OF TECHNOLOGY

September 2008

Signature of Author: _____
Geology, Department of Earth, Atmospheric, and Planetary Sciences
August 30th, 2008

Certified by: _____
Leigh H. Royden, PhD
Professor of Geology and Geophysics
Thesis Supervisor

Accepted by: _____
Maria T. Zuber, PhD
E.A. Griswold Professor of Geophysics
Head of the Department of Earth, Atmospheric, and Planetary Sciences

The Development of Orogenic Plateaus: Case Studies Examining Relationships between Tectonics, Crustal Strength, Surface Deformation, and Plateau Morphology

By

Kristen Lee Cook

Submitted to the Department of Earth, Atmospheric, and Planetary Sciences, in partial fulfillment of the requirements for the degree of

Doctor of Philosophy

Abstract

This thesis addresses processes associated with the uplift, deformation, and erosion of orogenic plateaus. The timing and mechanisms of uplift of the Tibetan Plateau and the Altiplano are the subject of ongoing debate. Central issues include the strength of the lower crust and the role of lower crustal flow, the relative importance of continuous deformation versus block deformation, and the possibility of lithospheric delamination. The goal of this thesis is to further explore several of these issues using a combination of numerical modeling, field observations, and thermochronology. I investigate controls on the large-scale evolution of the Tibetan Plateau and the Altiplano using a new quasi-three-dimensional viscous flow model that allows for both the development of a weak lower crust and lateral and temporal viscosity variations. Modeling motivated by the Tibetan Plateau shows that lateral variations in crustal strength can have a significant effect on surface velocities throughout the plateau, as well as on the location, shape, and slope of plateau margins and the overall plateau morphology. Model results suggest that crustal strength heterogeneities may be responsible for a number of seemingly unrelated aspects of Tibetan Plateau morphology and deformation. Modeling motivated by the Altiplano explores the relationship between subduction angle, the strength of the lower crust, crustal thickening, and surface shortening in the Central Andes. Model results illustrate that lower crustal flow above regions of steep-slab subduction can redistribute material along strike and can explain discrepancies between surface shortening and crustal thickness in the northern and southern Altiplano. I address the distribution of Middle Cenozoic deformation on the eastern margin of the Tibetan Plateau by using field observations and thermochronology to document an episode of extension and constrain its timing to the Oligocene. Finally, I examine the response of a major river system to flow over an abrupt plateau margin by using topographic data, cosmogenic nuclide dating, and numerical modeling to describe the incision history of the Colorado River into the southwestern Colorado Plateau.

Thesis Supervisor: Leigh H. Royden, Professor of Geology and Geophysics

Acknowledgements

Graduate school has been a long journey, and there have been many people providing valuable assistance and support along the way. I'd like to start by thanking my advisor, Wiki Royden. I've learned a lot from Wiki over the past 5 years, and I'm grateful for her guidance and support, as well as the freedom that she's given me to explore a wide range of problems. Clark Burchfiel and Kelin Whipple have also been extremely valuable sources of guidance, and I have greatly enjoyed working with them. I'd also like to thank the rest of my current and former committee members, Brendan Meade, Ben Weiss, Rob van der Hilst and Lindy Elkins-Tanton.

My field work would not have been possible without the assistance of a number of people – my colleagues at the Chengdu Institute of Geology and Mineral Resources, Li Junmin, Yuan Sihua, and Professor Chen Zhiliang, my drivers Xiang Shifu and Wang Shifu, and my field assistants, Owen Aftreth, who hauled around a lot of samples in China and Jeanette Hagan, who did a lot of digging in the Henry Mountains. My labwork also depended on some very helpful people – Malcolm Pringle and Bill Olszewski, who steered me (and my samples) through the Ar-Ar process, and Arjun Heimsath, who let me invade his cosmogenics lab.

A big thanks goes to the real backbone of the department, the folks on the 9th floor, both for all their help and their all-around wonderfulness. Roberta and Jacqui are the first stop for questions of all kinds, or for just a great chat. Mark has been incredibly helpful through all sorts of crises, and Vicki and Carol have also been great sources of support. And of course I'll never forget the 8th floor's den mother, the indominatable Roberta Bennett-Calorio, who never stopped looking after us, and never failed to put a smile on my face.

I also want to acknowledge the funding that's supported my research – grant EAR-0003571 from the NSF Continental Dynamics Program, an NSF Graduate Student Fellowship, an MIT Presidential Fellowship, and a GSA Student Research Grant.

My fellow graduate students in EAPS have been a huge part of my time here. The support, camaraderie, and willingness to help out with pretty much anything have played a big role in seeing me through the grad school process. In particular, Einat Lev has been a great source of friendship, support, and advice. Thanks also to Will, Taylor, Joel, Kate, Amy, and the rest of the 8th/10th floor crowd.

I also need to thank all of the regulars over at the swimming pool – the Masters Swimming, Metropolo, and women's water polo crowd, who have played a big role in keeping me sane over the past five years.

Most importantly, I need to thank my family – my siblings Carrie, Jeff, and Matt, my nephews Alex and Mason and my niece Lauren (for being extremely cute and always giving me something to smile about), and especially my parents. My mom has been my biggest cheerleader and deserves a lot of credit for helping me get where I am today.

Table of Contents

Chapter 1	Introduction.....	9
Chapter 2	The role of crustal strength variations in shaping orogenic plateaus, with application to Tibet.....	19
Chapter 3	Building the central Andes through axial lower crustal flow.....	77
Chapter 4	Cenozoic extension on the eastern margin of the Tibetan Plateau.....	111
Chapter 5	Characterizing Fluvial Incision in the Colorado River System in Southern Utah: Integrating Regional Patterns and Local Rates.....	153
Chapter 6	Summary.....	203

Chapter 1

Introduction

Motivation

Large continental plateaus are among the most impressive topographic features on the planet. The Tibetan Plateau and the Altiplano together comprise an area of over 4 million km^2 with elevations above 3000 meters, while the Colorado Plateau covers a large area of the Southwestern United States. The zone of deformation associated with the Tibetan Plateau contains all of the world's top 100 highest mountains, while the Andes contain the highest mountains outside of Asia. The Grand Canyon, on the southeastern margin of the Colorado Plateau, is matched or exceeded in size by canyons carved by rivers draining the Tibetan Plateau and Altiplano.

In addition to being geographically imposing, these large plateaus are important on a number of levels. They are drained by a number of the world's major rivers, including the Yangtze River, the Yellow River, and the Indus River from Tibet and the Colorado River from the Colorado Plateau. They have a significant effect on global atmospheric circulation and the earth's climate (Molnar et al., 1993). These large plateaus are also often associated with significant seismic hazard, as was acutely illustrated by the M7.9 Sichuan earthquake in May 2008. Most importantly, from the perspective of this thesis, these regions are also prime locations for the study of continental deformation processes.

Although the three plateaus discussed in this thesis formed in very different tectonic environments - Tibetan Plateau formed in a continental collision zone, the

Altiplano formed above an ocean-continent subduction zone, while the Colorado Plateau formed in the interior of the continent, they have a number of similarities. The Altiplano, the Tibetan Plateau, and the Colorado Plateau all have regions that show a disconnect between uplift and surface shortening. Flow of a ductile middle to lower crust has been proposed as a mechanism for crust thickening in each of these plateaus (Royden, 1996; Kley and Monaldi, 1998; McQuarrie and Chase, 2000), as has an opposing view relating uplift to delamination of the mantle lithosphere (Molnar et al., 1993; Allmendinger et al., 1997; Bird, 1979).

The similarities in the debates over the uplift these very different plateaus suggests that continental plateaus are governed by a common set of processes, regardless of their tectonic setting. At the same time, the magnitude of these features and the extensive deformation associated with them ensure that numerous factors, such as preexisting structures and variations in crustal properties, mantle dynamics, and local and far-field plate dynamics, have influenced plateau uplift, deformation, and erosion. In this thesis, I use a series of case studies, involving the Tibetan Plateau, the Altiplano, and the Colorado Plateau, to investigate controls on plateau development on scales ranging from an entire collision zone to a single river system. General questions I address include: How does crustal strength affect the partitioning of deformation both vertically and laterally in the crust? What factors control the large-scale distribution of crustal strength? How is deformation distributed in the foreland of a propagating plateau? Is deformation best described as continuous or discrete, or a combination of the two? How does rock strength and erodibility influence river incision across plateau margins? Each of the case

studies was conceived and carried out as a separate project, and each of the following chapters is intended to stand alone as an independent paper.

Chapters two through five – the case studies

In chapter two, I look at the large-scale effects of crustal strength variations on the morphology and dynamics of collisional plateaus. This study uses a semi-analytical viscous flow model that allows us to explore the effects of lateral variations in crustal strength on the development of a plateau with a weak lower crust. Our interest in lateral strength variations is motivated by the Tibetan plateau and the wide variations in the morphology of the plateau margins, particulary the juxtaposition of the extremely steep margin adjacent to the Sichuan Basin and the long-wavelength gently sloping southeastern margin.

A number of modeling studies have shown that vertical variation in crustal rheology (such as a weak lower crust) can significantly affect the transport of material and pattern of deformation in a collisional setting such as the Tibetan Plateau. Lateral variations in crustal strength are also likely to have an importance influence on orogen and plateau development. The effects of lateral heterogeneity may range from determining the shape and slope of plateau margins, to enabling the maintenance of regions of dynamic topography, to influencing the movement of crustal material throughout much of the orogen.

Chapter two describes the model that I have developed and the effects of irregular distributions of crustal strength on aspects of collisional orogens such as patterns of surface deformation, flow in the lower crust, topography, and uplift history. Model results

indicate that crustal strength variations have a dramatic effect on the morphology and dynamics of a developing plateau. Regions of strong crust correspond to steep margins and act as obstructions to the propagating plateau, causing flow of both the upper and lower crust to be diverted around the strong region. Regions of initially weak crust, on the other hand, result in gently sloping margins that propagate rapidly and divert materiel from the rest of the plateau towards the weak zone.

I also discuss the application of our model to the Tibetan Plateau and propose a relationship between a number of features of the plateau and crustal strength variations. With a relatively simple distribution of strength variations, corresponding to strong Tarim and Sichuan Basin crust and a weak southeastern corner, the model produces a plateau with many similarities to the Tibetan Plateau, including the overall morphology, rotation around the eastern syntaxis, and E-W extension. This remarkable similarity, in spite of the simplicity of the model, suggests that lateral strength variations have indeed played a fundamental role in the development of the Tibetan Plateau. Analysis of model results also suggests that E-W extension of the central plateau may be related to the rapid eastward flow of crustal material into a weak zone in the SE corner without significant change in plateau elevation. This manuscript is currently in press at the *Journal of Geophysical Research.*

In chapter three, I explore the possible role of lower crustal flow in transporting material along strike in the Andes. This study was motivated by the remarkable symmetry of the Central Andes. This symmetry is independent of along-strike variations in the magnitude of upper crustal shortening, bedrock geology and precipitation, suggesting that

regional, lithospheric-scale processes control orogen topography. In addition, abrupt decreases in the width and cross-sectional area of the orogen north and south of the Altiplano-Puna region coincide with the transition from a steeply dipping subducting slab in the Central Andes to flat slab subduction in the Northern and Southern Andes. These variations in the dip of the subducting Nazca plate may relate to along strike variations in temperature and therefore strength in the lower crust.

I adapt the three-dimensional viscous flow model described in chapter two to model the development of the Central Andes. Deformation is driven by a combination of eastward motion of the subduction zone and westward underthrusting of the Brazilian Shield, and the area above the steeply dipping slab is modeled as a zone of weak lower crust. The model produces topography that is quite similar to the present morphology of the Andes, where cross-sectional area and orogen width appear to be largely independent of the amount of upper crustal shortening along a specified cross-section. The development of the Bolivian Orocline and the uplift of the Altiplano and Puna plateaus are reproduced and are accompanied by a significant component of orogen parallel flow in the lower crust. This transport may help to explain observed discrepancies between crustal shortening estimates and current crustal thickness in the regions directly to the south and north of the Altiplano. Although this is a highly simplified model, these results suggest that axial lower crustal flow is a viable means of thickening the crust of the Altiplano without commensurate surface shortening. Chapter three was written in collaboration with Dr. William Ouimet, and is currently in preparation for submission to *Earth and Planetary Science Letters.*

Chapter four moves from the model world to the field, and addresses deformation on the eastern margin of the Tibetan Plateau during the period between the initial collision of India and Eurasia at ~50 Ma and the uplift of the eastern margin at ~8-12 Ma (Clark et al., 2005; Ouimet, 2007). In this chapter, I describe zones of extensional shear bounding two structures on the eastern margin – the Gezong Dome and the Kangding Antiform, and constrain the timing of extension using $^{40}Ar/^{39}Ar$ thermochronology. The fault zones move a sequence of Paleozoic sedimentary and metasedimentary rocks down and to the northwest relative to the underlying Precambrian granitic and metamorphic rocks. Deformation on the northern boundary of the Gezong Dome was accommodated on a narrow zone of mylonite, while the structure bounding the Kangding Antiform moved from the ductile to brittle regime during extension. Biotite and muscovite $^{40}Ar/^{39}Ar$ data show that the zones of ductile shear experienced localized heating and cooling at ~30 Ma, while the rocks above and below remained below ~300°C and have $^{40}Ar/^{39}Ar$ ages ranging from ~50 to over 100 Ma. The correlation between normal-sense shear fabric and Oligocene $^{40}Ar/^{39}Ar$ ages suggests that these ages are recording the timing of extension.

The Gezong Dome and Kangding Antiform are part of a larger structure – the NW-SE trending Danba Antiform, which has uplifted Paleozoic and basement rocks relative to the surrounding Triassic flysch. Regional thermochronology data suggest that the uplift of the Danba Antiform also took place at ~30 Ma, synchronous with extension. The timing of this deformation is of particular interest because it coincides with a major change in the tectonic framework of eastern Tibet, as initiation of motion along large strike-slip shear zones began to accommodate extrusion of material out of the collision

zone (Tapponnier et al., 1982; Leloup et al., 2001; Mock et al., 1999). The extent to which the lithosphere between these large shear zones behaved as rigid blocks has been the subject of some debate, but the presence of faulting and uplift in the Danba region during this time indicates that deformation was taking place far from a major shear zone. This provides some insight into the state of eastern Tibet at this time and the extent to which extension throughout South China affected the eastern margin and contributed to the eastward extrusion.

Chapter five addresses the interaction between surface processes and continental plateaus and looks at incision of a major river, the Colorado, as it flows across an abrupt plateau margin. The Colorado River system began to incise its best-known feature, the Grand Canyon, following the integration of the drainage system over the plateau edge ~6 Ma (Lucchitta 1990). Although the carving of the Grand Canyon was largely complete by ~1 Ma, the canyon ends at Lee's Ferry, and the incision history of Colorado River system upstream of the Grand Canyon, in southern Utah and northern Arizona, has been the subject of debate. In chapter five, I use three different techniques to shed light on the evolution of the Colorado River in this region.

I first use longitudinal profiles of the Colorado and tributaries between Lee's Ferry and Cataract Canyon, and the regional distribution of local relief and slopes to identify a recent pulse of incision on the Colorado River. This incision pulse has resulted in the formation of a knickpoint in the lower reaches of almost all of the tributaries in this region. These knickpoints are of similar size, occur at similar elevations, and coincide with changes in local relief, suggesting that the tributaries are steepening in response to

an episode of increased incision on the Colorado. This analysis makes predictions about the spatial distribution of incision rates in this region that are consistent with existing rate estimates and can be used to guide further studies.

I then complement the regional analysis, with a cosmogenic nuclide study to determine the incision rate of a tributary to the Colorado in the Henry Mountains of Southern Utah. I present ^{10}Be *in situ* concentration data from a suite of four gravel covered strath surfaces elevated above a channel that drains to the Colorado River. The resulting exposure ages suggest that incision for the past ~270 m.y. has been consistently rapid through time. These high incision rates support the interpretation that tributaries of the Colorado River upstream of the Grand Canyon are responding to a recent pulse of rapid incision on the Colorado.

Finally, in order to explain how this pulse of incision relates to the evolution of the Colorado River and the Grand Canyon, and how factors such as lithologic variation modulate the response of a river to rapid baselevel fall, I use a simple numerical model of river incision. Model results suggest that variations in bedrock erodibility extert a significant control on the way that incision propagates through the system.

This manuscript is currently in review at *Earth Surface Processes and Landforms*.

References

Allmendinger, R. W., T. E. Jordan, Kay, S. M., and B. L. Isacks (1997). The evolution of the Altiplano-Puna plateau of the Central Andes. Annual Reviews of Earth and Planetary Science 25: 139-74.

Bird, P. (1979) Continental delamination and the Colorado Plateau, J. Geophys. Res., **84**, 7561-7571.

Clark, M.K., House, M.A., Royden, L.H., Burchfiel, B.C., Whipple, K.X., Zhang, X., and Tang, W., 2005, Late Cenozoic uplift of southeastern Tibet, *Geology* 33, 525-528.

Hamblin WK. 1994. Late Cenozoic lava dams in the western Grand Canyon: Geological Society of America Memoir 183, 135 p.

Kley, J. and C. R. Monaldi (1998). Tectonic shortening and crustal thickness in the Central Andes: How good is the correlation? Geology 26 (8): 723-726.

Leloup, P. H., N. Arnaud, R. Lacassin, J. R. Kienast, T. M. Harrison, T. T. Trong, A. Replumaz, and P. Tapponnier, 2001, New constraints on the structure, thermochronology, and timing of the Ailao Shan-Red River shear zone, SE Asia, *J. Geophys. Res., 106(B4),* 6683-6732.

Lucchitta, I. 1990. History of the Grand Canyon and of the Colorado River in Arizona. In *Grand Canyon Geology*, Beus, SS, Morales, M (eds). Oxford University Press: New York; 311-332.

McQuarrie, N, Chase, C.G., 2000, Raising the Colorado Plateau, *Geology* 28(1), 91–94.

Mock, C, Arnaud, N.O., Cantagrel, J.M., 1999, An early unroofing in northeastern Tibet? Constraints from $^{40}Ar/^{39}Ar$ thermochronology on granitoids from the eastern Kunlun range (Qianghai, NW China), *Earth and Planetary Science Letters* 171, 107–122.

Molnar, P., P. England, and J. Martinod (1993), Mantle dynamics, uplift of the Tibetan Plateau, and the Indian monsoon, *Rev. of Geophysics, 31(4),* 357-396.

Ouimet, W.B., 2007, *Dissecting the Eastern Margin of the Tibetan Plateau: A Study of Landslides, Erosion, and River Incision in a Transient Landscape.* Ph.D thesis, MIT, Cambridge, MA.

Royden, L. H. (1996). Coupling and decoupling of crust and mantle in convergent orogens: Implications for strain partitioning in the crust, Journal of Geophysical Research 101 (B8): 17,679-17,705.

Tapponnier, P., G. Peltzer, A. Y. Le Dain, R. Armijo, and P. Cobbold (1982), Propagating extrusion tectonics in Asia; new insights from simple experiments with plasticine, *Geology* 10(12), 611-616.

Chapter 2

The role of crustal strength variations in shaping orogenic plateaus, with application to Tibet

Kristen L. Cook and Leigh H. Royden
Department of Earth, Atmospheric and Planetary Science, Massachusetts Institute of Technology, Cambridge, MA, USA

In press at the *Journal of Geophysical Research*

Abstract

The Tibetan Plateau is the type example of a large orogenic plateau formed as a result of continent-continent collision. The morphology of the plateau and its margins suggests that pre-existing variations in crustal strength have influenced the growth of the plateau. We have developed a three-dimensional numerical model of deformation in a viscous crust in order to investigate the effects of lateral heterogeneities on plateau growth. The model includes a two layer crust and allows for lateral variation of viscosity in both the upper and lower layers. Model results indicate that crustal strength variations have a dramatic effect on the morphology and dynamics of a developing plateau. A region of strong crust is characterized by a very steep plateau margin that propagates extremely slowly, does not accommodate significant shortening strain, and is subparallel to local upper and lower crustal velocities. A weak crustal region develops a gently sloping margin; uplift propagates rapidly across the weak zone, and crustal material within the plateau is diverted towards the low-strength region. With a relatively simple distribution of strength variations, corresponding to strong Tarim and Sichuan Basin crust and a weak southeastern corner, our model produces a plateau with many similarities to the Tibetan Plateau, including the overall morphology, rotation around the eastern syntaxis, and E-W extension. Analysis of model results suggests that E-W extension of the central plateau may be related to the rapid eastward flow of crustal material into a weak zone in the SE corner without significant change in plateau elevation.

1. Introduction

Unlike oceanic plates, which tend to concentrate strain along discrete boundaries, deformation in continental crust may be distributed over areas hundreds or even thousands of kilometers wide [ie. *Molnar and Tapponnier*, 1975]. A continental deformation zone may encompass regions of crust with different compositions, histories, thermal structures, and pre-existing anisotropies. As our understanding of the basic processes of continental deformation improves and our theories become more refined, we require a better understanding of the role of crustal heterogeneity. The effects of rheologic variations in the middle and lower crust on surface topography and deformation are particularly difficult to evaluate in active orogens because the relevant processes occur at depth and must be inferred from surface observations, geophysical properties, and comparison to analogous regions of exhumed lower crust.

A prime example of active continental deformation is the vast region of Central Asia affected by the convergence of India and Eurasia. The most impressive product of post-collisional convergence is the Tibetan Plateau, which is often used to motivate and evaluate theories of continent-continent collision. Because Tibet is in an active collision zone, we can combine measurements of current surface deformation from GPS data with displacement across active structures and observation of older structures to make inferences about the topographic and tectonic evolution of the plateau and surrounding regions. Such observations, summarized in the next section, indicate that strength heterogeneities, distributed laterally and with depth in the crust and lithosphere, play an important role in defining the mode and localization of crustal deformation in and around

Tibet. This study uses numerical modeling to investigate the effects of lateral heterogeneities in the upper and lower crust on the patterns of uplift and surface deformation in collisional orogens, with application to the Tibetan Plateau.

2. Motivation – the Tibetan Plateau

2.1. Modern morphology and dynamics of the Tibetan Plateau

The uplift of the Tibetan Plateau likely initiated with the collision of India and Eurasia at approximately 50 Ma [*Dewey et al.*, 1988; *Zhu et al.*, 2005; *Guillot et al.*, 2003; *Rowley*, 1996], although some parts of the region may have been moderately elevated as an Andean-type margin prior to collision [*Murphy*, 1997]. The modern plateau is characterized by a high elevation and extremely low-relief landscape that slopes gently from west to east [*Fielding et al.,* 1994]. Convergence and deformation continue today, but the mechanisms and timing of uplift and deformation remain controversial and a wide variety of end-member theories have been proposed to describe the development of the plateau, including extrusion of rigid blocks [*Molnar and Tapponnier*, 1975], underplating [*Powell*, 1986] or injection of Indian crust [*Zhao and Morgan*, 1987], distributed crustal thickening [*England and Houseman*, 1986], lithospheric delamination [*Molnar et al.*, 1993], and lower crustal flow [*Royden*, 1996].

We focus our discussion on the period of evolution between ~12 Ma and the present, when the patterns and timing of deformation are better known than for older time periods, and the uplift of the peripheral regions of the plateau can be reasonably well constrained. Within the central plateau, deformation since Pliocene or perhaps late Miocene time has been characterized by roughly E-W trending strike-slip faults and N-S

trending extensional grabens (Fig. 1) [*Dewey* 1988]. It appears that much of the uplift of the central plateau may be Early Cenozoic [*Rowley and Currie*, 2006], while Late Cenozoic uplift and crustal thickening have been focused preferentially around the northern and eastern margins of the plateau [*Dewey* 1988]. The relationships between Late Cenozoic deformation, plateau morphology, and older geologic structures vary widely in different regions of the plateau, as described below.

The Tibetan Plateau is bounded on the north and south by steep, well-defined margins. On the southern plateau margin, the Himalayas absorb almost half of the total active convergence between India and Eurasia along a large north-dipping thrust system [*Zhang et al.*, 2004]. The steep topography in the region is a reflection of the active shortening and deformation along the margin and the relatively strong character of the underlying crust. The convergence direction between points in southern Tibet and in the Indian craton is essentially perpendicular to the mountain front. Although the rate of denudation is very high along the Himalayan margin of the plateau, exhumation seems to be in balance with crustal shortening, and the elevation of this region may not have changed greatly since the middle Miocene [e.g., *Hodges*, 2000].

In contrast to the active shortening along the southern margin , the steep northern margin of the Tibetan plateau parallels the left-lateral Altyn Tagh Fault. The dominant mode of surface deformation along this margin is left-lateral strike slip with only a small component of convergence [*Yue et al.*, 2001; *Tapponnier et al.,* 2001; *Zhang et al.*, 2004]. Thrust faults associated with the Altyn Tagh Fault are oriented oblique to the plateau margin [i.e., *Tapponnier et al.,* 2001] and GPS data indicate little convergence perpendicular to the margin [*Zhang et al.*, 2004]. Only at the eastern and western ends of

the Altyn Tagh Fault, in the Qilian Shan and West Kunlun Shan, is there significant margin-perpendicular shortening [i.e., *Chen et al.*, 1999; *Cowgill et al.*, 2003]. The steep northern plateau margin appears to coincide spatially with the transition between the more rigid crust of the Tarim block [*Reigber et al.*, 2001] and the more rapidly deforming crustal terranes to the south.

To the west, the plateau narrows considerably before merging into the Karakoram and Pamir ranges southwest of the Karakoram Fault. During Late Cenozoic time, deformation spread northwest of the Tarim Basin into the Tien Shan range, which began to rise around 10-11 Ma [*Bullen et al.*, 2003]. The Tien Shan currently absorbs as much as 13 mm/yr convergence, nearly one third of the convergence rate between India and Eurasia [*Abdrakhmatov et al.*, 1996]. The Tien Shan region experienced several episodes of deformation during Paleozoic collision events [*Bullen et al.*, 2001; *Windley et al.*, 1990], and the current localization of convergent deformation in the range appears to be related to the pre-Cenozoic structure of the region.

The eastern plateau margin encompasses a gently sloping, long-wavelength margin in the southeast, an extremely steep boundary between the plateau and the Sichuan Basin, and another gently sloping region north of the Sichuan Basin. Low temperature thermochronology studies [*Clark et al.*, 2005b; *Ouimet et al.*, 2006] and the presence of an intact low-relief relict landscape draping the gently-dipping southeastern margin indicate that the southeastern margin has experienced little to no surface shortening or exhumation [*Clark et al.*, 2005b]. Pliocene-Quaternary deformation in eastern Tibet is dominated by left-lateral strike-slip faults that cut across both the topographic gradient of the margin and the trend of older structures. Shortening structures

of both Mesozoic and Cenozoic age trend oblique or perpendicular to the plateau margin [*Burchfiel et al.*, 1995; *Wang et al.*, 1998].

The steep margin adjacent to the Sichuan basin appears to have uplifted in the past 5-12 Ma with only minor upper crustal shortening [*Kirby et al.*, 2002; *Burchfiel et al.*,1995]. In contrast to the high elevation regions of the central and eastern plateau, and to the gently dipping margin of the southeastern plateau, the location of this margin corresponds to older structures related to the furthest extent of deformation during the Indosinian orogeny [*Burchfiel et al.*,1995; *Chen and Wilson*, 1996], indicating an older structural control on the location of the steep topographic edge of the plateau. GPS data show that there is currently no relative motion across this topographic front [*Chen et al.*, 2000].

As the above observations illustrate, deformation styles vary widely around the margins of the plateau. In some areas, uplift and crustal thickening are well-correlated with surface structures. In other regions topography seems to have no relationship to recent surface deformation, but abrupt changes in morphology correspond to older structures or terrane boundaries. This contrast may be related to the relative importance of upper crustal and lower crustal deformation processes, and suggests that lateral heterogeneities in the upper crust play a key role in some areas but not others. The role of lower crustal heterogeneities is more difficult to determine, but since the strength of the lower crust partly determines how stress is transmitted in the crust, variations in lower crustal strength have an important influence on both surface deformation and the growth of topography.

2.2. Lower crustal flow in Tibet

Lower crustal flow has been proposed to occur throughout the Tibetan plateau [*Bird*, 1991; *Royden*, 1996; *Beaumont et al.*, 2001; *Vanderhaeghe and Teyssier*, 2001]. High temperatures and/or the presence of even small amounts of fluids or partial melt can greatly reduce the strength of continental crust [*Rosenberg and Handy*, 2005; *Kohlstedt et al.*, 1995], allowing ductile flow in the middle to lower crust in response to pressure gradients resulting from topography. This enables a lateral flux of material throughout the plateau with minimal deformation of the upper crustal layer. An important consequence of a weak lower crust is that it results in local decoupling between the mantle and the upper crust, and significantly reduces the transmission of stresses through the weak layer. Thus, the recognition of lower crustal flow in an orogenic setting may be extremely important in the interpretation of large-scale deformation based on surface observations.

A number of geophysical observations point to the presence of fluids or partial melt in the middle or lower crust of southern Tibet [*Brown et al.*, 1996; *Nelson et al.*, 1996; *Ross et al.*, 2004; *Wei et al.*, 2001]. Other studies indicate significant crustal anisotropy and thinning of the lower crust through lateral flow in central and northern Tibet [*Haines et al.*, 2003; *Ozacar and Zandt*, 2004; *Shapiro et al.*, 2004]. The crust beneath the southeastern margin has slow P-wave velocities [*Li et al.*, 2006] and high heat flow values [*Wang*, 2001]. Recent teleseismic receiver function analysis indicates the presence of a midcrustal low velocity zone extending from the thick crust of western Sichuan Province south through the thinner crust of Yunnan [*Xu et al.*, 2007].

In contrast, the Sichuan Basin has been interpreted as region of strong lithosphere [*Clark et al.*, 2005a], consistent with fast seismic velocities down to 200km depth [*Li et*

al., 2006] and low heat flow measurements [*Wang,* 2001]. The Sichuan Basin sits atop cratonic crust of the Yangtze platform and has remained largely undeformed throughout both the Mesozoic Indosinian orogeny and the current Tibetan deformation [*Burchfiel et al.*, 1995]. The Tarim Basin also behaves as a rigid undeforming block [*Zhang et al.*, 2004], and has long been regarded as a region of strong lithosphere [*Vilotte et al.*, 1984; *England and Houseman*, 1985; *Dewey et al.*, 1988].

3. Modeling

3.1 Previous modeling studies

Because the behavior of the lower crust cannot be directly observed, evidence for or against lower crustal flow in an active orogen must be obtained indirectly from observable geophysical parameters, by drawing from studies of exhumed lower crust [ie. *Vanderhaeghe et al.*, 1999a; *Vanderhaeghe et al.*, 1999b; *Bouhallier et al.*, 1995], and through observations of its effects on surface deformation and morphology. Theoretical modeling proves useful in predicting what these effects may be, and thus in generating hypotheses that can be tested by geological and geophysical observations. Early studies [*Vilotte et al.*, 1984; *England and Houseman*, 1985] suggested that the presence of a rigid block approximating the Tarim Basin will have a significant effect on the development of a collisional orogen in a vertically homogeneous crust.

Several analytical and numerical models address lower crustal flow in the context of plateau development [*Royden*, 1996; *Shen et al.*, 2001; *Vanderhaeghe et al.,* 2003, *Jamieson et al.*, 2002; *Medvedev and Beaumont*, 2006; *Beaumont et al.*, 2006; *Jamieson et al.*, 2007]; however, these models do not allow for two-dimensional lateral variations

in crustal viscosity. *Clark and Royden* [2000] focused on the eastern margin and used a one dimensional model of channel flow to explore the relationship between crustal strength and margin steepness. *Clark et al.* [2005a] related channel flow against a rigid cylinder to the dynamic topography observed between the Longmen Shan and the Sichuan Basin.

These results suggest that there are important links between morphology, deformation style and crustal rheology, and highlight the need for a treatment of the role of both vertical and lateral crustal heterogeneities in plateau development. The modeling results, along with the correlation, described above, of older structures with steep boundaries imply that rheologic variations have almost certainly played an important role in locally shaping the eastern and northern plateau margins, but the extent to which blocks such as the Sichuan and Tarim Basins may have affected deformation throughout the rest of the plateau is unclear.

3.2 Model development

We follow the general approach of *Royden* [1996], *Royden et al.* [1997] and *Shen et al.* [2001] and model continuous crustal deformation using a simple rheology and relatively few parameters. The crustal flow model developed here treats the crust as an idealized incompressible Newtonian viscous fluid with two layers representing the upper and lower crust. Viscosity is allowed to vary laterally in both the upper and lower crust, but within each layer viscosity is invariant with depth (Fig. 2). The incorporation of lateral viscosity variations enables the model to evaluate the effects of particularly strong or weak areas on the evolution of topography. External forcing is provided by a

horizontal velocity imposed on the base of the crust, and crustal thickness evolves in response to a competition between gravity and the assigned basal velocity.

We do not model the thermal state of the crust or relate viscosity to temperature in the crust. The relationship between temperature and the bulk strength of the crust is not straightforward, and explicit modeling requires many assumptions about the composition and temperature of the lower crust, and the presence of fluids and partial melt. Using a 2D coupled thermal-mechanical model, *Vanderhaeghe et al.* [2003] have shown that the large-scale topographic characteristics of an orogen are not sensitive to whether viscosity is depth-dependent or temperature-dependent, as long as the viscosity contrast between the upper and lower crust is sufficient to allow effective decoupling between the upper crust and mantle. Thus, our simple method of assigning viscosities should be sufficient to capture the large-scale behavior of the system.

The use of a Newtonian viscous rheology allows the system to be fully described by the Stokes and continuity equations. With the appropriate assumptions and boundary conditions, the Stokes and continuity equations can be solved analytically to obtain expressions for the change in crustal thickness with time and the velocities of the surface of the crust, as shown in Appendix A.

We assume that the crust is always in pointwise isostatic equilibrium, so that topography is fully compensated and scales linearly with crustal thickness, and that the lateral extent of the features of interest is much greater than the crustal thickness. We impose the following boundary conditions: 1) Horizontal shear stresses are zero at the surface. 2) The gradient in vertical stress at the surface is proportional to the topographic gradient. 3) Shear and normal velocities, shear stress, and normal stress are continuous

across the interface between the upper and lower crust. 4) Horizontal velocities at the base of the crust are imposed on the model and correspond to plate like "mantle" velocities.

In Appendix A, we derive equations for the surface velocities u_s, v_s, and the rate of change in crustal thickness $\partial h/\partial t$. These are solved to compute crustal thickness and surface velocity as a function of time, which can later be used to determine the velocity field at any depth in the crust. We solve the equations simultaneously using an implicit finite difference technique on a two-dimensional fixed grid. The models presented here use a grid spacing of 20 km and timestep of 0.01 m.y. Models run with smaller grid spacing (10 km) and timesteps (0.0025 m.y.) produced indistinguishable results.

3.2.1 Model parameters

This model incorporates a relatively small number of independent parameters. These include the viscosity of the upper and lower layers as a function of position, the initial distribution of crustal thicknesses, the thickness of the upper layer, and the velocity imposed at the base of the crust. Several additional parameters are introduced by a series of rules, described below, that we use to control the viscosity evolution of the lower crust. The small number of free parameters accorded by the adoption of a simplified rheology enables better understanding of the role that each parameter plays in the model.

3.2.2 Viscosity criteria

Since we do not calculate viscosity based on the temperature distribution in the crust, we need to establish criteria that allow the viscosity to change with time in the lower crust. The viscosity of the upper crust remains constant with time. The method described below is only one possible way of assigning viscosities in the general

formulation of this model. Any number of other rules governing viscosity could be applied, but we found the following to be the simplest and most effective method.

In the models presented here, the viscosity is initially uniform with depth over the entire crust and differentiation of a weak lower crust does not appear until some crustal thickening has taken place. Because a weak lower crust is unable to support steep slopes and inhibits further uplift and crustal thickening, the lower layer must have some initial strength or a region of high topography can not develop. We use a critical thickness parameter (h_{crit+}) that controls the onset of weakening in the lower crust and may vary in space and time. When the total crustal thickness at any point reaches this critical thickness value, viscosity in the lower layer at that point is reduced gradually until it reaches the prescribed minimum viscosity. The decrease in viscosity is linear with time and does not depend on further increase in crustal thickness. A gradual weakening of the lower crust promotes stability by ensuring that the lower crust beneath steep topographic gradients retains some strength.

This method of weakening the lower crust simulates a time lag between crustal thickening and heating due to enhanced concentration of radiogenic isotopes and the possible introduction of fluids or partial melt. The timescale of lower crustal weakening has an important effect on the timing of plateau formation and the rate of plateau propagation, as a longer time lag will delay the transition to a plateau and will slow the propagation of the plateau margins. Studies of the thermal evolution of collisional orogens and plateaus suggest that appropriate timescales for heating and thermal weakening of the lower crust typically range from 10 to 20 m.y. [Vanderhaeghe et al., 2003; Medvedev and Beaumont, 2006; Huerta et al., 1998]. Factors such as the initial

temperature of the lower crust, the rate of heat production, the amount of water in the crust, and presence of partial melt will have a significant effect on the evolution of lower crustal strength in response to thickening and heating. The timescale that we use for lower crustal weakening begins only after the crust has reached $hcrit_+$, and therefore reflects only the latest stages in the evolution of the lower crust. Although the rate of crustal thickening in the modeled plateaus varies with position relative to the suture, the total timescale for crustal thickening and lower crustal weakening generally falls within the 10-20 m.y. range (except for the regions that are weak prior to uplift described in section 4.2.2).

A reverse technique for stabilizing the lower crust is also used. If crustal thickness decreases below h_{crit+} by more than a kilometer, viscosity in the lower crust is gradually increased until either the crust thickens again, or the lower layer viscosity has returned to its initial value. The values we use for the critical thickness parameter are selected to yield crustal thicknesses and plateau elevations similar to Tibet.

Values used for viscosity and thickness of the lower crust are similar to those of earlier modeling studies [*Clark and Royden*, 2000; *Shen et al.*, 2001] that match modeled topography to Tibet with a viscosity of 10^{21} Pa s in the upper crust and 10^{18} Pa s in a 15 km thick lower crust. These values are consistent with estimates of lower crustal viscosity from a number of actively deforming regions. *Kaufman and Royden* [1994] estimate that the maximum lower crust viscosity in Basin and Range Province is 10^{19} Pa s for a 10km thick channel. Independent estimates of lower crustal viscosity of Rhenish Massif in western Germany give effective viscosity around 10^{18} Pa s for a 15-20 km thick lower crust [*Westaway*, 2001, *Klein et al., 1997*]. *Vergnolle et al.* [2003] suggest a viscosity

between 10^{16} and 10^{19} in western Mongolia for a 15 km thick lower crust. When describing the strength of a layer of crust, viscosity scales with the cube of layer thickness, so estimates of lower crustal viscosity are highly dependent on the assumed thickness of the lower crust.

The appropriate viscosity for upper and lower crust in "strong" areas is not well constrained, although modeling by *Clark and Royden* [2000] suggests that the effective viscosity of the Sichuan crustal block must be several orders of magnitude greater than the viscosity of the southeastern margin. Estimates of vertically averaged viscosity from Tarim crustal block and southern China are ~10^{23} Pa s [*Flesch et al.*, 2001]. We find that as long as the viscosity used in the strong region is at least an order of magnitude greater than in the surrounding area and a weak layer is prevented from developing, the general results are not sensitive to the exact value used.

The current thickness of the Tibetan crust is well constrained [*Zhao et al.*, 2001; *Molnar* 1988], but the precollision thickness is less certain; for simplicity, we assign the crust an initial uniform thickness of 35km. The convergence velocity of India with respect to Eurasia is well known from plate motion studies [*Michel et al.*, 2000; *DeMets et al.*, 1994] to be ~50 mm/yr over the last ~40 m.y. This value was used for the velocity of a 2000 km wide "subducting plate."

4. Results

4.1 Homogenous crust

We first discuss the results when no lateral strength variations are present (Fig 3): this will provide a basis for comparison to cases with a laterally-heterogeneous crust.

Convergence within a uniformly viscous crust with no weak lower layer results in a linear mountain range with an approximately triangular cross section (Fig 3a). As the range grows, width and elevation increase while retaining a similar morphology. Because we assume that a weak layer does not develop in the lower crust until a threshold crustal thickness is obtained, this morphology describes the early evolution of a convergent system within laterally homogeneous crust. During this stage, moderate shear stresses are required to generate strain in the crust at tectonically significant rates; the flanks of the orogen are able to develop relatively steep topographic gradients. Orogen development during this stage is similar to the evolution of 2D viscous wedges described by Medvedev [2002] and Vanderhaeghe et al. [2003].

This general morphology is maintained until the orogen obtains the critical crustal thickness (h_{crit+}) and the viscosity of the lower crust begins to decrease. Because the viscosity of the lower layer decreases gradually, the crust continues to thicken beyond h_{crit+} as the lower crustal viscosity drops. Eventually, the lower crustal viscosity becomes low enough that the maximum elevation of the orogen no longer increases. At this time, the orogen stops growing higher and starts spreading laterally, as a plateau begins to develop (Fig 3b). In these initial stages of plateau development, the maximum elevation of the orogen decreases, first rapidly and then more slowly, as the plateau crustal thickness again approaches the critical thickness (h_{crit+}). After these initial stages, the elevation of the plateau remains constant, the plateau continues to spread laterally and the area underlain by weak, flowing lower crust expands (Fig 3c).

The resulting plateau is quite flat above the weak layer; steep topographic gradients are only present at the margins, where the lower crust is still strong enough to

support large shear stresses at relatively low strain rates. Shortening becomes localized along the plateau margins where the lower crust is still highly viscous. Within the interior of the plateau, the low viscosity layer in the lower crust precludes the transmission of significant shear stresses through the lower crust. The lack of coupling between upper crust and mantle results in velocity profiles where the motion of the upper crust can be very different from that of the underlying mantle. Channel flow (parabolic with depth) develops in the lower layer beneath the plateau. Rapid flow in the weak lower crust can occur in response to even small topographic gradients and the velocity of the lower crustal layer can be different from the upper crustal velocity and the mantle velocity in magnitude and direction. These results are similar to those of earlier modeling studies [i.e. *Shen et al.*, 2001; *Royden et al.*, 1997; *Vanderhaeghe et al.,* 2003], despite the differences between their models and the one used here.

A plateau modeled with a laterally homogeneous crust has a number of similarities to the Tibetan plateau. The dimensions, elevation, and general shape of the modeled plateau are broadly similar to those of Tibet. In addition, the modeled surface velocities, particularly in the southern and eastern regions, are reminiscent of upper crustal motions in Tibet. However, the homogenous model cannot account for some of the distinctive characteristics of the plateau, such as the steepness and arcuate shape of portions of the eastern and northern margins and the gentle gradients across the southeastern and northeastern margins. These are regions where lateral heterogeneities in crustal rheology have likely played an important role in shaping the topography and the geometry of the plateau margin. In order to better understand the effects of such

heterogeneities, we look at how several types of lateral crustal heterogeneities affect plateau development.

4.2 Heterogeneous crust

4.2.1 Strong foreland regions

The most striking contrasts between the morphology of the Tibetan Plateau and the model results described above occur along the margins adjacent to the Tarim and Sichuan basins. *Clark and Royden* [2000] have proposed that this is due to the presence of anomalously strong crust beneath these basins. In this section we investigate the effect that regions of stronger crust embedded in the foreland lithosphere have on plateau development.

Regions of stronger crust are modeled by assigning higher viscosities to both the upper and lower crust; we begin with a high viscosity zone embedded in the foreland north of the developing plateau. As the plateau grows northward and encounters this zone of strength, there is a dramatic effect on the morphology of the plateau margin (Fig 4). In essence, the strong region acts as an obstruction to plateau propagation, controlling the position and slope of the adjacent margin. The plateau margin does not propagate across the high-viscosity region, which remains largely undeformed and experiences crustal thickening only right at the boundary of the region. The strong region is not designated as a completely rigid block and is able to deform, but the high viscosities assigned to the upper and lower crust of the strong region result in very slow strain rates, and deformation is unable to penetrate beyond the boundary of the obstruction. Instead, the flow of crust is diverted around the strong zone, causing an indentation, or concavity, in

the plateau margin. The plateau margin adjacent to the 'obstruction' is significantly steeper than all other plateau margins except the southern margin. Thus the region of anomalously strong crust shows up clearly in the morphology of the resulting plateau.

A region of anomalously strong crust located in the path of convergence also results in somewhat higher elevation in the center of the plateau. This occurs because crustal material is constricted between the obstruction caused by the strong crustal block and the incoming "plate" on the opposite side of the plateau. As deformation proceeds, the crust of the high plateau begins to propagate around the ends of the strong region, and eventually "wraps" around the obstruction, leaving the strong region as a topographic low surrounded by the high topography of the plateau (Fig 4c).

Obstruction of plateau growth by a strong crustal region can also have a significant effect on crustal velocities. Figure 4 shows that a strong crustal region in front of the convergence zone may affect the motion of the upper crust over much of the central plateau. Compared to the homogeneous case discussed above, the northward component of upper crustal velocity is greatly reduced, and upper crust is instead deflected to the east and west. Over 80% of total N-S convergence is accommodated on the southern margin; the remainder is distributed across the central plateau, and no north-south extension occurs within the upper crust of the central plateau. There is very little convergence across the boundary adjacent to the strong crustal block, and flow is largely directed parallel to the margin. The lower crust moves rapidly around the obstruction, although in some places it has a component of motion towards the plateau margin. As the plateau wraps around the obstruction, velocities remain parallel to the boundaries of the strong region, particularly in the lower crust (Fig 4d).

A high-viscosity region embedded in the foreland to the east of the convergence zone has a similar effect on the morphology of the adjacent plateau margin (Fig 5). A steep margin, concave in planform, develops adjacent to the heterogeneity, which remains as an undeformed low-lying region. Again, most of the motion in the upper crust is oriented parallel to the boundary of the obstacle and there is no convergence across the margin. Although the local effects of a high viscosity zone are not dependent on its position relative to the convergence zone, a high viscosity zone to the side of the convergence zone has a less far-reaching effect on the motion of the upper crust than an obstacle located in the path of convergence. Surface velocities in the central plateau are not significantly affected by the presence of an obstruction in this location. The pattern of rotation in the southeastern plateau is also only slightly affected by the strong crustal block.

4.2.2 Weak foreland regions

In the context of our model, there are several different methods of specifying how zones of weak continental crust may be embedded into a foreland region. For example, the crust could begin with lower viscosity in both the upper and lower crust; the upper crust could have "normal" viscosity while the lower crust begins with lower viscosity; the lower crust could weaken more rapidly once h_{crit+} is reached; or the upper crustal thickness and the critical thickness for weakening the lower crust could be lower, allowing a weak lower layer to develop in thinner crust. Here we use a combination of these criteria, and define a "weak" area as one in which the lower crust begins with slightly lower viscosity, the upper crust is thinner, the h_{crit+} is smaller than in the rest of the crust, and the timescale for weakening is shorter (see table 1). Thus, our definition of

a "weak" region is crust that is initially slightly weaker, and in which the development of a weak lower crust is accelerated.

The presence of a weak crustal zone located to the north of the convergent zone has a profound effect on the morphology and crustal velocities of the developing orogen. Because crust is assumed to be attached to a strong mantle lithosphere, deformation cannot move into the weak region until the topographic front reaches it. At this point, as the plateau margin grows northward to encompass the zone of weakness, a broad, gently sloping margin is rapidly developed across the weaker area (Fig 6a,b). Despite the gentle topographic slope that that is developed above the weak crustal zone, the margin does not develop by synchronous tilting of the entire margin in a ramp-like geometry. Instead, crust in areas closer to the central plateau begins to thicken first, and surface uplift propagates northward (Fig 7). Once the plateau margin reaches the far side of the weak zone, northward propagation slows (Fig 6c). The weaker region then begins to slowly inflate as lower crustal material continues to flow in from the central plateau. The increased flow of crust to the north results in a plateau that is lower in elevation, slightly narrower from east to west, and that does not propagate as far to the south as in the homogenous case.

Crustal velocities exhibit a dramatic response to the presence of the weak zone; a weak region results in crust being diverted towards the heterogeneity and rapid flow towards and across the developing margin (Fig 6, Fig 9). The effect of a weaker region is most remarkable in the velocities in the lower crust (Fig 6d, Fig 9). Even a relatively narrow weak region will draw in lower crust from a significant portion of the plateau. Almost all of the lower crust in the central plateau flows towards the weak zone, flow

towards the southern margin is greatly reduced, and flow towards the eastern and western margins is only seen relatively close to these margins. The E-W component of velocity in the central and northern plateau is directed inward due to the diversion of the lower crust towards the weak zone (Fig 6d, Fig 9). Deformation in the upper crust is less sensitive to the presence of the weak zone; although there is a greater component of northward velocity, the upper crust is not diverted into the weak zone from the east and west.

The rapid flow of material into the weak region results in a large amount of north-south surface extension in the central plateau. Although the southern margin does accommodate ~60% of the mantle convergence velocity, surface velocities on the plateau exceed convergence velocities near the transition into the weak zone. Extension in the central plateau is balanced by a commensurate amount of shortening distributed across the weak margin, as the topographic gradient across the margin results in a large gravity-driven flux of material into the weak zone.

The presence of a weak crustal zone located in a region to the east of the convergent zone has a similar effect on the morphology and crustal velocities of the plateau margin (Fig 8). A broad, gently sloping margin is rapidly developed across the weaker area. Surface velocities are affected into the central part of the plateau, so that the divide between eastward- and westward-flowing upper crust is located in the western part of the plateau. Thus more crust flows eastward than westward and the elevation of the plateau is lower than in the homogeneous case.

4.3 Application to Tibet

We have evaluated the effects of several different types of crustal heterogeneities on the development of an orogenic plateau and have shown that variations in crustal strength may have significant effects on the morphology and dynamics of a plateau. In order to investigate the combined effect of such heterogeneities in the context of the Tibetan Plateau, we set up a model that incorporates high-viscosity heterogeneities approximating the Sichuan and Tarim crustal blocks and a weak region east and south of the convergence zone (Fig 10), as suggested by the plateau topography and the model results shown above. In addition, because Indian crust is thought to be relatively rigid, we assign a slightly higher viscosity to the upper crust of the indenting block, resulting in a slightly slower southward propagation of the plateau.

This model, after 40 m.y. of evolution, produces a plateau that is similar to the Tibetan Plateau in a number of ways, particularly near the eastern and northern margins. The combination of a strong Sichuan Basin and a weak southeastern region result in a modeled eastern margin that matches the morphology of Eastern Tibet quite well. The slope and wavelength of the southeastern margin are reproduced (Fig 10), as are the steep margin adjacent to the Sichuan Basin, the intermediate slope northeastern margin, and the concave shape of the margin around the Sichuan Basin. The model also predicts the east-west asymmetry of the plateau, as the plateau's width increases and elevation decreases from west to east, despite a uniform convergence velocity.

Modeled surface velocities are comparable to surface velocities obtained with geodetic studies of Tibet [*Chen et al.*, 2000; *Zhang et al.*, 2004], as well as to crustal motions inferred from geologic mapping in eastern Tibet (Fig 11) [*Wang et al.*, 1998]. In

particular, the model predicts significant amounts of shortening across the southern margin/Himalayan front, a lack of shortening between the northern plateau and the Tarim Basin, and east-west extension in the central plateau. In eastern Tibet, the model also predicts the rotation of material around the eastern Himalayan syntaxis, a zone of left lateral shear approximately corresponding to the location of the Xianshuihe fault, a lack of convergence in the Longmen Shan, distributed right-lateral shear northwest of the Sichuan Basin, margin-parallel motion north of the Sichuan Basin, and shortening across the northeastern margin in the Qilian Shan (Fig. 11).

5. Discussion

The results in this paper suggest that crustal heterogeneities have profoundly influenced the development of the Tibetan Plateau, and that many of the distinctive features of the plateau may be related to the distribution of these strength heterogeneities. In particular, the overall shape and asymmetry of the plateau can be largely explained by preexisting variations in crustal rheology and temperature (with the possible exception of southeastern Tibet, which may have resulted from a young thermal anomaly of unknown origin – see below). The plateau morphology is consistent with anomalously strong crust beneath the Tarim Basin, which appears to have acted as an obstruction to the northward growth of the plateau. This has limited the north-south extent of the western plateau, resulting in a plateau that is narrower in the west than in the east. The eastern extent of the plateau may also have been affected by the presence of weaker crust on the southeastern margin. Our results suggest that transfer of crustal material from the western plateau to the volumetrically greater eastern plateau is the result of diversion of crust

around the strong Tarim block and the rapid influx of crustal material toward a region of weak crust along the southeastern margin. Thus, the asymmetry of the plateau may be largely attributed to the position of the Tarim Basin relative to the convergence zone, although the latitudinal variation in convergence velocity [i.e., *Soofi and King*, 2002], and the possible influence of a stress-free eastern boundary condition [i.e., *Tapponnier et al.*, 1982] may also play a role.

The strong (and recognizable) effects of crustal strength heterogeneities on the development of orogenic plateaus highlights the need to understand the origin and nature of such heterogeneities. Continental lithosphere is typically an amalgamation of crustal domains with different ages, composition, and geologic and thermal history; thus spatial variations in crustal properties should be expected. However, the juxtaposition of crustal units does not always produce the large effects seen in eastern and northern Tibet. For example, in the central Tibetan Plateau, the Bangong-Nujiang and Jinsha sutures, boundaries between different crustal blocks, are not reflected in the morphology of the current plateau.

5.1 Strong regions

The apparently anomalous strength of the crust and lithosphere beneath the Sichuan and Tarim Basins is consistent with the current thermal state and the deformation history of these regions. Both regions lack previous episodes of penetrative deformation that affected and may have further weakened other regions of Tibetan crust, and both basins have formed in old cratonic lithosphere. Although our model focuses on the influence of heterogeneities in the crust, such strength variations are not necessarily confined to the

crust, and may involve the mantle lithosphere as well. The Sichuan Basin, in particular, appears as a distinctive fast anomaly in P-wave velocity models at lithospheric depths [*Li et al.*, 2006], suggesting that the lithosphere is colder than the surrounding regions.

5.2 Uplift of the southeastern margin

Anomalously slow seismic velocities in the region of apparently weak crust in the southeastern plateau strongly suggest elevated temperatures in the lithosphere as compared to surrounding regions. The origin of such a thermal anomaly is not known; it may be related to mantle processes active above the slab in the Indo-Burman subduction zone to the west. However, much of southern China, including regions offshore, appears to show anomalously slow in P-wave velocities at shallow mantle (lithospheric) depths, suggesting a possible, regional-scale anomaly related to as yet unknown processes [*Li et al.*, 2006]. Potentially, the time at which the crust in this region became weak may shed light on the process by which this occurred. There are two end-member possibilities: first that the crust of the southeastern margin was weakened prior to plateau development, but that initiation of crustal thickening and lower crustal flow in this region occurred only after the southeastward edge of the plateau encountered the already-weakened crust. The second possibility is that the uplift and development of the southeastern plateau occurred at the same time as, and was initiated by, the weakening of the crust in this region. In the first scenario, the weakening is potentially unrelated to the growth of the plateau, while the second scenario is more suggestive of a link between crustal weakening and plateau propagation. In either case, crustal weakening cannot be simply related to crustal thickening and increased radiogenic heating because the region of weak lower crust

appears to extend across the entire southeastern margin to regions of normal thickness crust in southern Yunnan [*Xu et al.*, 2007; *Clark and Royden,* 2000]. Hence even areas of normal crustal thickness appear to have a weak layer in the lower/middle crust. Medvedev and Beaumont [2006] also conclude, based on modeling of channel injection, that the crust of the southeastern margin was likely initially weak.

The deformation history of the southeastern margin can provide some constraints on the timing of weakening. The crust of the southeastern margin contains large lithosphere-scale strike slip shear zones such as the Ailao Shan, which accommodated large lateral motions between ~34 and ~17 Ma [*Leloup et al.*, 2001]. Gneisses currently exposed in the Ailao Shan shear zone were metamorphosed at depths up to ~18 km, indicating significant localized topography, erosion and exhumation [*Schoenbohm et al.*, 2005]. This suggests that the crust in this region was sufficiently strong to support a narrow, localized mountain belt during this time period. Uplift of the southeastern margin without significant surface shortening appears to have been initiated around 8-12 Ma [*Clark et al., 2005b*, *Ouimet et al.,* 2005], suggesting that by this time the crust had become weak. Thus, the timing of weakening is approximately constrained to between ~20 and ~10 Ma. The current eastward-directed subduction regime in the Indo-Burman region and the opening of the Andaman Sea appear to have initiated around 13 Ma. The similarity in timing suggests that this change in boundary conditions may be related to the large-scale weakening of the lower crust in southeastern Tibet.

5.3 Structures

The distribution and development of structural features on the Tibetan Plateau can be understood in light of this distribution of crustal strength heterogeneities. Our model treats the crust as a linear viscous material; therefore there is less strain partitioning in our results than would occur if we had incorporated a non-linear rheology or strain weakening along faults. Nevertheless, even this linear viscous rheology produces many features of plateau deformation, many of which can be related to the location, orientation, and timing of observed structural features, as described below.

5.3.1 East-west extension

Models that incorporate a weak crustal area east of the convergence zone produce westward flow of crust and a dramatic increase east-west extension across the central plateau. Significantly, this is the result of and occurs contemporaneously with uplift of the eastern plateau. The observations from the plateau show a similar pattern, with the onset of rapid uplift of the southeastern plateau (at ~10 Ma) being approximately the same age as the onset of east-west extension in the central plateau (~8 Ma). We propose that east-west extension within the central plateau is due largely to the rapid motion of crustal material eastward into the region of weak crust in the southeastern plateau. If our interpretation is correct, the onset of east-west extension should be associated with a small overall decrease in plateau elevation as material is evacuated from beneath the high plateau. This is in contrast to the hypothesis that extension results from a rapid increase in plateau elevation, perhaps due to convective removal of the lower lithosphere beneath Tibet. [i.e., *Molnar et al.*, 1993].

5.3.2 Strike-slip faults

Important strike-slip faults exist adjacent to both the Sichuan and Tarim basins and accommodate movement of crustal material parallel or oblique to the margin. The Altyn Tagh Fault, which occurs near the boundary between the plateau and the Tarim basin, appears to have had a long history with varying rates of motion. Its role in the development of the Tibetan Plateau, especially its early history, is the subject of much debate [i.e., Mériaux et al., 2004; Shen et al., 2001; Yue et al., 2001]. However, the location of the Altyn Tagh Fault and its role in accommodating eastward, margin parallel motion in the upper crust suggest that the strong Tarim block has played an important role in the localization of this fault along the plateau margin. Although the Altyn Tagh Fault may have accommodated large amounts of displacement prior to and in the early stages of the India-Asia collision, we propose that the primary role of the current fault is the diversion of the upper crust eastward past the Tarim Basin, with transfer of shortening in the upper crust to the eastern and western ends of the fault.

The Xianshuihe Fault is a younger feature that is generally thought to accommodate clockwise rotation of crustal material around the eastern Himalayan syntaxis. The timing of motion along the fault is not well constrained, but extrapolation of current rates indicates that the fault initiated at ~8-10 Ma [*Wang et al.*, 1998], making it approximately coeval with the initial uplift of the eastern plateau margin. Comparison with model results indicates that the Xianshuihe Fault accommodates a diversion of crustal material to the south around the strong crustal block of the Sichuan Basin. It also accommodates a rapid flow of crustal material into the weak crust region of southeastern Tibet. Our modeling suggests that the Xianshuihe Fault may have developed as the result of these two major strength heterogeneities. If so, then its development is causally linked

to rapid uplift of the eastern plateau and the onset of rapid southeastward flow in the lower crust, as both result from the interaction of the developing plateau with areas of anomalously strong or weak crust.

6. General Conclusions

As regions of anomalously strong or weak crust are incorporated into an actively developing plateau system, they cause systematic and recognizable effects on plateau shape, plateau margin steepness, and crustal velocity. The contrasting styles of deformation and morphology accompanying these lateral strength variations enable us to recognize crustal strength variations in actual orogens. The morphology of the northern and eastern margins of Tibet is consistent with the presence of strong crust in the regions of the Sichuan and Tarim Basins and weak crust beneath the southeastern margin.

As a developing plateau encounters regions of strong crust, the adjacent plateau margin becomes steep, and is localized along the boundaries of the strong crustal block, and is commonly concave in map view. Despite the steepness of these margins, they do not accommodate significant shortening strain, and crustal material within the plateau does not generally move towards this plateau edge. Instead, velocities in both the upper and lower crust are directed subparallel to the plateau margin (Fig 4, Fig 9).

As regions of weak crust become incorporated into a developing plateau, the plateau margin acquires characteristics that are nearly opposite to those of a strong region. The weak crustal region develops a gently sloping margin that propagates rapidly across the weak zone and accommodates large amounts of shortening. Crustal material

within the plateau moves towards the low-strength region, with rapid flow towards and across the low-gradient plateau margin (Fig 6, Fig 9).

We emphasize that the models presented here treat the entire crust as a continuously deforming material. In a real system, the dynamics of the upper crust will be complicated by strain partitioning along discrete structures and by the possibility of more block-like motion or the development of brittle fold and thrust belts. We emphasize that the goal of this study is to explore some of the large-scale dynamics that result from the presence of crustal strength heterogeneities, and not to reproduce a detailed deformation history of plateau deformation. However, despite the simple rheology used in this model, a model set up with the appropriate geometry creates a plateau that matches a number of key features of the Tibetan Plateau. The similarities between the surface deformation predicted by the model and the GPS velocities in eastern Tibet suggest that the model is accurately capturing some of the fundamental controls of the dynamics of the plateau and can therefore be used with some confidence to more closely investigate the role of crustal heterogeneities in shaping the Tibetan Plateau.

Acknowledgements

This work was supported by the National Science Foundation (NSF) Continental Dynamics Program (grant EAR-0003571) and an NSF graduate student fellowship (to K.L. Cook). We also thank Chris Beaumont and Olivier Vanderhaeghe for extremely helpful and constructive reviews.

Table 1

	Maximum thickness of upper crust, h_1	Critical thickness for viscosity transition, h_{crit+}	Viscosity of upper crust, μ_1	Minimum viscosity of lower crust, μ_2	Timescale of viscosity transition in lower crust, t_{change}
normal crust	50 km	60 km	10^{21} Pa s	10^{17} Pa s	4 My
weak crust	36 - 50 km	36 - 60 km	10^{21} Pa s	$5 * 10^{17}$ Pa s	2 My
strong crust	50 km	60 km	10^{23} Pa s	$7.5 * 10^{22}$ Pa s	4 My
Parameters for Tibet set-up					
weak crust	36 - 50 km	36 - 60 km	10^{21} Pa s	10^{19} Pa s	2 My
strong crust	50 km	60 km	10^{23} Pa s	$7.5 * 10^{22}$ Pa s	4 My
Indian crust	50 km	60 km	$1.25 * 10^{21}$ Pa s	10^{17} Pa s	4 My

Appendix A

Derivation of the analytical solution

The crustal flow model developed here treats the crust as a Newtonian viscous fluid composed of two layers. The upper layer has viscosity μ_1 and thickness h_1, while the lower layer has viscosity μ_2 and thickness $(h - h_1)$, where h is the total thickness of the crust. Both layers have the same density ρ_c, and μ_1 is always greater than or equal to μ_2. Viscosity is dependent only on depth, total crustal thickness, and the initial viscosity distribution imposed. Deformation is described by the Stokes and continuity equations. For a fluid with variable viscosity the balance of forces in the x-direction can be expressed as

$$\partial_x P = 2\partial_x(\mu\partial_x u) + \partial_z(\mu\partial_z u + \mu\partial_x w) + \partial_x(\mu\partial_y u + \mu\partial_x v) \qquad \text{(eq. 1)}$$

with similar formulations for y and z-directions. Flow is driven by pressure gradients caused by variations in the vertical compressive stress resulting from gradients in the surface topography. Pressure and viscous stress contribute to the total normal stress in the fluid. Thus, the vertical compressive stress is given by (Turcotte and Schubert p. 236)

$$\sigma_{zz} = P - \tau_{zz} = P - 2\mu\partial_z w \qquad \text{(eq. 2)}$$

In order to solve to solve the Stokes equations explicitly for velocity in the x and y directions, we define a stream function Ψ such that

$$\nabla \times (-\Psi_1, \Psi_2, 0) = (u, v, w),\ u = \frac{-\partial\Psi_2}{\partial z},\ v = \frac{-\partial\Psi_1}{\partial z},\ w = \frac{\partial\Psi_2}{\partial x} + \frac{\partial\Psi_1}{\partial y} \qquad \text{(eq. 3)}$$

Differentiating eq. 2 and combining with eq. 3 yields

$$\partial^2_{xz} P = \partial^2_{xz}(\sigma_{zz}) + 2\partial^2_{xz}(\mu\partial_z w) = \partial^2_{xz}(\sigma_{zz}) + 2\partial_{xz}(\mu\partial^2_{zx}\Psi_2 + \mu\partial^2_{zy}\Psi_1) \qquad \text{(eq. 4)}$$

Eq. 4 can be combined with eq 1 to yield eq. 5:

$$\partial^2_{xz}(\sigma_{zz}) = -4\partial^2_{xz}(\mu\partial^2_{xz}\Psi_2) + \partial^2_{zz}(\mu\partial^2_{xx}\Psi_2 + \mu\partial^2_{xy}\Psi_1 - \mu\partial^2_{zz}\Psi_2) - 2\partial^2_{xz}(\mu\partial^2_{yz}\Psi_1) - \partial^2_{yz}(\mu\partial^2_{zy}\Psi_2 + \mu\partial^2_{xz}\Psi_1)$$

We make the approximation that higher order lateral derivatives of Ψ are small compared to vertical derivatives, so the terms $\partial_{xx}\Psi$, $\partial_{xy}\Psi$, and $\partial_{yy}\Psi$ can be neglected. Eq. 4 can then be

restated in terms of u and v, and integrated over the crustal thickness. After applying the surface boundary conditions: $\partial_x(\sigma_{zz})|_{z=0} = \partial_x T\rho_c g$, where T is the elevation of the surface above sea level, and the surface velocity $u_s = u(0)$, this yields:

$$\partial_x T\rho_c g = 4\partial_x(\mu\partial_x u_s) + \partial_z(\mu\partial_z u) + 2\partial_x(\mu\partial_y v_s) + \partial_y(\mu\partial_y u_s + \mu\partial_x v_s) \qquad \text{(eq. 6)}$$

Eq. 6 can then be solved explicitly for *u(z)*, the *x*-component of velocity, by repeated integration of $\partial_z(\mu\partial_z u)$ over the thickness of the crust.

$$u(z) = u_s - \int_0^z \frac{1}{\mu}\int_0^z [4\partial_x(\mu\partial_x u_s) + 2\partial_x(\mu\partial_y v_s) + \partial_y(\mu\partial_y u_s) + \partial_y(\mu\partial_x v_s)]dzdz + \int_0^z \frac{1}{\mu}\int_0^z \partial_x T\rho_c g\, dzdz$$

(eq. 7)

Evaluating eq. 6 for basal velocity $u_b = u(h)$ gives an explicit expression for velocity at the surface:

$$u_s = u_b - \frac{\partial_x T\rho_c g}{2}\left(\frac{h_1^2}{\mu_1} + \frac{h^2 - h_1^2}{\mu_2}\right) + \frac{h - h_1}{\mu_2}\left[uds_{h_1\Delta\mu}\right] + \frac{h_1^2}{2\mu_1}\left[uds_{\mu_1}\right] + \frac{h^2 - h_1^2}{2\mu_2}\left[uds_{\mu_2}\right] \qquad \text{(eq. 8)}$$

Performing the analogous derivation for the y-direction gives

$$v_s = v_b - \frac{\partial_y T\rho_c g}{2}\left(\frac{h_1^2}{\mu_1} + \frac{h^2 - h_1^2}{\mu_2}\right) + \frac{h - h_1}{\mu_2}\left[vds_{h_1\Delta\mu}\right] + \frac{h_1^2}{2\mu_1}\left[vds_{\mu_1}\right] + \frac{h^2 - h_1^2}{2\mu_2}\left[vds_{\mu_2}\right] \qquad \text{(eq. 9)}$$

where

$uds_{\mu_1} = 4\partial_x(\mu_1\partial_x u_s) + 2\partial_x(\mu_1\partial_y v_s) + \partial_y(\mu_1\partial_y u_s) + \partial_y(\mu_1\partial_x v_s)$, and

$vds_{\mu_1} = 4\partial_y(\mu_1\partial_y v_s) + 2\partial_y(\mu_1\partial_x u_s) + \partial_x(\mu_1\partial_x v_s) + \partial_x(\mu_1\partial_y u_s)$,

with analogous expressions for $uds_{\mu 2}$, $vds_{\mu 2}$, $uds_{\mu 2}$, $uds_{h1\Delta\mu}$, and $vds_{h1\Delta\mu}$. We use eqs. 7 and 8, and the equivalent equations for *v(z)* and v_s to obtain the flux through a column of crust in the *x* and *y* directions. The difference in flux across the column gives the amount of material added to or removed from the column and therefore the rate of change in crustal thickness:

$$\frac{\partial h}{\partial t} = -\left(\frac{\partial}{\partial x}U + \frac{\partial}{\partial y}V\right)$$

$$= -\frac{\partial}{\partial x}\left[u_b h + \frac{\partial_x T\rho_c g}{3\mu_2}\left(-h^3 + \frac{h_1^3\Delta\mu}{\mu_1}\right) + \frac{h^2 - h_1^2}{2\mu_2}\left[uds_{h_1\Delta\mu}\right] + \frac{h_1^3}{3\mu_1}\left[uds_{\mu_1}\right] + \frac{h^3 - h_1^3}{3\mu_2}\left[uds_{\mu_2}\right]\right] +$$

$$-\frac{\partial}{\partial y}\left[u_b h + \frac{\partial_y T\rho_c g}{3\mu_2}\left(-h^3 + \frac{h_1^3\Delta\mu}{\mu_1}\right) + \frac{h^2 - h_1^2}{2\mu_2}\left[vds_{h_1\Delta\mu}\right] + \frac{h_1^3}{3\mu_1}\left[vds_{\mu_1}\right] + \frac{h^3 - h_1^3}{3\mu_2}\left[vds_{\mu_2}\right]\right] \quad \text{(eq. 10)}$$

Equations 8, 9, and 10 are non-dimensionalized and solved simultaneously on a two-dimensional grid to obtain the surface velocities and crustal thickness at each timestep.

References

Abdrakhmatov, K. Y., S. A. Aldazhanov, B. H. Hager, M. W. Hamburger, T. A. Herring, K. B. Kalabaev, V. I. Makarov, P. Molnar, S. V. Panasyuk, and M. T. Prilepin (1996), Relatively recent construction of the Tien Shan inferred from GPS measurements of present-day crustal deformation rates, *Nature, 384*, 450-453.

Beaumont, C., R. A. Jamieson, M. H. Nguyen, and B. Lee (2001), Himalayan tectonics explained by extrusion of a low-viscosity crustal channel coupled to focused surface denudation, *Nature, 414*, 738–742.

Beaumont, C., Nguyen, M., Jamieson, R.A., and S. Ellis (2006), Crustal flow modes in large hot orogens, in *Channel Flow, Ductile Extrusion and Exhumation of Lower-mid Crust in Continental Collision Zones,* edited by R. D. Law, M. Searle, and L. Godin, *Geological Soc. London Spec. Publ., 268,* pp. 91-145.

Bird, P. (1991), Lateral extrusion of lower crust from under high topography, in the isostatic limit, *J. of Geophys. Res., 96*, 10,275-10,286.

Bouhallier, H., Chardon, D., and P. Choukroune (1995), Strain patterns in Archaic dome-and basin structures: the Dharwar craton (Karnataka, south India). *Earth and Planetary Science Letters*, 135, p. 57-75.

Brown, L. D., W. Zhao, K. D. Nelson, M. Hauck, D. Alsdorf, A. Ross, M. Cogan, M. Clark, X. Liu, and J. Che (1996), Bright Spots, Structure, and Magmatism in Southern Tibet from INDEPTH Seismic Reflection Profiling, *Science, 274*, 1688-1690.

Bullen, M. E., D. W. Burbank, J. I. Garver, and K. Y. Abdrakhmatov (2001), Late Cenozoic tectonic evolution of the northwestern Tien Shan: New age estimates for the initiation of mountain building, *Geol. Soc. Am. Bull., 113(12),* 1544-1559.

Bullen, M. E., D. W. Burbank, and J. I. Garver (2003), Building the Northern Tien Shan: Integrated Thermal, Structural, and Topographic Constraints, *J. of Geology, 111(2),* 149-165.

Burchfiel, B.C., Z. Chen, Y. Liu, and L. H. Royden (1995), Tectonics of the Longmen Shan and adjacent regions, *Int. Geological Rev., 37(8),* 661–736.

Chen W.-P., C.-Y. Chen, J. L. Nabelek (1999), Present-day deformation of the Qaidam basin with implications for intra-continental tectonics, *Tectonophysics, 305(1),* 165-181.

Chen, Z., B. C. Burchfiel, Y. Liu, R. W. King, L. H. Royden, W. Tang, E. Wang, J. Zhao, and X. Zhang (2000), Global Positioning System measurements from eastern Tibet and their implications for India/Eurasia intercontinental deformation, *J. Geophys. Res., 105*, 16,215–16,227.

Clark, M. K., and L. H. Royden (2000), Topographic ooze: building the eastern margin of Tibet by lower crustal flow. *Geology 28*, 703–706.

Clark M. K., J. W. M. Bush, and L. H. Royden, 2005a, Dynamic topography produced by lower crustal flow against rheological strength heterogeneities bordering the Tibetan Plateau, *Geophys. J. Int., 162*, 575–590.

Clark, M. K., M. A. House, L. H. Royden, B. C. Burchfiel, K. X. Whipple, X. Zhang, and W. Tang, 2005b, Late Cenozoic uplift of southeastern Tibet, *Geology, 33*, 525-528.

Cowgill, E., A. Yin, T. M. Harrison, and X. F. Wang (2003), Reconstruction of the Altyn Tagh fault based on U-Pb geochronology: Role of back thrusts, mantle sutures, and heterogeneous crustal strength in forming the Tibetan Plateau, *J. Geophys. Res., 108(B7),* 2346.

DeMets, C., R. G. Gordon, D. F. Argus, and S. Stein (1994), Effect of recent revisions to the geomagnetic reversal time scale on estimates of current plate motions, *Geophys. Res. Letters*, 21, 2191-2194.

Dewey, J. F., R. M. Shackleton, C. Chengfa, and S. Yiyin (1988), The Tectonic Evolution of the Tibetan Plateau, *Phil. Trans. R. Soc. London, 327*, 379-413.

England, P., and G. Houseman (1986), Finite strain calculations of continental deformation 2. Comparison with the India – Asia collision zone, *J. Geophys. Res., 91(3),* 3664-3676.

England, P., and G. Houseman (1985), The influence of lithospheric strength heterogeneities on the tectonics of Tibet and surrounding regions, *Nature, 315*, 297-301.

Fielding , E., Isacks, B., Barazangi, M., and C. Duncan (1994), How Flat is Tibet?, *Geology, 22*, 163-167.

Flesch, L., A. Haines, and W. Holt (2001), Dynamics of the India-Eurasia collision zone, *J. Geophys. Res., 106(B8)*, 16,435–16,460.

Guillot, S., Garzanti, E., Baratoux, D., Marquer, D., Mahéo, G. and J. de Sigoyer (2003), Reconstructing the total shortening history of the NW Himalaya, *Geochem. Geophys. Geosystems,* 4, 1064, doi:10.1029/2002GC000484

Haines, S. S., S. L. Klemperer, L. Brown, J. Guo, J. Mechie, R. Meissner, A. Ross, and W. Zhao (2003), INDEPTH III seismic data: From surface observations to deep crustal processes in Tibet, *Tectonics, 22(1),* 1001.

Hodges, K. V. (2000), Tectonics of the Himalaya and southern Tibet from two perspectives, *Bull. Geological Soc. America, 112(3),* 324-350.

Jamieson, R. A., Beaumont, C., Nguyen, M. H. and B. Lee (2002), Interaction of metamorphism, deformation and exhumation in large convergent orogens, *J. metamorph. Geol.,* 20, 9–24.

Jamieson, R. A., Beaumont, C., Nguyen, M.H., and N. G. Culshaw (2007), Synconvergent ductile flow in variable-strength continental crust: Numerical models with application to the western Grenville orogen, *Tectonics, 26*, TC5005, doi:10.1029/2006TC002036.

Kaufman, P. S., and L. H. Royden (1994), Lower crustal flow in an extensional setting: Constaints from Halloran Hills region, eastern Mojave Desert, California, *J. Geophys. Res., 99(B8),* 15,723-15,739.

Kirby, E., P. W. Reiners, M. A. Krol, K. X. Whipple, K. V. Hodges, K. A. Farley, W. Tang, and Z. Chen (2002), Late Cenozoic evolution of the eastern margin of the Tibetan Plateau: Inferences from 40Ar/39Ar and (U-Th)/He thermochronology: *Tectonics, 21*, 1001.

Klein, A., W. Jacoby, and P. Smilde (1997), Mining-induced crustal deformation in northwest Germany: modelling the rheological structure of the lithosphere, *Earth Planet. Sci. Lett., 147,* 107-123.

Leloup, P. H., N. Arnaud, R. Lacassin, J. R. Kienast, T. M. Harrison, T. T. Trong, A. Replumaz, and P. Tapponnier (2001), New constraints on the structure,

thermochronology, and timing of the Ailao Shan-Red River shear zone, SE Asia, *J. Geophys. Res., 106(B4),* 6683-6732.

Li, C., R. D. van der Hilst, and M. N. Toksoz (2006), Constraining P-wave velocity variations in the upper mantle beneath Southeast Asia, *Phys. Earth Planet. Inter, 154*, 180–195.

Medvedev, S., and Beaumont, C. (2006), Growth of continental plateaus by channel injection: constraints and thermo-mechanical consistency, in *Channel Flow, Ductile Extrusion and Exhumation of Lower-mid Crust in Continental Collision Zones,* edited by R. D. Law, M. Searle, and L. Godin, *Geological Soc. London Spec. Publ., 268*, pp. 147-164.

Medvedev, S. (2002), Mechanics of viscous wedges: modelling by analytical and numerical approaches, *J.. Geophysical Res.*, 107 (B6), 1-15.

Mériaux, A. S., F. J. Ryerson, P. Tapponnier, J. Van der Woerd, R. C. Finkel, X. Xu, Z. Xu, and M. W. Caffee (2004), Rapid slip along the central Altyn Tagh Fault: Morphochronologic evidence from Cherchen He and Sulamu Tagh, *J. Geophys. Res, 109.*

Michel, G. W., M. Becker, D. Angermann, C. Reigber, and E. Reinhart (2000), Crustal motion in E- and SE-Asia from GPS measurements, *Earth Planets Space, 52*, 713-720.

Molnar, P (1988), A Review of Geophysical Constraints on the Deep Structure of the Tibetan Plateau, the Himalaya and the Karakoram, and their Tectonic Implications, *J Phil. Trans. Royal Soc. London. Series A*, 326(1589), 33-88.

Molnar, P., P. England, and J. Martinod (1993), Mantle dynamics, uplift of the Tibetan Plateau, and the Indian monsoon, *Rev. of Geophysics, 31(4),* 357-396.

Molnar, P., and P. Tapponnier (1975), Cenozoic tectonics of Asia: effects of a continental collision, *Science, 189*, 419–426.

Murphy, M. A., A. Yin, T. M. Harrison, S. B. Duerr, Z. Chen, F. J. Ryerson, W. S. F. Kidd, X. Wang, and X. Zhou (1997), Did the Indo-Asian collision alone create the Tibetan Plateau?, *Geology, 25(8),* 719-722.

Nelson, K. D., W. Zhao, L. D. Brown, J. Kuo, J. Che, X. Liu, S. L. Klemperer, Y. Makovsky, R. Meissner, J. Mechie, R. Kind, F. Wenzel, J. Ni, J. Nabelek, C.

Leshou, H. Tan, W. Wei, A. G. Jones, J. Booker, M. Unsworth, W. S. F. Kidd, M. Hauck, D. Alsdorf, A. Ross, M. Cogan, C. Wu, E. Sandvol, and M. Edwards (1996), Partially molten middle crust beneath southern Tibet: synthesis of project INDEPTH results, *Science, 274*, 1684-1688.

Ouimet, W. B., K. X. Whipple, and L. H. Royden (2005), Long and short-term erosion and river incision on the eastern margin of the Tibetan plateau, a transient landscape, *Eos Trans. AGU, 86*(52), Fall Meet. Suppl., Abstract H31A-1279.

Ozacar, A. A., and G. Zandt (2004), Crustal seismic anisotropy in central Tibet: Implications for deformational style and flow in the crust, *Geophys. Res. Lett, 31*, L23601.

Powell, C. M. (1986), Continental underplating model for the rise of the Tibetan plateau, *Earth planet. Sci. Lett., 81(1)*, 13579–94.

Reigber, Ch., Michel, G. W., Galas, R., Angermann, D., Klotz, J., Chen, J. Y., Papschev, A., Arslanov, R., Tzurkov, V. E., and M. C. Ishanov (2001), New space geodetic constraints on the distribution of deformation in Central Asia, *Earth and Planetary Science Letters*, 191, 157–165

Rosenberg, C., and M. Handy (2005), Experimental deformation of partially melted granite revisited: implications for the continental crust, *J. Metam. Geol.*, 23, 19-28.

Ross, A.R., L. D. Brown, P. Pananont, K. D. Nelson, S. Klemperer, S. Haines, Z. Wenjin, and G. Jingru (2004), Deep reflection surveying in central Tibet: lower-crustal layering and crustal flow, *Geophys. J. Int., 156(1),* 115.

Rowley, D. B. (1996), Age of initiation of collision between India and Asia: A review of stratigraphic data, *Earth and Planetary Science Letters*, 145, 1–13.

Rowley, D. B., and B. S. Currie (2006), Palaeo-altimetry of the late Eocene to Miocene Lunpola basin, central Tibet, Nature, 439, 677-681.

Royden, L. H. (1996), Coupling and decoupling of crust and mantle in convergent orogens: Implications for strain partitioning in the crust, *J. Geophys. Res., 101(B8)*, 17,679-17,705.

Royden L.H., B.C. Burchfiel, W. King, E. Wang, Z. Chen, F. Shen and Y. Liu (1997), Surface Deformation and Lower Crustal Flow in Eastern Tibet, *Science, 276*, 788–790.

Schoenbohm, L. M., B. C. Burchfiel, C. Liangzhong, and Y. Jiyun (2005), Exhumation of the Ailao Shan shear zone recorded by Cenozoic sedimentary rocks, Yunnan Province, China, *Tectonics, 24(6),* TC6015, doi:10.1029/2005TC001803.

Shapiro, N. M., M. H. Ritzwoller, P. Molnar, and V. Levin (2004), Thinning and Flow of Tibetan Crust Constrained by Seismic Anisotropy, *Science, 305*, 233-236.

Shen, F., L. H. Royden, and B. C. Burchfiel (2001), Large-scale crustal deformation of the Tibetan Plateau, *J. Geophys. Res., 106*, 6793– 6816.

Soofi, M. A., and S. D. King (2002), Oblique convergence between India and Eurasia, *J. Geophys. Res, 107,* 2101.

Tapponnier, P., G. Peltzer, A. Y. Le Dain, R. Armijo, and P. Cobbold (1982), Propagating extrusion tectonics in Asia; new insights from simple experiments with plasticine, *Geology, 10(12)*, 611-616.

Tapponnier, P., Z. Xu, F. Roger, B. Meyer, N. Arnaud, G. Wittlinger, and J. Yang (2001), Oblique stepwise rise and growth of the Tibet Plateau, *Science, 294*, 1671–1677.

Vanderhaeghe, O., Burg, J.-P., and C. Teyssier (1999a), Exhumation of migmatites in two collapsed orogens: Canadian Cordillera and French Variscides, *Geological Society London Special Publications*, 154, 181-204.

Vanderhaeghe, O., Teyssier, C., and R. Wysoczanski (1999b), Structural and geochronologic constraints on the role of partial melting during the formation of the Shuswap metamorphic core complex at the latitude of the Thor-Odin dome, *British Columbia:Canadian Journal of Earth Sciences*, 36, 917-943.

Vanderhaeghe, O., and Teyssier, C. (2001), Partial melting and flow of orogens, *Tectonophysics*, 342, 451-472.

Vanderhaeghe, O., S. Medvedev, P. Fullsack, C. Beaumont, and R. A. Jamieson (2003), Evolution of orogenic wedges and continental plateaux: insights from crustal thermal-mechanical models overlying subducting mantle lithosphere, *Geophys. J. Int., 153*, 27-51.

Vergnolle, M., F. Pollitz, and E. Calais (2003), Constraints on the viscosity of the continental crust and mantle from GPS measurements and postseismic deformation models in western Mongolia, *J. Geophys. Res, 108*, 15-1.

Vilotte, J. P., M. Daignieres, R. Madariaga, and O. C. Zienkiewicz (1984), The role of a heterogenous inclusion during continental collision, *Phys. Earth Planet. Inter., 36*, 236-259.

Wang, E., B. C. Burchfiel, L. H. Royden, L. Chen, J. Chen, and W. Li (1998), *Late Cenozoic Xianshuihe-Xiaojiang and Red River fault systems of southwestern Sichuan and central Yunnan, China*, Geological Society of America Special Paper, 327, 108 p.

Wang, Y. (2001), Heat flow pattern and lateral variation of lithosphere strength in China mainland: constraints on active deformation, *Phys. Earth Planet. Inter., 126*, 121–146.

Windley, B. F., M. B. Allen, C. Zhang, Z. Y. Zhao, and G. R. Wang (1990), Paleozoic accretion and Cenozoic redeformation of the Chinese Tien Shan Range, Central Asia, *Geology, 18(2),* 128-131.

Wei, W., M. Unsworth, A. Jones, J. Booker, H. Tan, D. Nelson, L. Chen, S. Li, K. Solon, and P. Bedrosian (2001), Detection of widespread fluids in the Tibetan crust by magnetotelluric studies, *Science, 292*, 716–718.

Westaway, R. (2001), Flow in the lower continental crust as a mechanism for the Quaternary uplift of the Rhenish Massif, north-west Europe, in *River Basin Sediment Systems: Archives of Environmental Change*, edited by D. Maddy, M.G. Macklin and J.C. Woodward, pp. 87–167. Balkema, Abingdon, UK

Xu, L., S. Rondenay, and R. D. van der Hilst (2007), Structure of the crust beneath the Southeastern Tibetan Plateau from teleseismic receiver functions, submitted to Phys. Earth Planet. Int.

Yue, Y., B. D. Ritts, and S. A. Graham (2001), Initiation and long-term slip history of the Altyn Tagh fault, *Int. Geology Rev., 43*, 1087-1093.

Zhang P., Z. Shen, M. Wang, W. Gan, R. Burgmann, P. Molnar, Q. Wang, Z. Niu, J. Sun, J. Wu, H. Sun, and X. You (2004), Continuous deformation of the Tibetan plateau from global positioning system data, *Geology, 32*, 809–812.

Zhao, W., and W. J. Morgan (1987), Injection of Indian crust into Tibetan lower crust: A two-dimensional finite element model study, *Tectonics, 6*, 489 – 504.

Zhao W., Mechie, J., Brown, L. D., Guo, J., Haines, S. Hearn, T., Klemperer, S. L., Ma, Y. S., Meissner, R., Nelson, K. D., Ni, J. F., Pananont, P., Rapine, R., Ross, A., and J. Saul (2001), Crustal structure of central Tibet as derived from project INDEPTH wide-angle seismic data, *Geophys. J. Int.*, 145, 486–498

Zhu, B., Kidd, W. S. F., Rowley, D. B., Currie, B. S., and N. Shafique (2005), Age of Initiation of the India-Asia Collision in the East-Central Himalaya, *J. of Geology*, 113, 265–285.

Figure Captions

Figure 1

Topography and major structures of the Tibetan Plateau and surrounding regions. Strike-slip faults are drawn in black, normal faults are dark blue, and thrust faults are red. Light blue lines are major rivers.

Figure 2

(a) Plan view of model setup for crust with a strong foreland region, illustrating imposed basal (mantle) velocity and crustal viscosity distribution. A region 2000 km wide is assigned a northward basal velocity of 5 cm/yr, basal velocity elsewhere is zero. The northern boundary of the indenting region remains fixed. This viscosity distribution corresponds to the model results discussed in section 4.2.1 and shown in figure 4.
(b) Schematic cross section of a model plateau resulting from the initial setup shown in panel (a) after 40 m.y. of evolution, illustrating both lateral and vertical variations in crustal viscosity. A low-viscosity lower crust has formed in regions of thick crust, except in the area designated as "strong crust". Note the vertical exaggeration.

Figure 3

Evolution of topography and surface velocities (arrows) of a plateau formed in laterally homogenous crust. (a) 4 m.y. after the initiation of convergence the crustal thickness has not yet reached the critical thickness parameter h_{crit+}, so the lower crust remains strong and a linear mountain range has formed. (b) By 16 m.y., the lower crust beneath the

center of the orogen has weakened, and the orogen has stopped growing taller and has transitioned into a plateau. (c) Between 16 and 40 m.y. the plateau continues to grow outwards in all directions. The The surface velocities at 40 m.y. indicate significant shortening across the southern margin, rotation around the syntaxes, and a component of east-west extension in the central plateau.

Figure 4

(a)-(c) Evolution of topography and surface velocities (arrows) of a plateau with a region of strong crust in the foreland (see figure 2). Contours are 500, 2000, 3500, and 5000 m elevation. (a) By 12 m.y. the northern flank of the growing plateau has reached the region of strong crust and a very steep margin has begun to develop. (b) Between 12 and 24 m.y. the plateau propagates to the east, west, and south, while the northern margin remains stationary. (c) By 40 m.y. the plateau has begin to wrap around the eastern and western boundaries of the strong region. (d) Topography and lower crustal velocities after 40 m.y. of evolution. Note the change in velocity scale. The slight asymmetry in the topography and velocities is due to staggering of the velocity and viscosity grids.

Figure 5

Topography and surface velocities (arrows) after 40 m.y. of evolution of a plateau with a region of strong crust east of the suture zone. Contours are 500, 2000, 3500, and 5000 m elevation.

Figure 6

(a)-(c) Evolution of topography and surface velocities (arrows) of a plateau with a region of weak crust in the foreland. Contours are 500, 2000, 3500, and 5000 m elevation. The blue box indicates the boundary of the weak zone. At 16 m.y. (a) the plateau margin has barely reached the weak zone, between 16 and 23 m.y. (b) the weak zone experiences rapid crustal thickening and northward propagation of the plateau. By 40 m.y. (c) the plateau margin has reached the northern end of the weak zone, rapid northward propagation has ceased, and a steeper northern margin has been reestablished.
(d) Topography and lower crustal velocities after 40 m.y. of evolution. The lower crust still flows rapidly into the weak zone causing the crust to continue thickening.

Figure 7

Plot of elevation vs. time for locations as shown. (a) Progression of uplift from south to north. Point b, located closest to the suture, experiences early, relatively rapid uplift, while points c, d, and e, located in the region of weak crust, experience rapid uplift that progresses from south to north. Rapid flow of crust into the weak region causes the decrease in elevation of points b and c in conjunction with the uplift of points farther north. (b) Rapid uplift of points b and c relative to slower uplift at points a and f , located to the south and west of the mantle suture. (c) Locations of points a through f.

Figure 8

Topography and surface velocities (arrows) after 40 m.y. of evolution of a plateau with a region of weak crust east of the suture zone. Contours are 500, 2000, 3500, and 5000 m elevation. The black box indicates the boundary of the weak zone.

Figure 9

(a) Magnitude and direction of the upper crustal velocity (white arrows) and the maximum lower crustal velocity (black arrows) for 40 m.y. plateaus shown in figures 3, 4, and 5. Letters indicate the locations of profiles in panels (b) and (c). (b) North-south velocity-depth profiles, with north positive. (c) East-west velocity-depth profiles, with east positive. Note the rapid northward flow of both upper and lower crust in the weak foreland model, and the margin parallel of both upper and lower crust flow in the strong foreland model.

Figure 10

Initial setup and evolution of a plateau with a Tibet-like distribution of strong and weak regions as indicated in top panel. Regions of strong crust are analogous to the Sichuan and Tarim Basins, and a region of weaker crust is placed to the east and south of the eastern indenter corner. Contours are 500, 2000, 3500, and 5000 m elevation. Arrows show surface velocity. See text for discussion.

Figure 11

Comparison of Tibet-like model to the topography, GPS velocities, and structures of the Tibetan Plateau. a) Topography, and selected major strike-slip and normal faults for Tibet. b) Elevation and surface velocities from the model presented in figure 8 after 40 m.y. of evolution. Thick black lines suggest possible correspondence with structures in Tibet. c) Contours of elevation and GPS velocities (after *Chen et al.*, 2000; *Zhang et al.*, 2004) for Tibet. Contours in all panels are 500, 2000, 3500, and 5000 m elevation. See text for discussion.

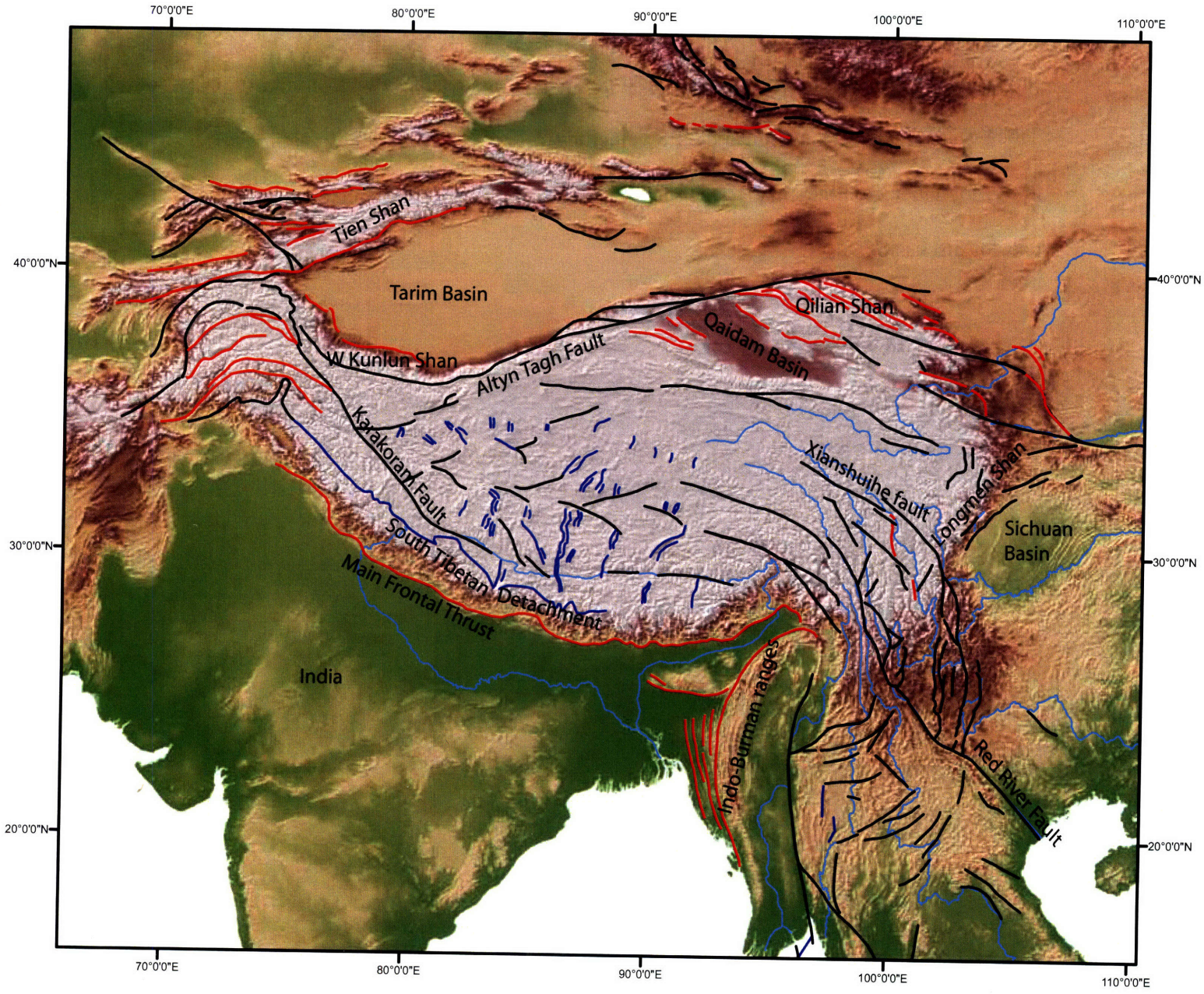
70°0'0"E
80°0'0"E
90°0'0"E
100°0'0"E
110°0'0"E
40°0'0"N
30°0'0"N
20°0'0"N
Tien Shan
Tarim Basin
Qilian Shan
Qaidam Basin
W Kunlun Shan
Altyn Tagh Fault
Karakoram Fault
Xianshuihe fault
Longmen Shan
Sichuan Basin
South Tibetan Detachment
Main Frontal Thrust
India
Indo-Burman ranges
Red River Fault

Figure 1

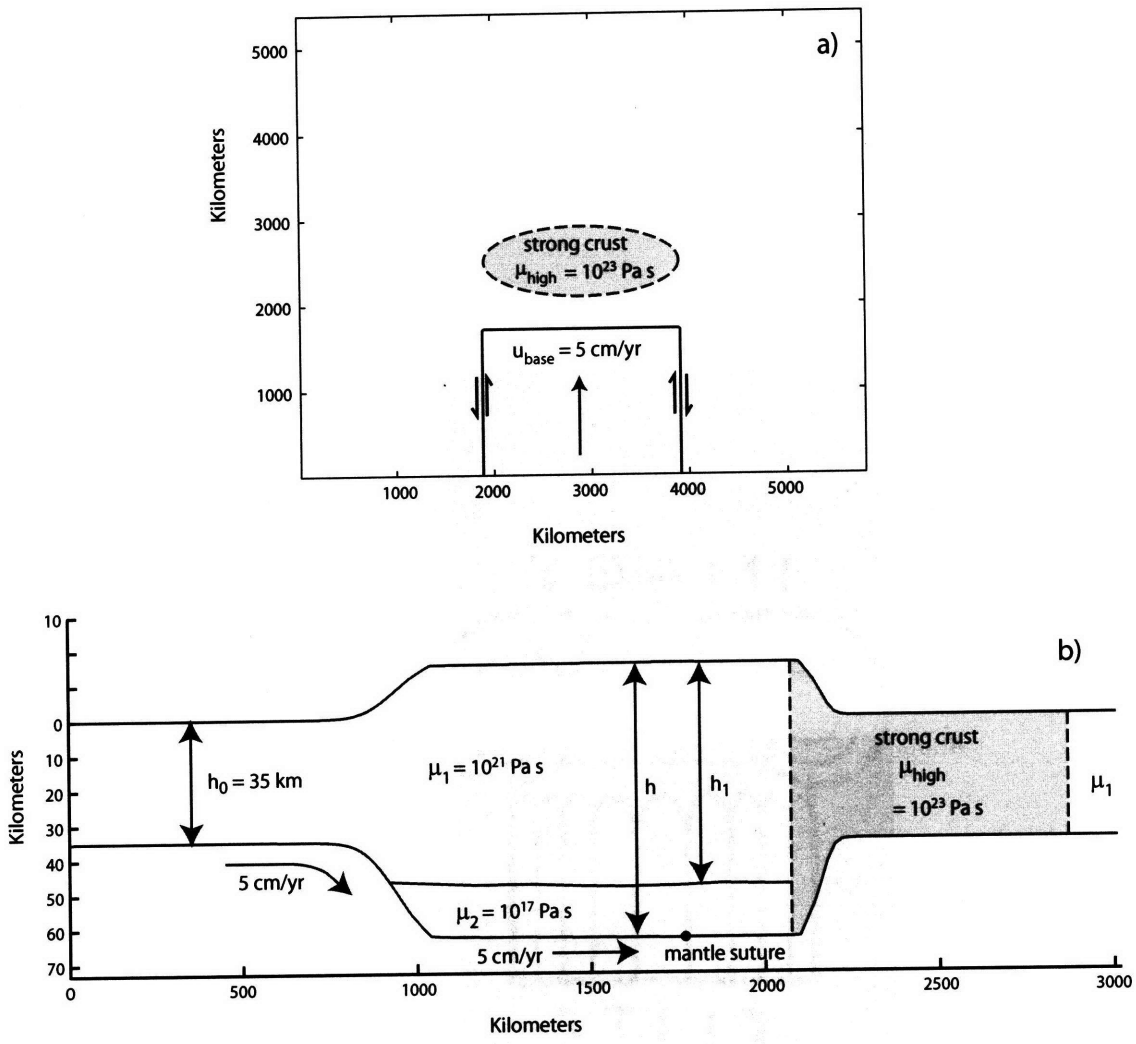
a)
Kilometers
5000
4000
3000
2000
1000
strong crust
$\mu_{high} = 10^{23}$ Pa s
$u_{base} = 5$ cm/yr
1000
2000
3000
4000
5000
Kilometers
b)
Kilometers
10
0
10
20
30
40
50
60
70
$h_0 = 35$ km
$\mu_1 = 10^{21}$ Pa s
h
h_1
strong crust
μ_{high}
$= 10^{23}$ Pa s
μ_1
5 cm/yr
$\mu_2 = 10^{17}$ Pa s
5 cm/yr
mantle suture
0
500
1000
1500
2000
2500
3000
Kilometers

Figure 2

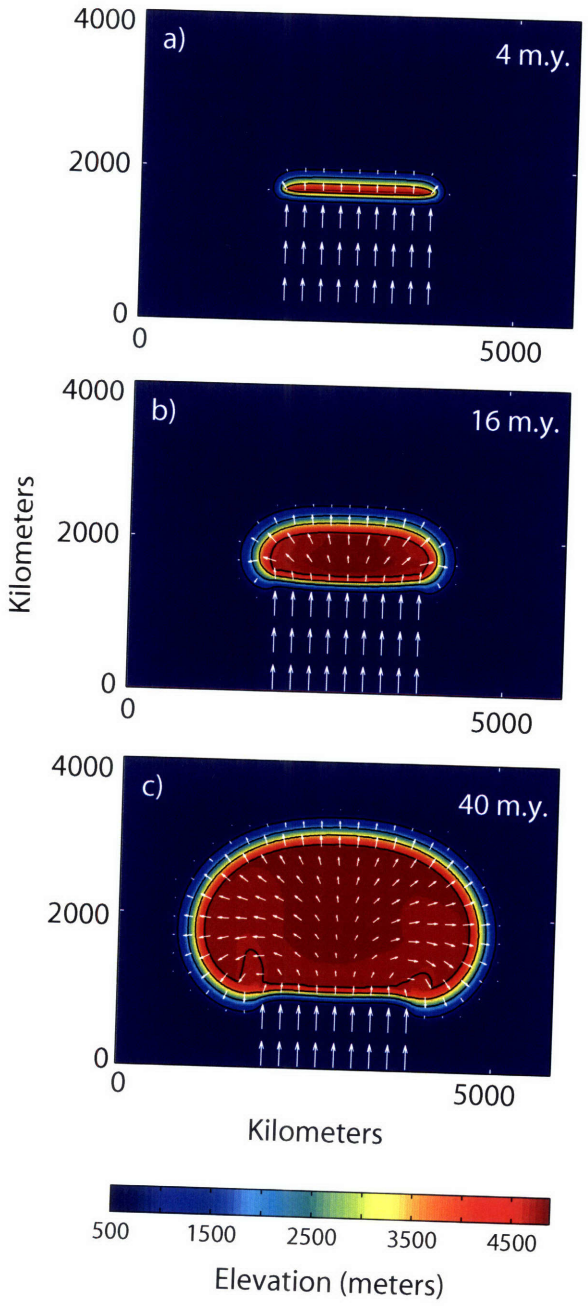
a)
4 m.y.
b)
16 m.y.
c)
40 m.y.
4000
2000
0
0
5000
Kilometers
Kilometers
500
1500
2500
3500
4500
Elevation (meters)

Figure 3

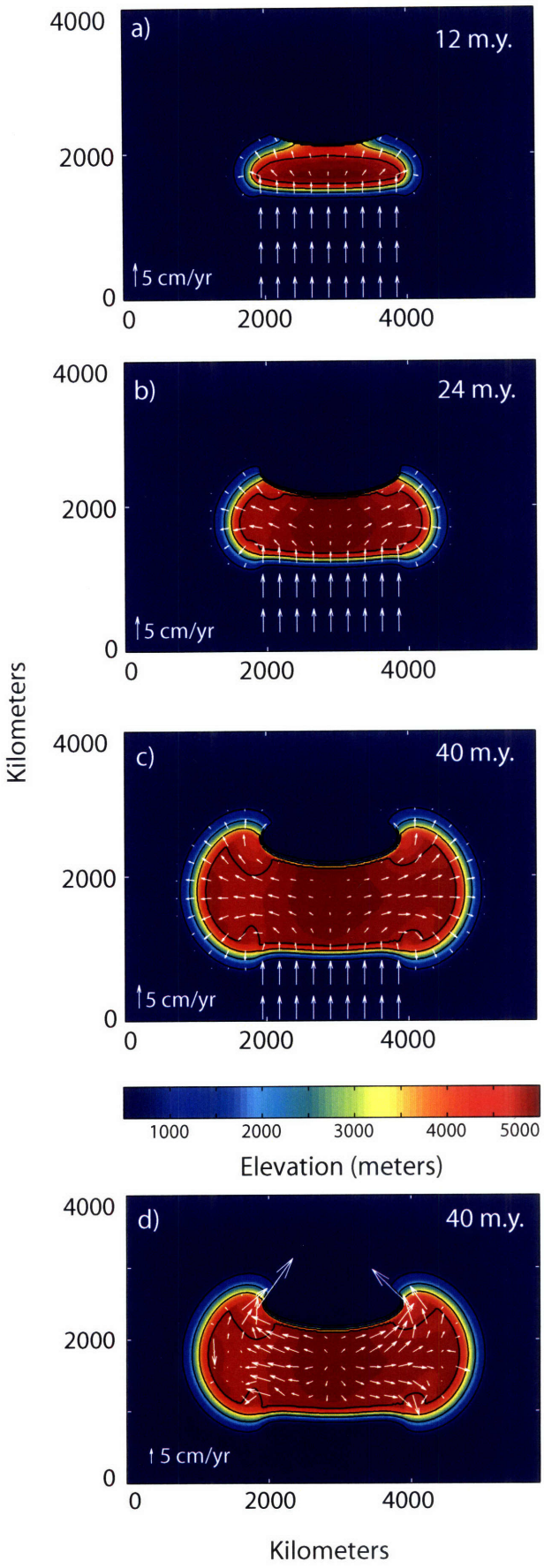
a)
12 m.y.
b)
24 m.y.
c)
40 m.y.
d)
40 m.y.
5 cm/yr
4000
2000
0
0
2000
4000
Kilometers
1000
2000
3000
4000
5000
Elevation (meters)

Figure 4

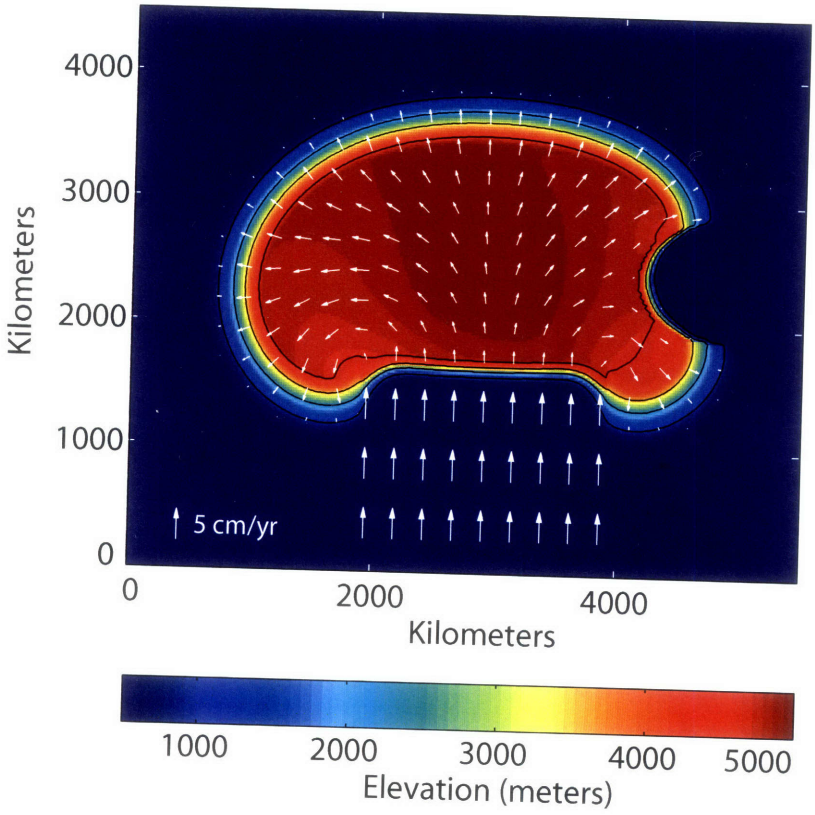
4000
3000
2000
1000
0
Kilometers
5 cm/yr
0
2000
4000
Kilometers
1000
2000
3000
4000
5000
Elevation (meters)

Figure 5

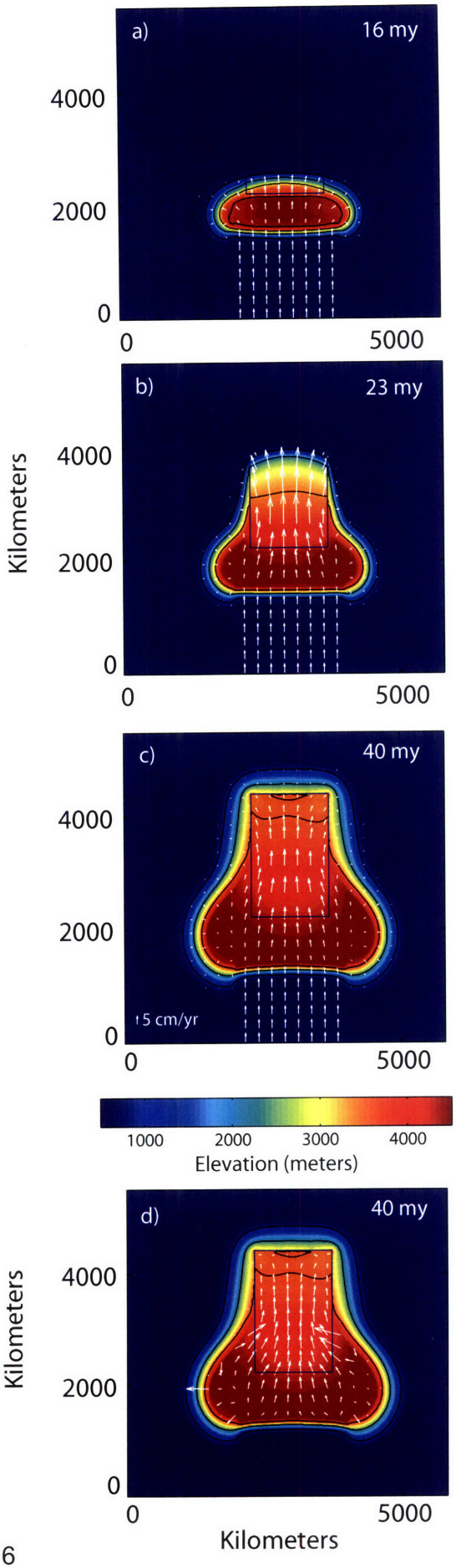
a)
16 my
b)
23 my
c)
40 my
d)
40 my
4000
2000
0
0
5000
Kilometers
5 cm/yr
1000
2000
3000
4000
Elevation (meters)
Kilometers

Figure 6

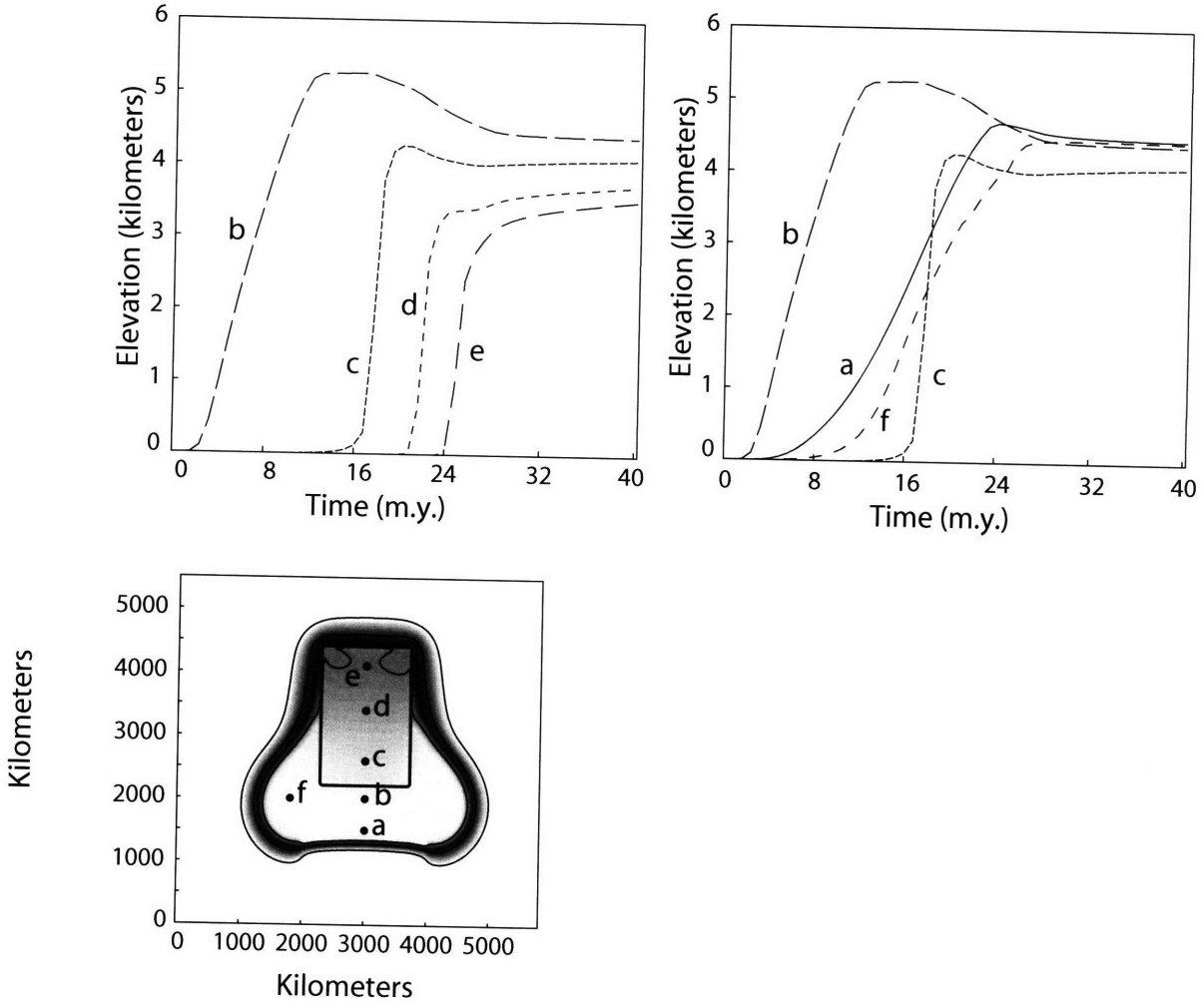
Elevation (kilometers)
Time (m.y.)
b
c
d
e
a
f
Kilometers
Kilometers
0 1000 2000 3000 4000 5000

Figure 7

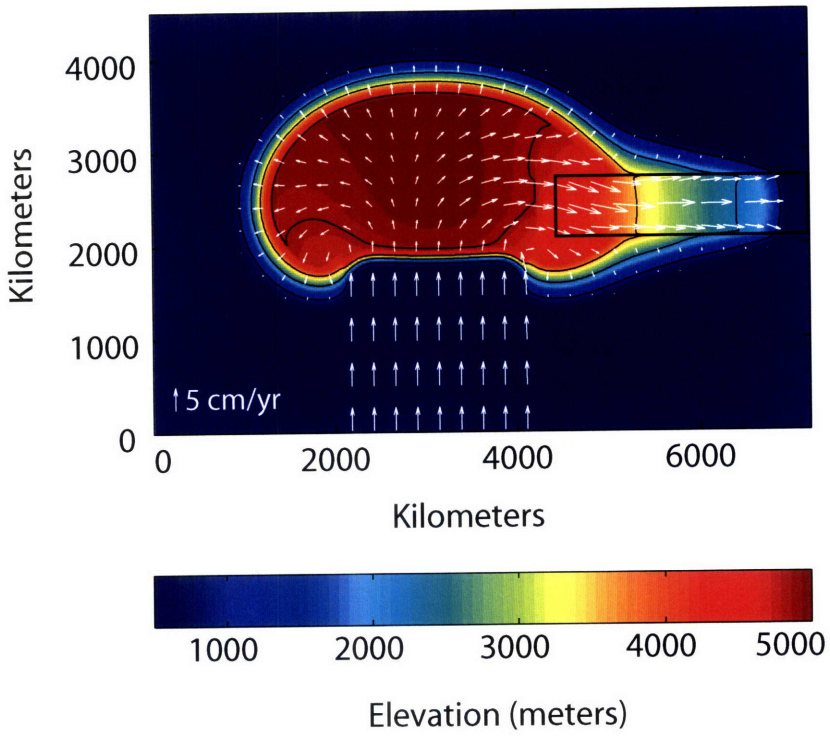
4000
3000
2000
1000
0
Kilometers
5 cm/yr
0
2000
4000
6000
Kilometers
1000
2000
3000
4000
5000
Elevation (meters)

Figure 8

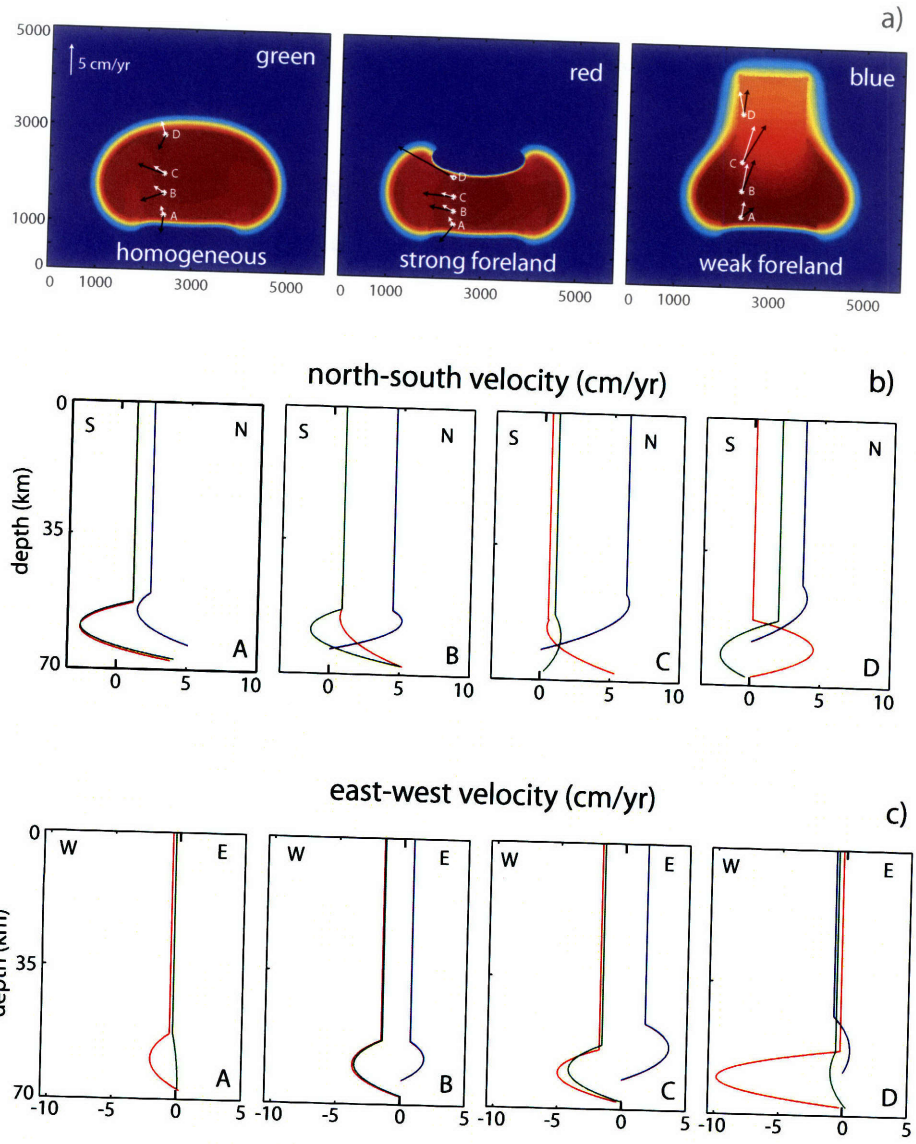
a)
5000
3000
1000
0
5 cm/yr
green
red
blue
D
C
B
A
homogeneous
strong foreland
weak foreland
0
1000
3000
5000
north-south velocity (cm/yr)
b)
depth (km)
35
70
S
N
A
B
C
D
0
5
10
east-west velocity (cm/yr)
c)
W
E
-10
-5

Figure 9

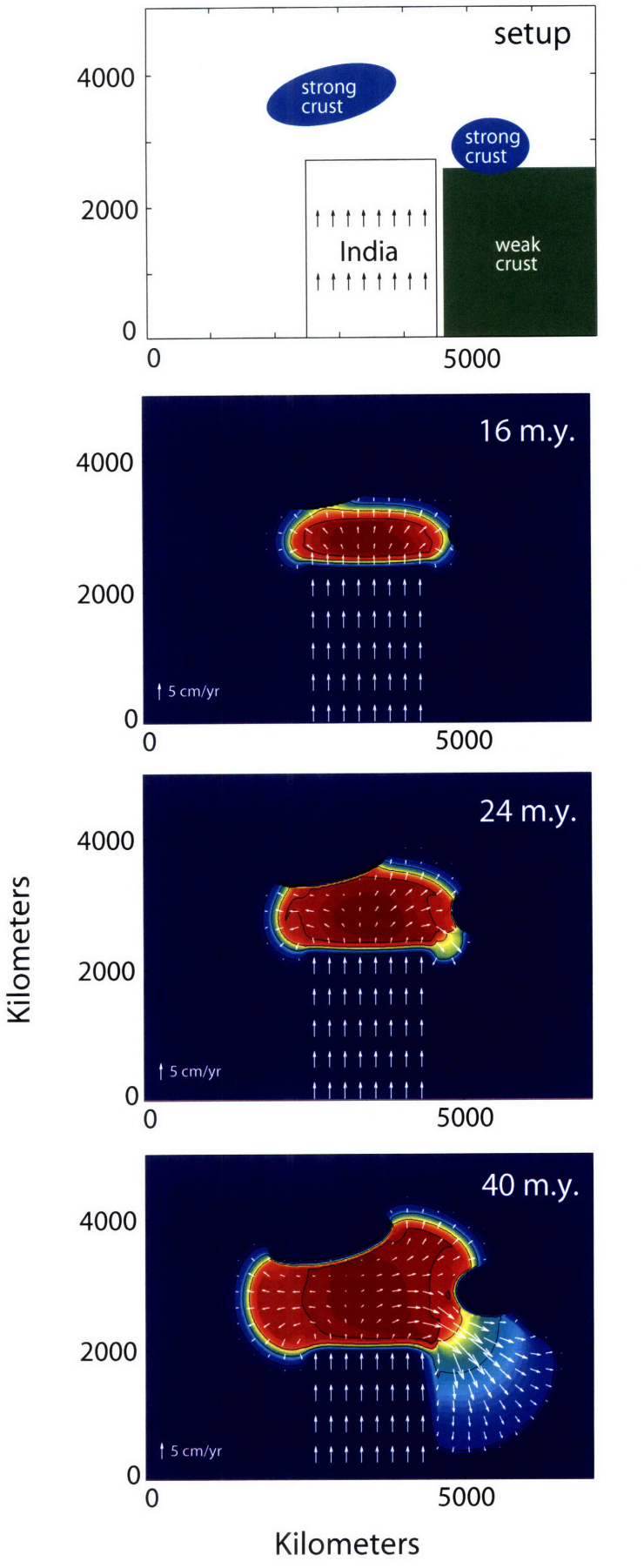
setup
strong crust
strong crust
India
weak crust
16 m.y.
24 m.y.
40 m.y.
5 cm/yr
4000
2000
0
0
5000
Kilometers
Kilometers
1000
2000
3000
4000
5000
Elevation (meters)

Figure 10

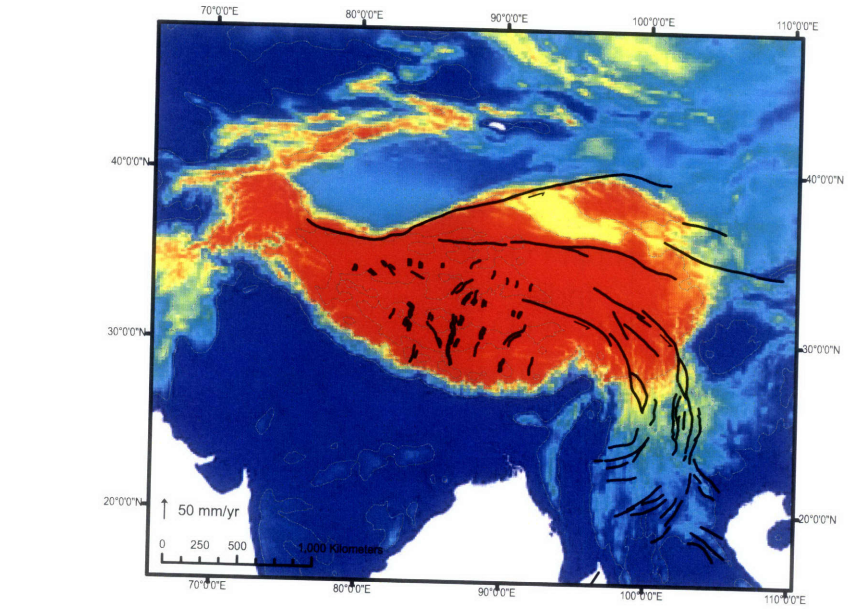
70°0'0"E
80°0'0"E
90°0'0"E
100°0'0"E
110°0'0"E
40°0'0"N
30°0'0"N
20°0'0"N
50 mm/yr
0 250 500 1,000 Kilometers

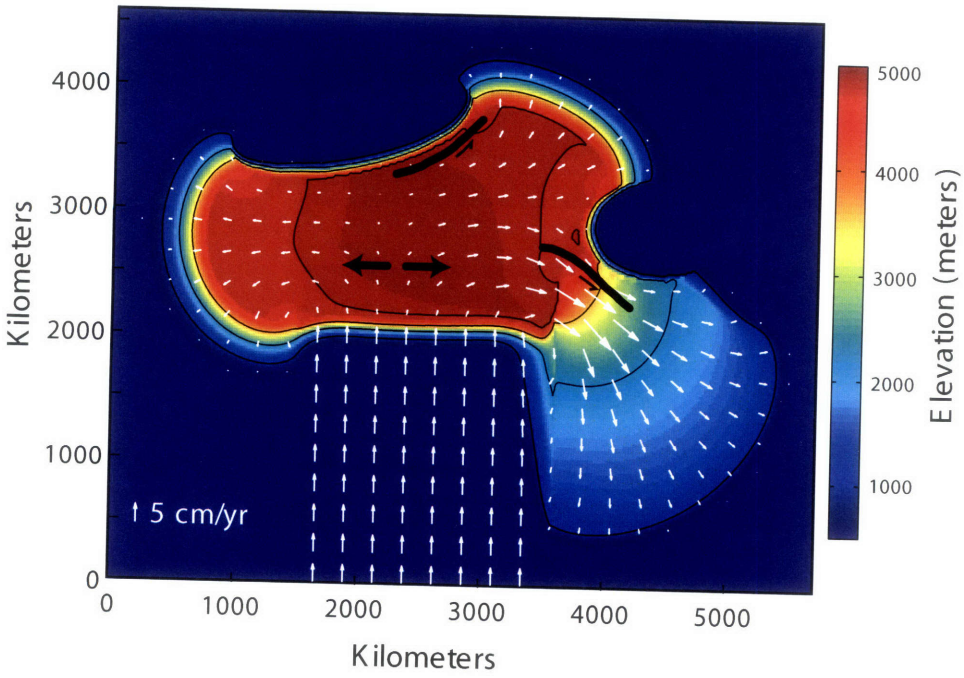
4000
3000
2000
1000
0
Kilometers
0 1000 2000 3000 4000 5000
Kilometers
5 cm/yr
5000
4000
3000
2000
1000
Elevation (meters)

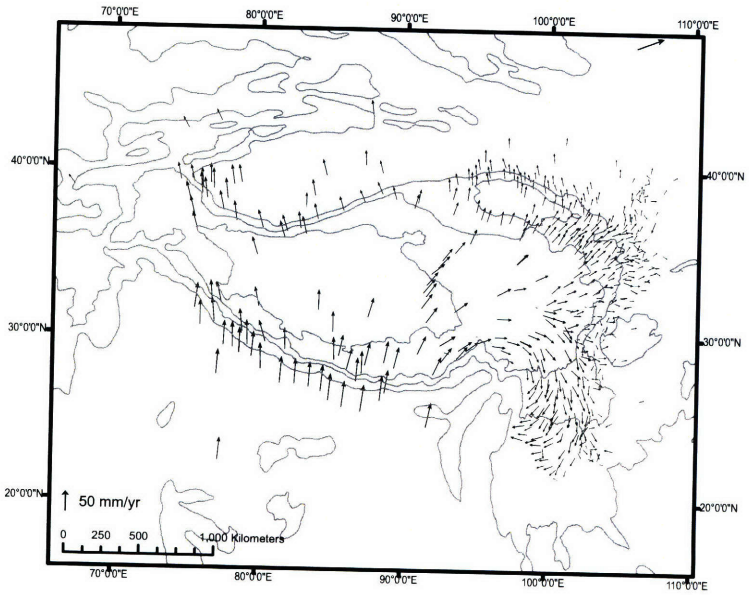
70°0'0"E
80°0'0"E
90°0'0"E
100°0'0"E
110°0'0"E
40°0'0"N
30°0'0"N
20°0'0"N
50 mm/yr
0 250 500 1,000 Kilometers

Figure 11

Chapter 3

Building the central Andes through axial lower crustal flow

Kristen L. Cook[1] and William B. Ouimet[2]

[1]Department of Earth, Atmospheric, and Planetary Sciences, Massachusetts Institute of Technology, Cambridge, MA 02139 USA
[2]Department of Geosciences, Penn State University, University Park, PA 16802, USA

In preparation for submission to *Earth and Planetary Science Letters*

Abstract

The orogen-scale morphology of the Central Andes, which are longitudinally symmetric about ~19°S. correlates with the geometry of the subducting Nazca slab, but is largely independent of local bedrock geology or precipitation. Crustal thickening, as measured by cross-strike width of the orogen above 3000 m and cross-sectional area of the crust, is not well correlated with observed magnitudes of upper crustal shortening. In our interpretation the large-scale morphology is instead correlated with, and controlled by, lithospheric-scale processes and subduction dynamics. Using a semi-analytic, three-dimensional Newtonian viscous flow model, we produce Andean-like topography and distribution of upper crustal shortening during subduction of an oceanic lithosphere eastward beneath the Andes provided that (i) the more steeply-dipping slab segment beneath the central Andes is overlain by weak lower or middle crust (ii) the flat-slab subduction segments to the north and south of this zone are overlain by strong middle and lower crust. and (iii) the steeply-dipping central slab segment is overlain by a narrow, centrally-localized zone of increased crustal shortening shortening. The resulting model orogen displays substantial orogen-parallel flow in the weak lower crust above the steep slab zone. Orogen-parallel flow does not penetrate into the regions of stronger lower crust above the flat slab segments, resulting in a broad, plateau-topped orogen above the central slab segment and narrow but high orogenic segments above the flat-slab region. Redistribution of material through lower crust flow explains the observed mismatch between crustal volume and upper crustal shortening in the Central Andes.

Keywords: Andes, lower crustal flow, Altiplano-Puna plateau

Introduction

The development of high topography in the central Andes, including development of the Altiplano and Puna plateaus, has resulted from Neogene shortening of the South American plate during eastward subduction of the Nazca plate beneath South America (Isacks, 1988). The mechanisms that contribute to crustal thickening and surface uplift remain enigmatic, and much of the plateau exhibits a mismatch between crustal volume and estimates of upper crustal shortening. The thick crust and high topography in the northern Altiplano and the Puna coincide with significant deficits in measured upper crustal shortening, while the central Altiplano has an excess of upper crustal shortening (Kley and Monaldi, 1998). The Central Andes also display a remarkable symmetry in orogen width and cross sectional area, despite a pronounced asymmetry in precipitation and upper crustal lithology. The transition from a wide plateau to a narrower mountain range to both the north and south of the Altiplano coincide with changes in the dip of the subducting Nazca slab – from a steeply dipping slab underneath the Altiplano to a flat slab underneath the regions to the north and south. Such observations suggest that the overall morphology of the Central Andes is largely independent of local geology, upper crustal shortening, and precipitation, and may be largely controlled by orogen-scale dynamics of the lithosphere and underlying subduction systems.

Lower crustal flow has been proposed to explain crustal thickening and surface uplift in the absence of upper crustal shortening in a number of orogens, most notably beneath the eastern Tibetan plateau and its margins (Clark and Royden, 2000). Some authors have proposed that in the central Andes ductile flow within the lower crust redistributes crustal material along strike, translating material away from areas with greater magnitudes of upper crustal shortening and towards areas with lesser magnitudes of upper crustal shortening (Kley and Monaldi, 1998;

Hindle et al., 2005). Mass transfer in the lower crust has also been cited as a potential explanation for crustal thickening and surface uplift in the eastern Cordillera of the Bolivian Andes and in the western Altiplano of southwest Peru starting at ~10 Ma (Barke and Lamb, 2006; Schildgen et al., 2007). In this paper, we explore the potential role of lower crustal flow in controlling the morphology and development of high topography in the central Andes.

Central Andes (12° TO 30° S)

The Andes mountains define the western edge of South America. The orogen is more than 8000 km long and displays large along-strike variations in width, mean elevation, geomorphic character and style of upper crustal deformation. From 2° to ~14° S and 28° to 34° S, the Nazca plate subducts shallowly eastward beneath at Andes (at <10°). This contrasts with subduction beneath the central Andes, where the Nazca plate is smuch steeper (~30°) (Jordan et al.; 1983; Isacks, 1988; Cahill and Isacks, 1992).

The highest and widest parts of the orogen are in the central Andes between 12° and 30° S, culminating in the Altiplano-Puna plateau of southern Peru, Bolivia, and northern Chile (Figure 1). In this region, average elevations of 3.5 to 4 km persist over an area of ~600,000 km^2 (300 km x 2000 km) (Isacks, 1988); maximum orogen widths are on the order of 600-700 km, and crustal thicknesses are as large as 60 to 70 km (Beck et al., 1996). The highest elevations throughout this region are typically mountain peaks associated with Cretaceous-Tertiary volcanic rocks, which rise above the plateau to elevations greater than 6000 m.

The Altiplano-Puna plateau, together with the Western Cordillera, an active volcanic arc, and the Eastern Cordillera, a Miocene thrust belt, define a broad zone with average elevation greater than 3000 m (Figure 1). Near ~19° S, the central Andes reaches its maximum width.

Here the eastern margin of the Andes includes the Subandean zone, an active, thin-skinned fold-thrust belt, and is bordered by an active foreland basin in the Chaco plain. In the northern Altiplano (~14° S) and in the southern Puna (~28° S), the plateau and cordillera are less well-defined. This coincides with a transition to different styles of deformation postulated to result from the presence of flat slab subduction beneath the northern and southern parts of the orogen (Isacks, 1988). Deformation began in the Andes in Jurassic time, but the development of high topography in the central Andes began only after 25 Ma, concurrent with accelerated convergence between the Nazca and South American plates (Allmendinger et al., 1997). In the vicinity of the central Andes, the present rate of convergence between the Nazca and South American plates is ~80 mm/yr (NUVEL-1A: DeMets et al., 1994). Shortening estimates from GPS data in the sub-Andean zones are ~15–20 mm/yr (Norabuena et al., 1998). The pre-Neogene crustal thickness is believed to have been ~30-35 km, requiring an approximate doubling of the crust to reach the current crustal thickness of the Central Andes (Sempere et al., 2002).

Estimates of Upper Crustal Shortening

The cross-sectional area and orogen widths observed in the central Andes are inconsistent with current estimates of upper crustal shortening. Structures that accommodate shortening vary along strike (Figure 2). The Subandean thrust belt, which accommodates much of the shortening in the central part of the Bolivian orocline, disappears to the south, where it is replaced by a series of uplifted basement blocks. To the north, the Subandean thrust belt narrows and disappears into an undifferentiated package of sedimentary rocks metamorphosed to low-grade. This makes it difficult to measure accurately the total magnitude of upper crustal

shortening. Near the axis of symmetry between 17°S and 22°S, many researchers have documented large magnitudes of upper crustal shortening (200-300 km), with some estimates reaching as high as ~530 km (Kley and Monaldi, 1998; McQuarrie, 2002). The higher estimates are greater than the 350 km of shortening expected from the cross-sectional area (Figure 3g) (Kley and Monaldi, 1998). In contrast, shortening estimates in the Puna, between 22°S and 28°S, range from 70 to 120 km. In the northern Altiplano, between 17°S and 14°S, the few existing estimates are even lower, suggesting only ~50 km of shortening (Kley and Monaldi, 1998). The small magnitude of apparent upper crustal shortening in these northern and southern sections of the central Andes is not sufficient to explain current crustal thicknesses (>50 km) and orogen widths (> 300 km) observed here, which correspond to more than ~200 km of upper crustal shortening. We therefore see a mismatch between crustal volume and upper crustal shortening throughout the plateau, with an excess of shortening in the center of the Altiplano and a deficit in the northern Altiplano and Puna (Figure 3g).

Orogen Morphology

The longitudinal symmetry of the Andes can be observed visually (Figure 1) but is highlighted by quantitative analysis of topographic swath profiles constructed perpendicular to the trench (Figure 1b, Figure 2, see Isacks, 1988). The profiles show maximum, minimum and mean elevations averaged across 80 km wide swaths. Using the mean topography from each swath profile, we compiled the cross-sectional area (area under the mean topography profile and above sea-level), the orogen width at 3000 m elevation, and the highest mean elevation (Figure 2).

The along-strike symmetry in cross-sectional area and orogen width is clear when compared to the same data inverted about the axis of symmetry (at ~19°S, where cross-sectional area and orogen width are a maximum). North and south of 19°S, cross-sectional area and orogen width are relatively uniform above the region of steeper slab subduction (from ~14 and 28°S). At the transition to flat slab subduction to the north and south, there is a pronounced decrease in these values. The maximum peak elevations are largely invariant along the length of the orogen and appear unrelated to underlying slab geometry. Relatively small, local variations in width and cross-sectional area, such as occurs around 16° S, are probably related to local processes, but do not significantly affect the large-scale symmetry of the orogen or the clear changes in width and cross-sectional area that occur near 14°S and 28°S. It is likely that the local variations in orogen morphology are related to variable precipitation and drainage patterns along strike.

Regional Bedrock Geology and Structure Style

The bedrock geology and style of structural deformation on the eastern flanks of the Andes vary significantly along-strike and are highly asymmetric (Figure 3) (Allmendinger et al, 1997; Schenk et al., 1998). The northern region is comprised of low-grade, undifferentiated Pre-Cambrian, Paleozoic and Mesozoic meta-sediments. The central region is dominated by a thick sequence of Paleozoic sedimentary rocks that make up the thin-skinned Subandean fold-thrust belt. The southern region is distinguished by Precambrian basement rocks and Paleozoic intrusives deformed in a thick-skinned thrust belt (Schenk et al., 1998). The geology of the west of the Eastern Cordillera is more consistent along strike. Most of the plateau region is covered by Quaternary sediments and Cretaceous to Tertiary volcanic rocks. Mesozoic to Cenozoic intrusive

rocks are found mainly in the coastal cordillera to the west of the Western cordillera and in the northern peaks of the central Andes.

Annual Precipitation

Annual precipitation in the central Andes is also highly asymmetric (Figure 3f) and varies along strike by an order of magnitude. The highest values occur on the steep topographic escarpment abutting the northeastern edge of the plateau in Peru and Bolivia (centered on 15° to 17°S) and low values occur in all other areas of the plateau and associated high topography (Peterson and Russell, 1997) (Figure 3f). Some studies have suggested that increased erosion in areas of high precipitation in the Andes has affected the geomorphic, metamorphic, and structural characteristics of the orogen (Masek et al., 1994; Horton, 1999; Montgomery et al., 2001), but variations in precipitation do not appear to significantly affect the large-scale morphology of the Central Andes, particularly at elevations above 3000 m.

Crustal Flow Modeling

The data summarized above suggest that the topography of the central Andes is tied primarily to the dynamics and geometry of the Nazca/South America subduction boundary rather than to variations in properties such as surface geology or climate. This conclusion, originally discussed and argued by Gephart (1994), motivates us to consider processes that may relate slab geometry to morphology via crustal deformation, and whether these processes could explain the shortening deficit, described above, of the Puna and northern Altiplano.

The role of the lower crust in the development of orogenic plateaus has been discussed in the context of the Altiplano (Kley and Monaldi, 1998; Hindle et al., 2005; Husson and Sempere,

2003; Yang et al., 2003) and the Tibetan Plateau (Bird, 1991; Royden, 1996; Beaumont et al., 2001), as well as in theoretical models of plateau development (Vanderhaeghe et al., 2003). Central to this discussion is the assumption that the crust may, under appropriate conditions, become weak enough to enable ductile channel flow in response to lateral pressure gradients resulting from variations in crustal thickness. This enables a lateral flux of deep crustal material beneath the plateau with minimal deformation of the upper crustal layer, and may effectively decouple the motion of the upper crust from that of the mantle. Experimental, observational, and theoretical studies suggest that the strength of continental crust can decrease significantly at high temperatures and/or in the presence of fluids or partial melt (Kohlstedt et al., 1995; Rosenberg and Handy, 2005).

Previous modeling studies of lower crustal flow in the Andes have focused on east/west lower crustal flow from Eastern and Western Cordillera into the Altiplano (Husson and Sempere, 2003), or have examined only north to south lower crustal flow with a prescribed geometry for the Andes topography and an imposed distribution of deformation (Yang et al., 2003). Our approach employs a three-dimensional viscous flow model to explore the relationships between slab dip, crustal strength, lower crustal flow and the topography, uplift, and orogen-scale symmetry of the central Andes.

Modeling Framework

The modeling approach adopted in this paper is identical to that of Cook and Royden (2008) (see also Royden, 1996, and Shen et al., 2001). The crust is treated as an idealized incompressible Newtonian viscous fluid with two layers representing the upper and lower crust. Viscosity is allowed to vary laterally in both layers, but is depth-invarient within each layer.

Deformation is fully described by the Stokes and continuity equations. With appropriate boundary conditions, we obtain analytical expressions for velocity at the surface of the crust and the change in crustal thickness over time at length scales that are similar to and longer than the thickness of the crust. A detailed discussion of the methods, parameters and assumptions can be found in Cook and Royden (2008).

In this study, we do not model the thermal state of the crust explicitly. The relationship between temperature and the bulk strength of the crust is neither straightforward nor well-constrained, requiring assumptions about composition, hydration, and temperature at depth. Instead, the model specifies the viscosity in the lower crust directly as a response to the evolving crustal thickness. Initially, the crust has a uniform viscosity throughout; when it thickens beyond a specified value, the viscosity of the lower crust is reduced as the lower crustal layer thickens and is a function of crustal thickness. Once the total crustal thickness reaches a critical value, the viscosity stabilizes at a prescribed minimum value. If the crust subsequently thins to be less than this critical value, the viscosity of the lower crust is again allowed to depend on crustal thickness, increasing as the crust thins.

Model Setup

A schematic cross-section (Figure 4) illustrates the set-up and parameters used in this study. Crustal deformation is driven by "plate-like" mantle velocities imposed at the base of the crust. Topography evolves in response to the interaction between this forcing and the pressure gradients created by the evolving topography itself. We assume a uniform initial continental crustal thickness of 35 km and an initial oceanic crustal thickness of 1 km. The 1 km of oceanic crust represents an estimate of material incorporated into the Andean orogen from the subducted

slab while the rest of the oceanic crust is subducted. The crust is assigned an initial viscosity of 10^{21} Pa·s.

The total convergence across the subduction boundary is specified at 80 mm/yr. In most regions, the zone of convergence at the base of the crust is given a slow rate (0.75 cm/yr) of eastward motion, and the South American plate is given a slow rate (1.5 cm/yr) of westward motion representing underthrusting of the Brazilian Shield. More rapid eastward motion of the convergent boundary at the base of the crust and slightly more rapid westward motion of the South American plate are applied to the region that will develop into the center of the Bolivian orocline, enhancing the shortening of the South American plate in this region. We refer to this zone as the orocline zone. The convergent boundary is not straight and convergence is specified to be parallel to the axis of symmetry. (This is similar to the observed direction of convergence between the Nazca and South American plates).

Model results

We evaluated many different subduction zone geometries, basal velocities, shortening patterns, and viscosity structures before arriving at the model results illustrated in Figures 5 through 8 (for parameter values see Table 1). The most Andean-like results occur with a subduction boundary that is divided into several regions. In the orogenic segment underlain by a more steeply subducting slab (between14 and 28°S), the viscosity of the lower crust begins to drop when the crust reaches a thickness of 50 km and arrives at its minimum value of 10^{17} Pa s when the crust reaches a thickness of 65 km. In the orogenic segments underlain by flat slab subduction (north of 14°S and south of 28°A) the lower crust is not allowed to weaken and the viscosity remains uniform throughout the crust. Embedded in the center of the steep slab zone is

a narrower oroclinal zone where the convergent boundary at the base of the crust moves eastward more rapidly than to the north and south (while total convergence remains uniform along the convergent boundary). This corresponds to the area where the eastward motion of the Nazca subduction boundary is more rapid than in the areas to the north and south, and where the magnitude of underthrusting of the Brazilian Shield is also greater. This model effectively generates topography with a morphology generally similar to that of the central Andes (Figure 6).

The increased magnitude of crustal shortening along the eastern side of the central orocline region is accommodated by orogen-parallel flow of deep crust to the north and south. Orogen parallel flow is restricted to the area of weak lower crust, hence to the hotter crust above the zone of steeper subduction. Because the lower crust does not weaken until the crust reaches a prescribed critical thickness, there is little axial flow of crust during the initial stages of orogen growth. As the crust in the steep slab region reaches the prescribed critical crustal thickness, the lower crustal viscosity decreases and deep crustal material flows away from the central region of highest shortening towards the north and south. This results in a redistribution of crust as illustrated by cross-sections extracted from model topography (Figure 7, 8).

Flow within the low viscosity crustal layer occurs under low pressure gradients, so that flow within the weak crust region continues until the elevation above the weak crust region is the nearly the same along- and across-strike (Figure 8). As the lower crust flows northward and southward from the center of the orogen, the cross-sectional width and integrated topography across the model orogen also become similar throughout the weak crust region. Thus the amount of crust added to the orogen, as estimated from the cross-sectional area of the orogen, is similar along the entire weak crust region of the orogen despite the fact that central part of the weak

crust region experiences approximately three times as much upper crustal orogen-perpendicular shortening as the weak crust regions to the north and south. (Figure 9). This is consistent with observations from the Andes, where crustal shortening estimates above the steep slab region are much higher between 17°S and 22°S (>300 km) and much lower to the north (<50 km) and south (70-120 km). (Note, however, that our model produces more shortening than is observed in the Andes, with a maximum of ~740 km in the center of decreasing to ~260 km to the north and south.).

Discussion

Our results suggest that the large-scale morphology of the Central Andes can be mostly explained by the interaction between subduction geometry and large-scale variations in upper crustal shortening along the length of the Andean belt. Figure 3 shows that this large-scale morphology reflects the dip of the subducting slab but is largely insensitive to variations in local shortening, lithology, and precipitation. Within the orogen, a plateau with little along-strike variation in width and cross-sectional area develops as the lower crust weakens above the steeply dipping segment of the Nazca slab, while flow into the region above the flat slab segments is blocked by the presence of a strong lower crust.

In this paper, our goal is not to produce a replica of the central Andes, in geometry nor in temporal evolution, but rather to gain insight into the role of the deep crustal in the development of large-scale morphology and its relationship to subduction dynamics and lithospheric rheology. The model presented here is simplified as compared to the Andean orogen and ignores much of the complexity of crustal processes and regional geology. It represents a possible end-member model meant to highlight the importance of a single process in orogen development. For

example, we have not fine-tuned the model topography above the flat-slab zones, where the orogen is narrow and steep; the high model elevations in these regions are artifacts of the model implementation. While a combination of processes have contributed to the evolution of the Andes, the results presented here show that axial lower crustal flow partitioned by large-scale subduction dynamics is responsible for much of the overall morphology of the Central Andes. This also presents a viable and straightforward explanation for the discrepancies between crustal shortening estimates and crustal volume in the Altiplano.

Subduction angle and crustal temperature

The morphology of the Andes is strongly correlated with the dip of the subducting Nazca Plate, with a wide plateau over a steeply dipping segment, and a narrow orogen over flat slab segments. This correlation may arise from the effect of slab dip on the thermal structure of the overriding plate. A gently dipping slab prevents the formation of a mantle wedge and instead places relatively cold oceanic crust at the base of the upper plate. This is thought to result in crust that is colder, stronger, and less ductile above regions of flat slab subduction (Gutscher, 2002). More steeply dipping slab segments allow the development of a mantle wedge, higher temperatures at the base of the crust, and the introduction of fluids and partial melt (Gutscher, 2002). The higher temperatures and possible introduction of fluids or partial melt will weaken the crust above steeply dipping slab segments and make the lower crust more susceptible to weakening and ductile flow (Kohlstedt et al., 1995; Rosenberg and Handy, 2005). The effect of slab dip can be seen in the pattern in heat flow in the Andes, as several studies find that heat flow is highest in the Altiplano region and drops off to the north and to the south (Henry and Pollack, 1988; Springer and Förster, 1998). The correlation that we see between morphology and slab dip

is consistent can therefore be explained by cooler temperatures and a stronger lower crust above the flat slab zone blocking longitudinal flow in the lower crust.

Crustal shortening

The distribution of shortening imposed in our modeling is based on estimates from the Central Andes indicating that the center of the Altiplano has experienced more shortening than the regions to the north and south. There are several proposed explanations for the inferred increase in the amount shortening at the center of the Bolivian Orocline. Lamb and Davis (2003) suggest that a drier Late Cenozoic climate in the central Andean region resulted in a sediment-starved subduction trench, causing high plate friction and the shear stress needed to support high topography. Another possibility is that an oceanic plateau may have collided with the South American plate, forcing it to shorten as it was dragged under the South American craton (eg. Gutscher et al., 1999). Oblique convergence prior to 15 Ma and the geometry of the margin may also have affected the distribution of shortening (McQuarrie, 2002). The correspondence between the location of maximum upper crustal shortening and the center of the steep slab zone hints at a link between shortening and slab geometry. Regardless of the reasons for the increased shorting in the central Altiplano, our modeling suggests that it is balanced by an outward flow of lower crust.

Effects of erosion and lithology

The large-scale symmetry of the Andes, as shown in figure 3, appears to be unaffected by along-strike variations in lithology and erosion rate. The influence of lower crustal flow is largely confined to regions of thick crust and high topography because flow can only occur in

regions with a weak lower crust. However, the slope and width of the lower Andean flanks may be controlled in part by properties and processes in the upper crust. These include erosion and upper crustal lithology. In particular, the width and slope of the Andean flanks below 3 km appear sensitive to lithology and precipitation, and erosion rate (Figure 3). A number of studies (Masek et al., 1994; Horton, 1999; Montgomery et al., 2001; Allmendinger et al., 1997) have related variations in precipitation, erosion rate, and lithology to variations in morphology along strike in the Andes. Our modeling, and the large-scale symmetry described above, suggests that these processes primarily influence the flanks of the orogen and the regions below ~3 km elevation, while the higher elevation regions and orogen-scale morphology remain largely unaffected.

Conclusions

The present morphology and axial symmetry of the Andean belt is independent of widespread variations in along-strike magnitude of upper crustal shortening, bedrock geology and precipitation. The persistence of axial symmetry despite these variations, and the correlation between changes in orogen morphology and the dip of the subducting slab suggest that lithospheric-scale orogenic processes related to slab dip control the regional-scale crustal evolution and morphology of the central Andes.

Our simple, semi-analytic, viscous flow model highlights the interaction between slab dip, lower crustal flow, and the development of topography in the Altiplano region of the Andes. As lower crust above the more steeply dipping segment of the subducting slab becomes hot and weak, increased shortening in the center of the Andes drives longitudinal flow of lower crust along strike to the north and south. Longitudinal flow does not penetrate into the flat slab

regions, presumably because the crust there is stronger and the lower crust is unable to flow. The redistribution of material results in an apparent discrepancy between local crustal volume and surface shortening. Our results indicate that lower crustal flow exerts a fundamental control on the distribution of topography along and across the Andes.

Acknowledgements

This work was supported by the NSF Continental Dynamics program (EAR-0003571), in collaboration with Leigh Royden and Clark Burchfiel at Massachusetts Institute of Technology. Thanks to Taylor Schildgen for helpful comments and feedback.

References

Allmendinger, R. W., T. E. Jordan, Kay, S. M., and B. L. Isacks (1997). The evolution of the Altiplano-Puna plateau of the Central Andes. *Annual Reviews of Earth and Planetary Science* 25: 139-74.

Barke, R., and Lamb, S., (2006). Late Cenozoic uplift of the Eastern Cordillera, Bolivian Andes: *Earth and Planetary Science Letters*, v. 249, p. 350-367.

Beaumont, C., Nguyen, M., Jamieson, R.A., and S. Ellis (2006). Crustal flow modes in large hot orogens, in *Channel Flow, Ductile Extrusion and Exhumation of Lower-mid Crust in Continental Collision Zones,* edited by R. D. Law, M. Searle, and L. Godin, *Geological Soc. London Spec. Publ., 268,* pp. 91-145.

Beck, S. L., Zandt, G., Myers, S.C., Wallace, T.C., Silver, P.G., and Drake, L., (1996). Crustal thickness variations in the central Andes. *Geology* 24 (5): 407-410.

Bird, P. (1991). Lateral extrusion of lower crust from under high topography, in the isostatic limit, *J. of Geophys. Res., 96*, 10,275-10,286.

Cahill, T. and B. L. Isacks (1992). Seismicity and Shape of the Subducted Nazca plate. *Journal of Geophysical Research* 97 (B12): 17,503-17,529.

Clark, M. and L. Royden (2000). Topographic Ooze: Building the Eastern Margin of Tibet by Lower Crustal Flow. *Geology* 28 (8): 703-706.

Cook, K.L. and Royden, L.H. (2007) The influence of crustal strength variations on the development of collisional plateaus, with application to Tibet, Journal of Geophysical Research, *in press.*

Demets, C., Gordon, R.G., Argus, D.F., and Stein, S., (1994). Effect of recent revisions to the geomagnetic reversal time scale on estimates of current plate motions. *Geophysical Research Letters* 21 (20): 2191-2194.

Elger, K., Oncken, O., and Glodny, J., (2005). Plateau-style accumulation of deformation: Southern Altiplano. *Tectonics*, v. 24, TC4020, doi: 10.1029/2004TC001675.

Garzione, C.N., Molnar, P., Libarkin, J.C., and MacFadden, B.J., (2006). Rapid late Miocene rise of the Bolivian Altiplano: Evidence for removal of mantle lithosphere. *Earth and Planetary Science Letters*, v. 241, p. 543-556.

Gephart, J.W., (1994). Topography and subduction geometry in the central Andes: Clues to the mechanics of a noncollisional orogen. *Journal of Geophysical Research*, v. 99, p. 12279–12288.

Ghosh, P., Garzione, C.N., and Eiler, J.M., (2006). Rapid uplift of the Altiplano revealed through ^{13}C-^{18}O bonds in paleosol carbonates. *Science*, v. 311, p. 511-514.

Gregory-Wodzicki, K. M. (2000). Uplift History of the Central and Northern Andes: A review, *Geological Society of America Bulletin* 112 (7): 1091-1105.

Gubbels, T.L., Isacks, B.L., Farrar, E., (1993). High-level surfaces, plateau uplift, and foreland development, Bolivian central Andes., *Geology*, v. 21, p. 695-698.

Gutscher, M.-A., Olivet, J.-L., Aslanian, D., Eissen, J.-P., Maury, R., (1999). The ''lost Inca Plateau'': cause of flat subduction beneath Peru? *Earth Planet. Sci. Lett.* 171, 335– 341.

Henry, S.G., and Pollack, H.N., (1988). Terrestrial heat flow above the Andean subduction zone in Bolivia and Peru, *Journal of Geophysical Research* 93, 153–162.

Hindle, D., Kley, J., Oncken, O., Sobolev, S., (2005). Crustal balance and crustal flux from shortening estimates in the Central Andes, *Earth and Planetary Science Letters*, 230, 113-124.

Horton, B. K. (1999). Erosional control on the geometry and kinematics of thrust belt development in the central Andes, *Tectonics* 18: 1292-1304.

Husson, L. and T. Sempere (2003). Thickening the Altiplano crust by gravity-driven crustal channel flow, *Geophysical Research Letters* 30, 5, 1243, doi:10.1029/2002GL016877.

Isacks, B. L. (1988). Uplift of the Central Andean plateau and the bending of the Bolivian Orocline, *Journal of Geophysical Research* 93: 13,841-13,854.

Jordan, T. E., B. L. Isacks, et al. (1983). Andean tectonics related to geometry of subducted Nazca plate., *Geological Society of America Bulletin* 94: 341-361.

Kley, J. and C. R. Monaldi (1998). Tectonic shortening and crustal thickness in the Central Andes: How good is the correlation? *Geology* 26 (8): 723-726.

Kohlstedt, D. L., Evans, B., Mackwell, S. J., (1995). Strength of the lithosphere: Constraints imposed by laboratory experiments, *J. Geophys. Res.* 100, 17587-17602.

Lamb, S. and P. Davis (2003). Cenozoic climate change as a possible cause for the rise of the Andes., *Nature* 425.

Lamb, S., and Hoke, L. (1997). Origin of the high plateau in the Central Andes, Bolivia, South America. *Tectonics*, v. 16, no. 4, p. 623-649.

Masek, J. G., B. L. Isacks, et al. (1994). Erosion and tectonics of margins of continental plateaus., *Journal of Geophysical Research* 99: 13,941-13,956.

McQuarrie, N. (2002). Initial plate geometry, shortening variations, and evolution of the Bolivian Orocline., *Geology* 30 (10): 867-870.

Montgomery, D. R., G. Balco, et al. (2001). Climate, tectonics, and the morphology of the Andes., *Geology* 29 (7): 579-582.

Norabuena, E., L. Leffler-Griffin, et al. (1998). Space Geodetic Observations of Nazca–South America Convergence Across the Central Andes., *Science* 279.

Peterson, Thomas C. and Russell S. Vose, 1997: An overview of the Global Historical Climatology Network temperature data base, *Bulletin of the American Meteorological Society,* 78, 2837-2849.

Rosenberg, C., and M. Handy (2005), Experimental deformation of partially melted granite revisited: implications for the continental crust, *J. Metam. Geol.*, 23, 19-28.

Royden, L. H. (1996). Coupling and decoupling of crust and mantle in convergent orogens: Implications for strain partitioning in the crust, *Journal of Geophysical Research* 101 (B8): 17,679-17,705.

Schenk, C. J., Viger, R. J., and Anderson, C. P., 1998, U.S. Geological Survey Open-File Report 97-470D. Maps showing Geology, Oil and Gas Fields, and Geologic Provinces of the South America Region., U.S. Department of the Interior.

Schildgen, T.F., Hodges, K.V., Whipple, K.X., Reiners, P.W., and Pringle, M.S., (2007), Uplift of the western Altiplano revealed through canyon incision history, Southern Peru, *Geology* 35 (6), 523–526, doi: 10.1130/G23532A.

Sempere, T., G. Carlier, et al. (2002). Late Permian–Middle Jurassic lithospheric thinning in Peru and Bolivia, and its bearing on Andean-age tectonics, *Tectonophysics* 345: 153–181.

Shen, F., L. H. Royden, et al. (2001). Large-Scale Crustal Deformation of the Tibetan Plateau., *Journal of Geophysical Research* 106 (B4): 6793-6816.

Springer, M., and Förster, A., (1998). Heat-flow density across the Central Andean subduction zone, *Tectonophysics* 291, 123-139.

Vanderhaeghe, O., S. Medvedev, P. Fullsack, C. Beaumont, and R. A. Jamieson (2003). Evolution of orogenic wedges and continental plateaux: insights from crustal thermal-mechanical models overlying subducting mantle lithosphere, *Geophys. J. Int., 153*, 27-51.

Victor, P., Oncken, O., and Glodny, J., (2004), Uplift of the western Altiplano plateau: evidence from the Precordillera between 20 and 21°S (northern Chile): *Tectonics*, v. 23, TC4004, doi: 10.1029/2003TC001519.

Yang, Y. and Liu, M., (2003). A 3-D geodynamic model of lateral crustal flow during Andean mountain building, *Geophysical Research Letters* 30, 10, doi:10.1029/2003GL038303.

Figure Captions

Figure 1: (a) Topography of the central Andes (GTOPO30) and Pacific Ocean bathymetry (ETOPO5), rotated such that the dominant plate convergence direction for the past 25 Ma is oriented east/west to illustrate the large scale symmetry in the topography. Note the regions of flat-slab subduction bounding the northern and southern margins of the central Andes, accentuating the symmetry. The axis of symmetry is at ~19°S. (b) Comparison of cross sections at analogous locations north and south of the axis of symmetry. Note the similarities in width and elevation.

Figure 2: Simplified geologic map of the Central Andes. Geology from Schenk et al., 1998.

Figure 3: Topographic analysis of the central Andes. (a) Example of one of the topographic swath profiles used in our analysis (Cross Section 27, at ~19°S), showing how cross-sectional area, width and peak elevations were calculated. The topographic data used for all swaths is GTOPO30 data, 888 m grid spacing. The profiles for maximum, minimum and mean elevations are based on a 80 km wide window. (b) Location and key for 59 topographic swath profiles, showing the axis (parallel to the trench) from which profiles were extracted perpendicularly. Profiles were analyzed to investigate specific trends along the orogen length, such as cross-sectional area above sea level (c), width of the 3000 m contour (d), and peak mean elevation (e). Shaded regions on each plot are the respective beginnings of the flat-slab regions. Each trend is plotted N to S, and flipped S to N at the axis symmetry. (f) Plot showing maximum annual precipitation variation along strike. Maximum annual precipitation values were calculated from swaths of precipitation data equal in extent to the topographic swaths. The interpolated DEM of

peak annual precipitation (not shown) was derived from GHCN Version 2 Global Precipitation data set, Peterson and Russell, 1997. (g) shortening estimates along strike, black line indicates the amount of shortening expected based on cross-sectional area (after Kley and Monaldi, 1998, figure 2)

Figure 4: Schematic cross-section of the Andes at ~19° S showing basic parameters used in the model (crustal thicknesses, viscosities, convergence velocities, etc.).

Figure 5: Boundary conditions and model set-up motivated by topography symmetry and geometry of the Nazca/South America subduction zone boundary. (a) Topographic symmetry. (b) Plan view model set-up. (c) Model topography after 30 My. Flat-slab zones modeled as strong crust where no lower crustal flow occurs. Shortening is focused at the center of the Bolivian Orocline. Deformation is driven by moving the subduction zone to the east; note the initial and final positions of the subduction zone boundary.

Figure 6: Time-series depicting the evolution of topography during one model run for 30 My. Model time 3 My refers to 27 My before present, 18 My refers to 12 My before present, and so on. Each image represents a DEM of elevations.

Figure 7: (a) Model topography after 30 Ma, and (b) 4 topographic cross-sections showing final topography. Plateau elevations are lower within the central Andes because crust is weaker and flows. (c) Plot showing volume/area change in each cross-section through time when compared

to the volume/area that's expected from how much convergence and shortening has occurred. This is calculated by taking the crustal volume/area at any point and subtracting by the amount of crustal volume/area expected simply from the amount of shortening experienced. This plot shows the effect of axial lower crustal flow: material flows away from the center towards the north and south, resulting in crustal deficits and volume addition.

Figure 8: (a) Cross-sections of model topography after 6, 12, 18, and 24 My of orogen growth. Locations and symbology of cross-section lines are the same as in Figure 7. (b) Mean topography from swath profiles at analogous locations in the Andes.

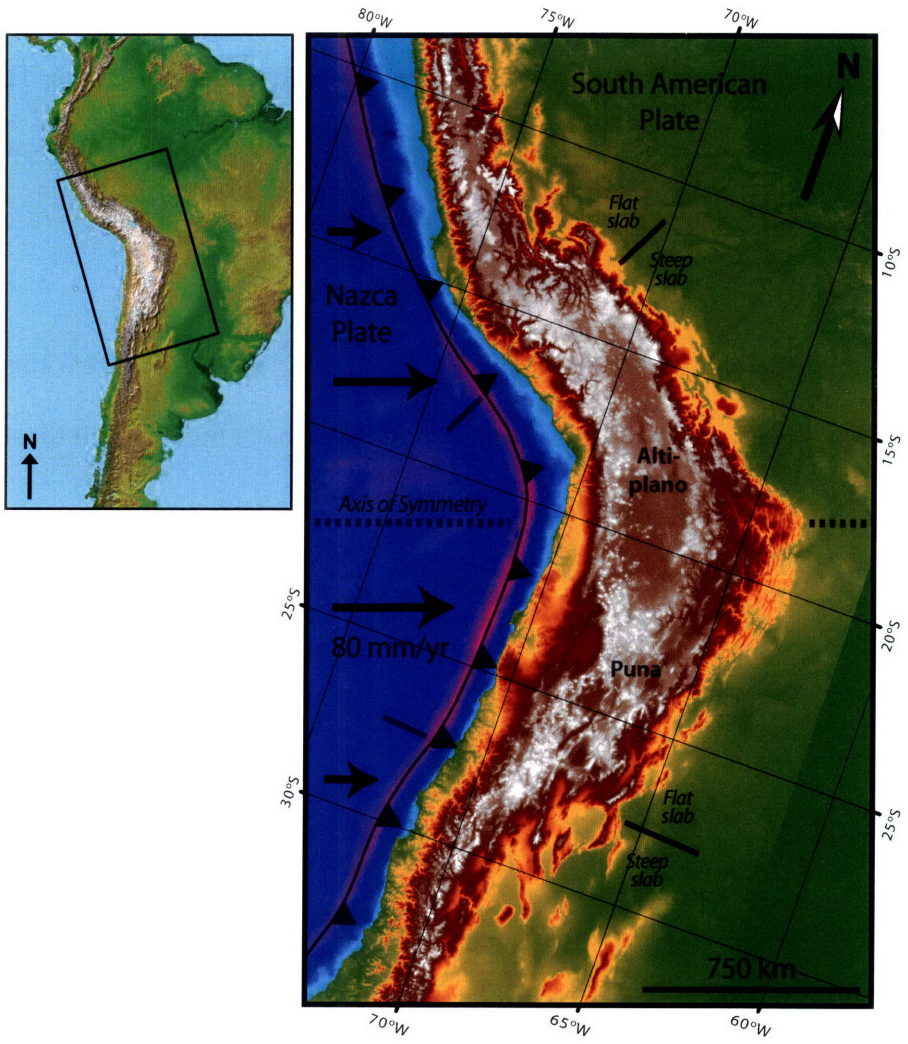
80°W
75°W
70°W
N
South American Plate
Flat slab
Steep slab
Nazca Plate
Alti-plano
Axis of Symmetry
10°S
15°S
20°S
25°S
30°S
80 mm/yr
Puna
Flat slab
Steep slab
750 km
70°W
65°W
60°W
N

Figure 1

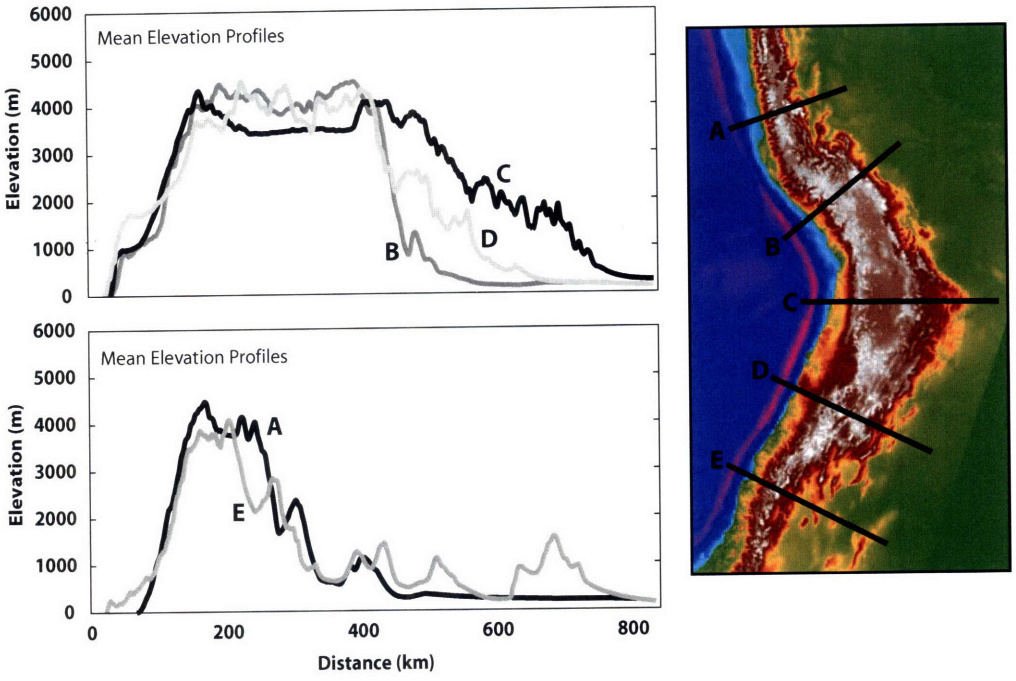
Mean Elevation Profiles
Elevation (m)
6000
5000
4000
3000
2000
1000
0
A
B
C
D
E
Mean Elevation Profiles
Elevation (m)
0
200
400
600
800
Distance (km)

Figure 1b

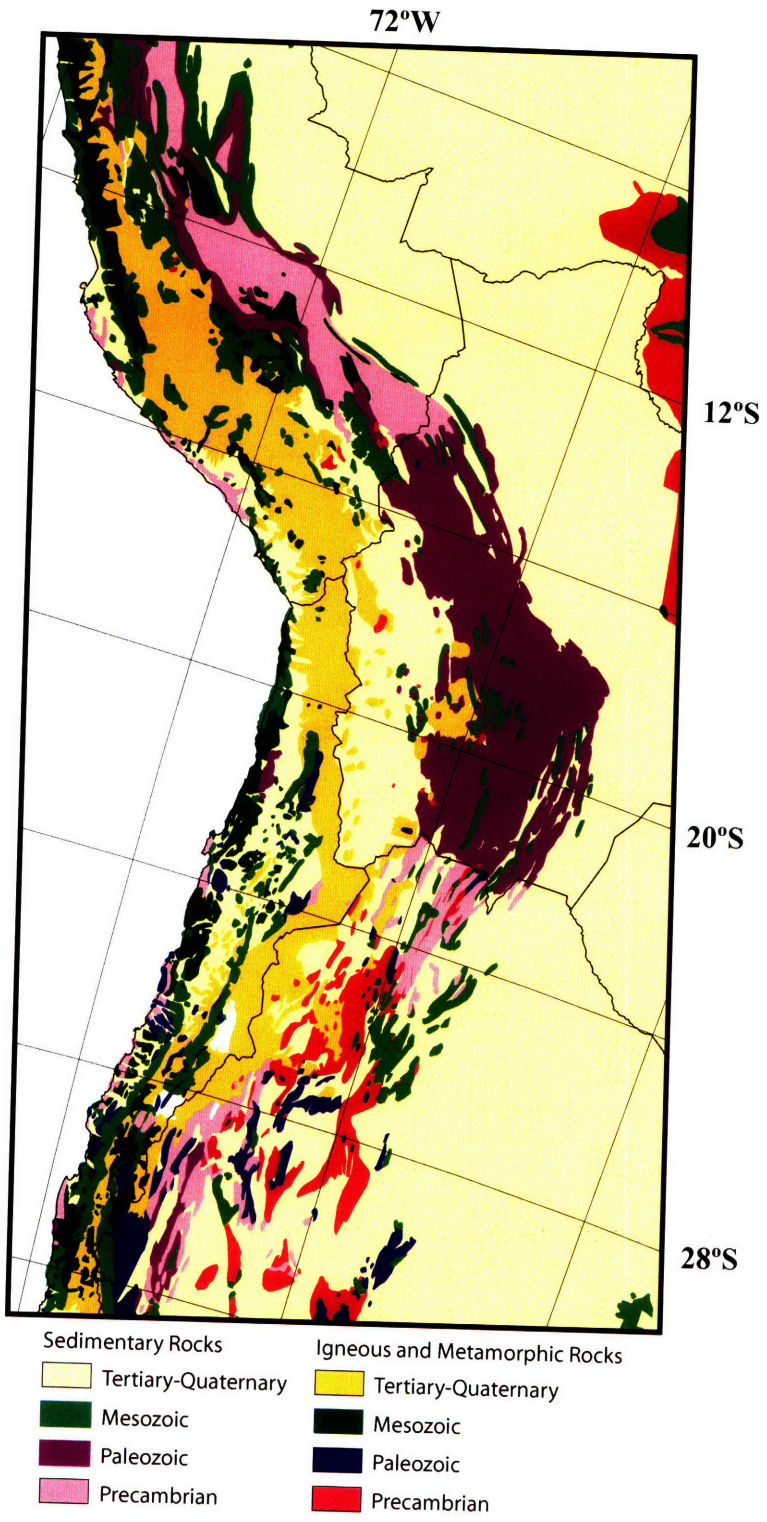
72°W
12°S
20°S
28°S
Sedimentary Rocks
Tertiary-Quaternary
Mesozoic
Paleozoic
Precambrian
Igneous and Metamorphic Rocks
Tertiary-Quaternary
Mesozoic
Paleozoic
Precambrian

Figure 2

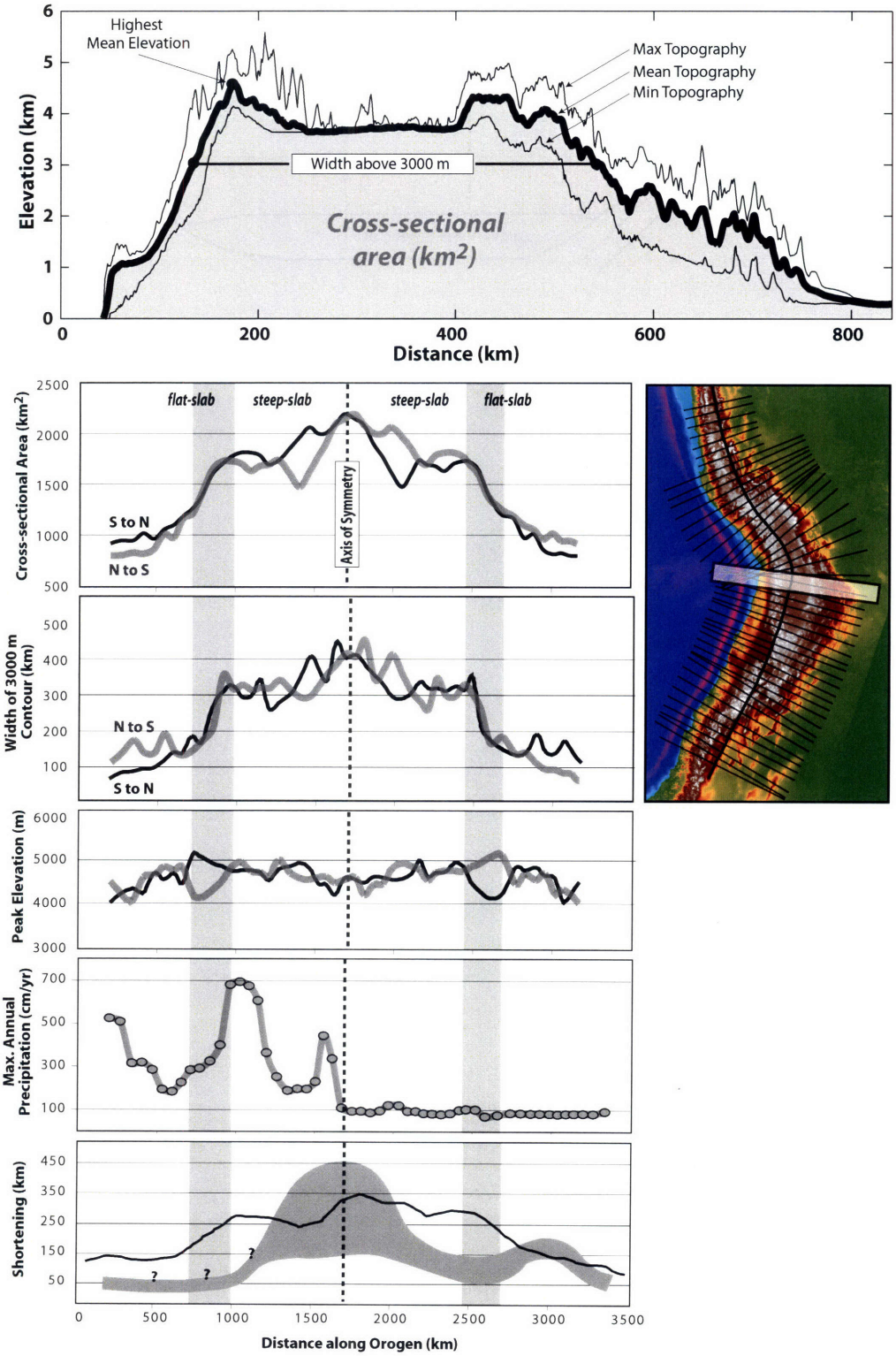
Highest
Mean Elevation
Max Topography
Mean Topography
Min Topography
Width above 3000 m
Cross-sectional
area (km²)
Elevation (km)
Distance (km)
flat-slab
steep-slab
steep-slab
flat-slab
Axis of Symmetry
S to N
N to S
Cross-sectional Area (km²)
Width of 3000 m
Contour (km)
Peak Elevation (m)
Max. Annual
Precipitation (cm/yr)
Shortening (km)
Distance along Orogen (km)

Figure 3

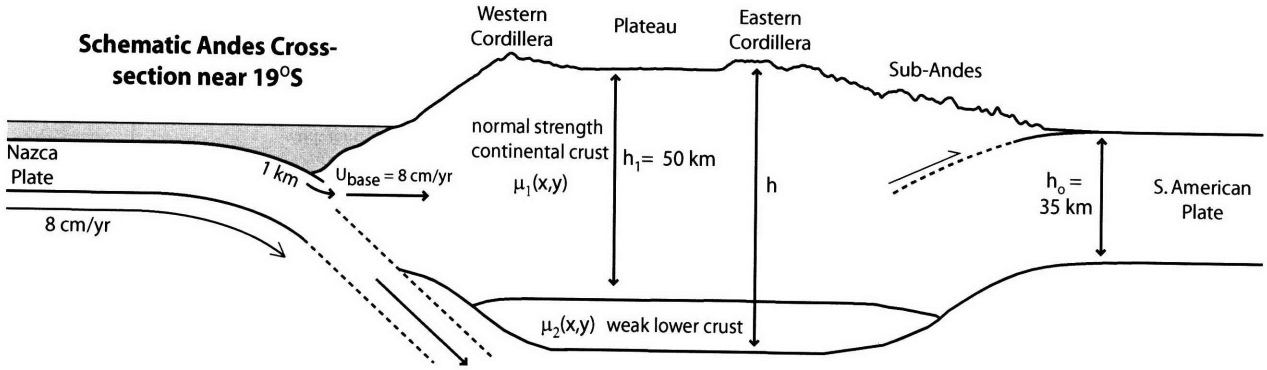
Schematic Andes Cross-section near 19°S
Western Cordillera
Plateau
Eastern Cordillera
Sub-Andes
Nazca Plate
1 km
U_{base} = 8 cm/yr
8 cm/yr
normal strength continental crust
$\mu_1(x,y)$
h_1= 50 km
h
h_o = 35 km
S. American Plate
$\mu_2(x,y)$ weak lower crust

Figure 4

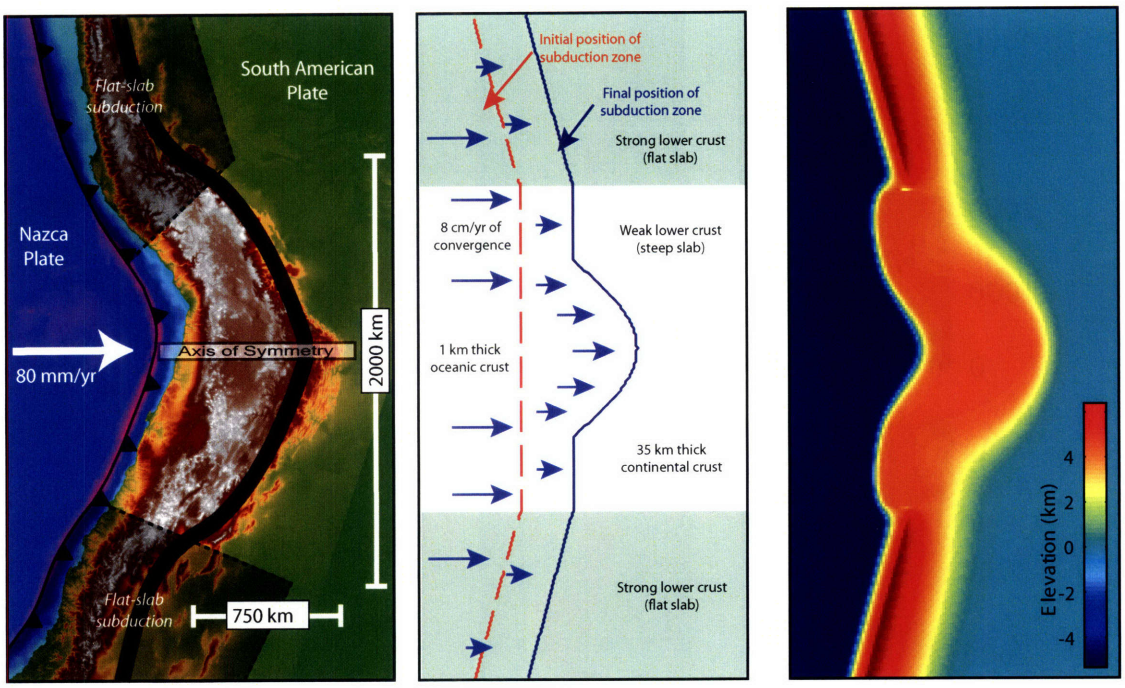
Flat-slab subduction
South American Plate
Nazca Plate
80 mm/yr
Axis of Symmetry
2000 km
Flat-slab subduction
750 km
Initial position of subduction zone
Final position of subduction zone
Strong lower crust (flat slab)
8 cm/yr of convergence
Weak lower crust (steep slab)
1 km thick oceanic crust
35 km thick continental crust
Strong lower crust (flat slab)
Elevation (km)
4
2
0
-2
-4

Figure 5

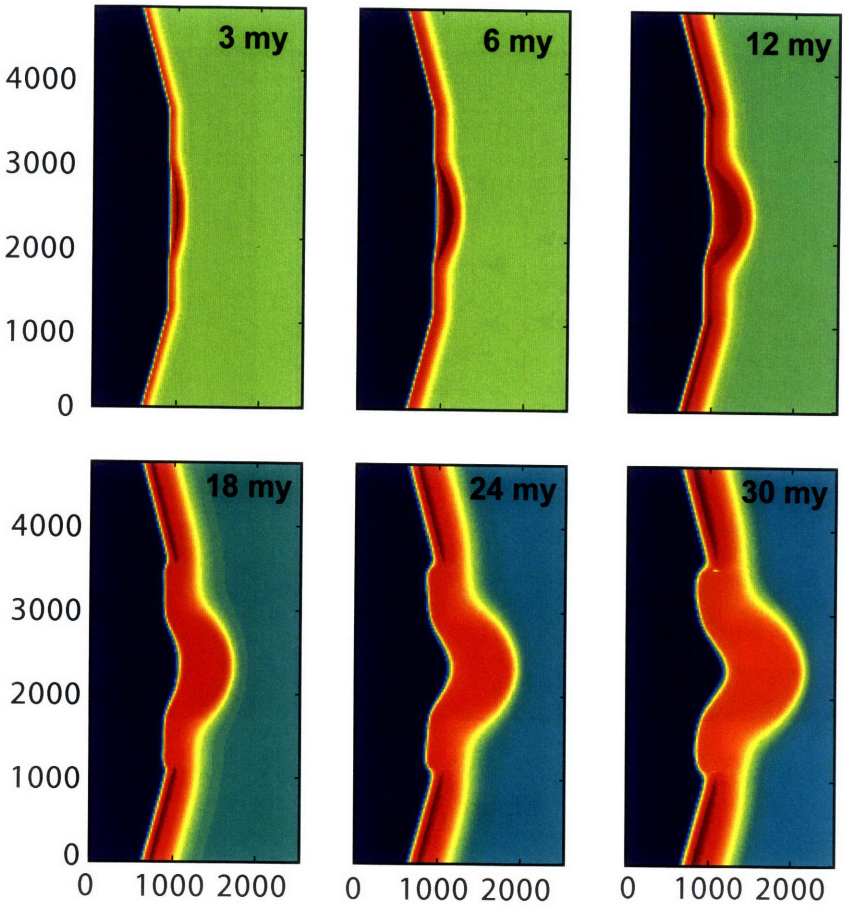

Figure 6

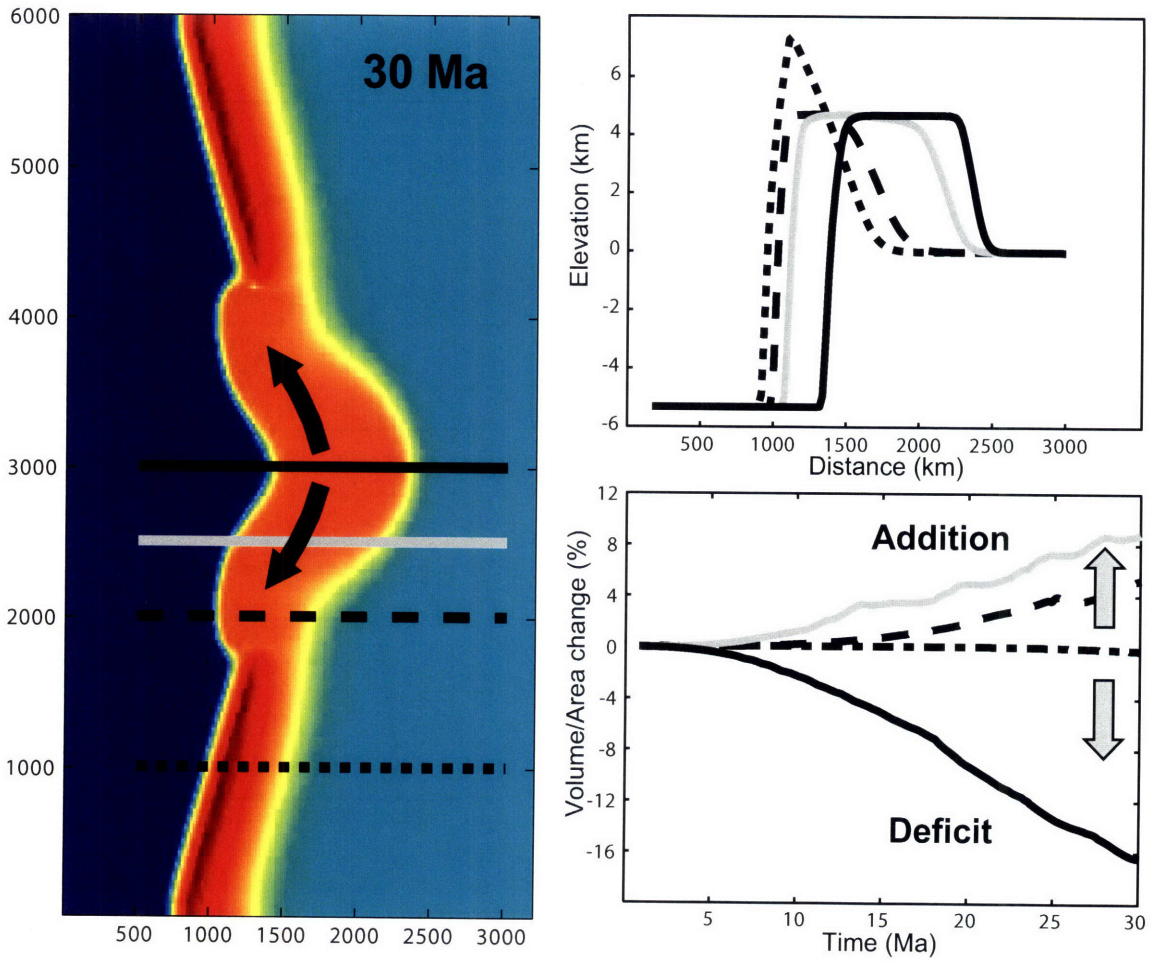
30 Ma
6000
5000
4000
3000
2000
1000
500
1000
1500
2000
2500
3000
Elevation (km)
6
4
2
0
-2
-4
-6
Distance (km)
Addition
Deficit
Volume/Area change (%)
12
8
4
0
-4
-8
-12
-16
5
10
15
20
25
30
Time (Ma)

Figure 7

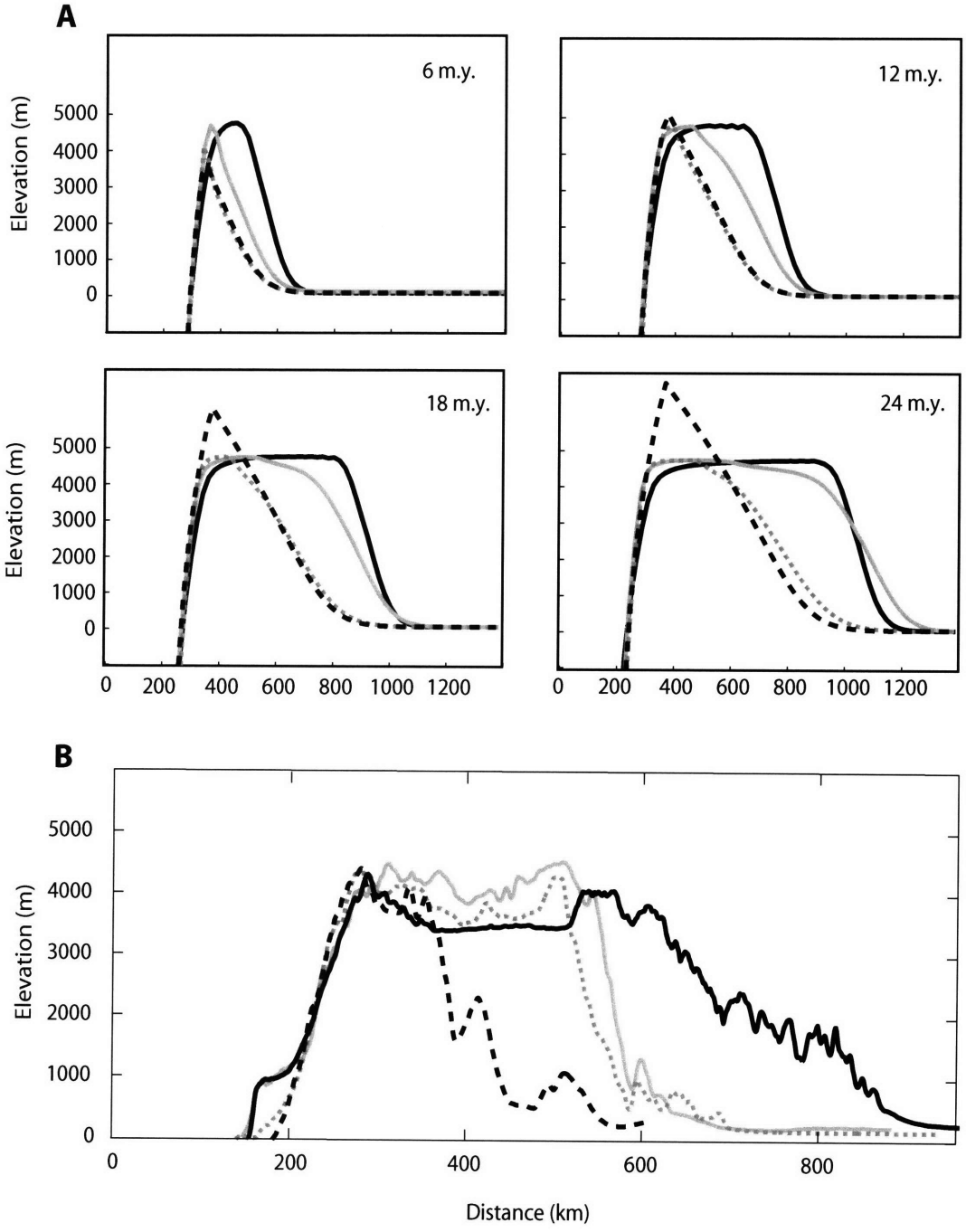
A
6 m.y.
12 m.y.
18 m.y.
24 m.y.
Elevation (m)
5000
4000
3000
2000
1000
0
0
200
400
600
800
1000
1200
B
Elevation (m)
Distance (km)

Figure 8

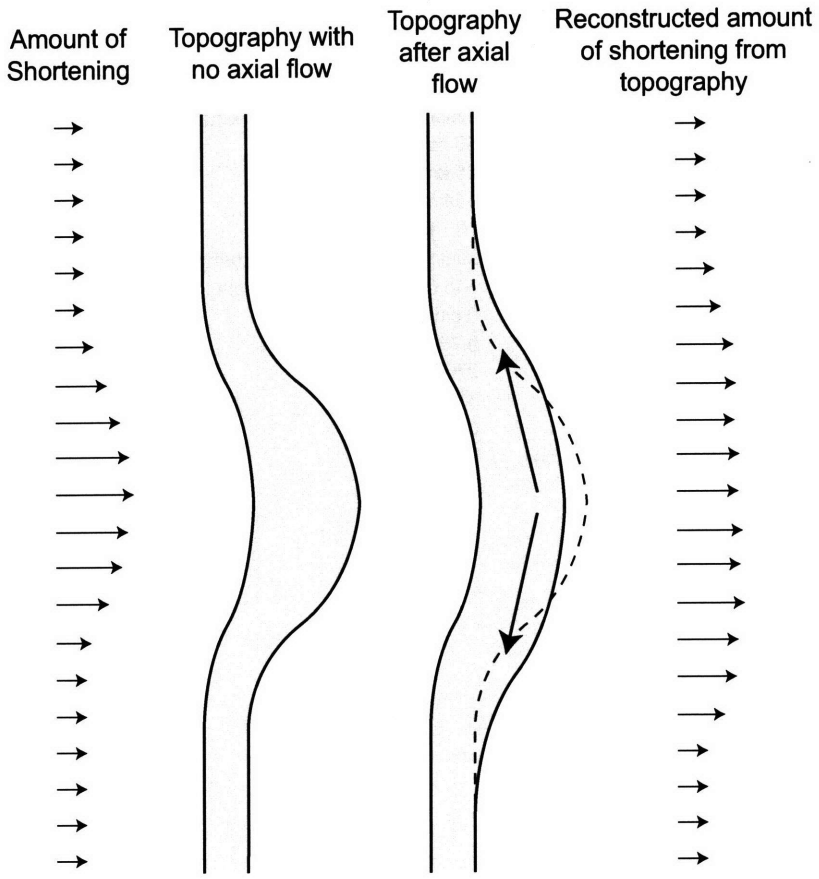
Amount of Shortening
Topography with no axial flow
Topography after axial flow
Reconstructed amount of shortening from topography

Figure 9

Table 1 -- Model Parameters

Definition of variables		value/initial value
h	total thickness of the crust	initial: h_o = 35 km in continental crust, 1km in oceanic crust
h_1	maximum thickness of upper crust	50 km
h_{crit}	critical thickness for viscosity transition	65 km
$h - h_1$	approximate thickness of lower crust	15 km
μ_1	viscosity of upper crust	10^{21} Pa•s
μ_2	viscosity of lower crust	minimum value:10^{17} Pa•s between 14 and 28°S, 10^{21} Pa•s elsewhere
u_{base}	basal velocity in x-direction	5 to 6.5 cm/yr in Nazca Plate, -3 to -1.5 cm/yr in the Brazilian Shield
v_{base}	basal velocity in y-direction	0 cm/yr everywhere
u_{suture}	velocity of suture (in x-direction)	0.75 cm/yr to 3.75 cm/yr
ρ_c	density of the crust	2700 kg/m^3
ρ_m	density of the mantle	3200 kg/m^3
Δt	timestep length	0.01 m.y.
Δx	grid spacing, equal in x and y-directions	20 km

Chapter 4

Cenozoic extension on the eastern margin of the Tibetan Plateau

Kristen L. Cook, B. Clark Burchfiel, Leigh H. Royden

Department of Earth, Atmospheric and Planetary Science, Massachusetts Institute of Technology, Cambridge, MA, USA

Abstract

Models of Tibetan Plateau evolution make different predictions about the distribution of Cenozoic deformation on the eastern margin of the Tibetan Plateau. We describe zones of extensional shear bounding the Gezong Dome and the Kangding Antiform. North to northwestward dipping faults move Paleozoic metasedimentary rocks down and to north relative to the underlying Precambrian granitic and metamorphic rocks. The shear zone bounding the northern Gezong Dome is characterized by a narrow zone of mylonite, while faults bounding the Kangding Antiform contain evidence for a progression from ductile to brittle deformation. Biotite and muscovite $^{40}Ar/^{39}Ar$ data from the mylonite zone indicates that the mylonitic rocks experienced localized heating and cooling at ~30 Ma. Regional thermochronology data suggest that rock uplift in the Danba region and the formation of the Danba Antiform also took place at ~30 Ma. The Danba Antiform parallels, and may be related to, other zones of Cenozoic shortening to the south and west. Oligocene deformation in the Danba region coincides with the initiation of motion along the Ailao Shan and Altyn Tagh Faults and may be associated with the onset of eastward extrusion, indicating that deformation during the Oligocene was more widespread than predicted by the extrusion model.

Introduction

The deformation of the Tibetan Plateau is commonly described in terms of two end-member models. One posits that deformation is distributed throughout the crust in a

continuous manner, while the other suggests that deformation is largely confined to major faults bounding rigid lithospheric blocks. These models make different predictions about the timing and distribution of Cenozoic structures on the eastern margin of the Tibetan Plateau, a region that has a long and complicated deformation history. Several recent studies constrain the timing of surface uplift of the eastern margin to be Middle to Late Miocene (Clark et al., 2005; Ouimet, 2007; Kirby et al., 2002), but the Cenozoic tectonic evolution of this region, particularly during the period after the India-Asia collision at ~50 Ma and the uplift of the region at 8-12 Ma, remains poorly understood.

In this paper we address deformation in the region of the Danba Antiform and use structural and thermochronologic data to link extensional faults bounding the northern and western sides of the Kangding Antiform and the northern boundary of the Gezong Dome to Oligocene uplift of the Danba Antiform. The Danba Antiform appears to be part of a larger NW-SE trending zone of shortening and uplift rock uplift, and may be related to a parallel belt of Cenozoic shortening to the west. We suggest that the eastern margin of Tibet may have experienced widespread deformation during Oligocene time. This deformation coincides with the initiation of eastward extrusion along the Altyn Tagh and Ailao Shan strike-slip faults to the north and south of the Danba region and suggests that deformation was more widely distributed than is suggested by the extrusion model.

Geologic Setting

The Danba region is located ~100 km west of the steep eastern margin of the Tibetan Plateau, (Figure 1) at an average elevation of 3500 to 4500 m. The region is incised by deep river gorges that create several kilometers of local relief. Eastward, the

plateau ends abruptly where the Longmen Shan range, which forms the eastern plateau margin, abuts the Mesozoic Sichuan Basin, which has a surface elevation of ~500 m.

Pre-Cenozoic deformation

The eastern margin of the Tibetan Plateau has experienced intense deformation from late Precambrian time through the present. The Danba region underwent left-lateral transpression during Late Triassic closure of the basin between the North and South China Blocks and the Tibet Block in Late Triassic to Early Jurassic time (Dewey 1988, Burchfiel 1995, Harrowfield and Wilson, 2005) when a sequence of continental margin sediments and flysch were deformed into N to NW trending isoclinal folds and thrust southeastward onto the rocks of the Yangtze craton. The thrust sheets are dominantly composed of Triassic Songpan-Garze flysch, which now covers much of the eastern plateau. Much of the deformation within the flysch occurred at greenschist-grade conditions and structures are intruded by undeformed to weakly deformed granitic plutons of Jurassic age (Wallis et al., 2003; Roger et al., 2004).

The Middle and Late Mesozoic evolution of the eastern margin is poorly constrained, although evidence for continued deformation is provided by the stratigraphy of the Sichuan Basin. Foreland basin subsidence and deposition east of the Longmen Shan began in the Late Triassic as the result of tectonic loading via thrusting in the Longmen Shan thrust belt during the deformation episode described above. Deposition of clastic sediments in the Sichuan Basin continued throughout the Mesozoic, and up to 5 km of Middle Jurassic to Early Cretaceous sediments were deposited in portions of the basin (Meng et al., 2005), suggesting that uplift and shortening in the Longmen Shan also

continued throughout the Mesozoic. However, structures of Middle Jurassic to Cretaceous age have not been identified in the Longmen Shan and Danba regions (Burchfiel et al., 1995).

In several areas near the eastern plateau margin, the crystalline basement beneath the flysch is exposed. The westernmost of these encompasses the Danba Antiform and the Danba Metamorphic Terrane (Figures 1, 2). For clarity, we will use the term Danba Antiform to refer to the entire northwest-southeast corridor of pre-Tertiary rocks, the term Danba Metamorphic Terrane to refer to the high grade region in the northwestern portion of the antiform, and the term Kangding Antiform to refer to the complex of Precambrian rocks in the southeastern part of the Danba Antiform.

The Danba Metamorphic Terrane consists of several granitic gneiss and migmatite cored domes overlain by variably metamorphosed Sinian to Permian cover rocks. Metamorphism in the northern part of the Danba Metamorphic Terrane reaches migmatite grade; the metamorphic grade decreases rapidly to the east, north, and west, and somewhat more gradually to the south. The Gezong Dome is located within the zone of staurolite grade metamorphism (Huang et al., 2003) in the south of the Danba Metamorphic Terrane and is often considered to be part of the terrane.

The earliest recorded metamorphism in the Danba region is Late Triassic, when Barrovian metamorphism occurred during the Indosinian orogeny (approx 204-190 Ma; Huang et al., 2003b), synchronous with the emplacement of granitic plutons (Huang et al, 2003b; Roger et al., 2004). Extensive folding in the overlying Songpan-Ganze flysch along EW-trending fold axes was accompanied by development of gently-dipping shear zones that separate Triassic sediments from the underlying basement and display north-

south trending lineations with a top-to-the-south sense of shear (Huang et al., 2003; Harrowfield and Wilson, 2005). A proposed later phase of deformation and metamorphism in the northern Danba Metamorphic Terrane at ~165 Ma involves sillimanite grade metamorphism, migmatization, and folding along N-S trending axes (Huang et al, 2003b). The high grade rocks are exposed in domal structures that are often interpreted as resulting from interference of orthogonal folds (Burchfiel et al., 1995, Huang et al, 2003), although Harrowfield et al. (2005) have suggested that the domes are related to diapiric upwelling of partial melt around 200 Ma. In our opinion, this cannot be correct for the Gezong Dome which is cored by undeformed and unmetamorphosed granite with a U-Pb age of 864+/-8 Ma (Zhou et al, 2002).

The Gezong Dome and the Danba Metamorphic Terrane are the northwestward continuation of the Kangding Antiform. To the south, the Kangding Antiform exposes Precambrian granitic and metamorphic rocks, dated at 796 +/- 14 Ma (Zhou et al., 2002), that are overlain by Proterozoic and Paleozoic metasediments. The antiform is truncated to the southwest by the Late Cenozoic, left-lateral Xianshuihe fault, and to the southeast by the right-lateral Leng Qi Fault zone. In several places along the northern and western margin of the antiform, the contact between the crystalline rocks and the overlying metasedimentary units is a normal fault, as is discussed in detail below. The Kangding Antiform appears to coincide with the northern end of the Kungdian high, a region of elevated topography through at least some of the Paleozoic and early Triassic. Upper Triassic rocks in depositional contact with Precambrian crystalline rocks can be seen in the region where the Dadu River Fault cuts the Kangding Antiform.

Cenozoic deformation

The Early to Middle Cenozoic evolution of the eastern margin of the Tibetan plateau is poorly constrained. Some authors suggest that an episode of Barrovian-type metamorphism occurred north of Danba at ~65 Ma (Wallis et al., 2003, also Hou et al 1996, Xu et al., 1992 see Huang 2003 p. 225). In the southern part of the Longmen Shan thrust belt, sediments presumed to be Oligocene in age are complexly folded and faulted. This points to Cenozoic reactivation of thrust faults in the Longmen Shan thrust belt. However, the paucity of Cenozoic rocks in this area means that the timing and spatial extent of Cenozoic reworking are poorly constrained, particularly within the Songpan-Garze terrane.

Deformation from Middle Miocene through the present time is somewhat better constrained. Low temperature thermochronology indicates that rapid uplift of the plateau region east of the Yangtze River began at ~9-13 Ma (Clark et al., 2005; Ouimet, 2007). Uplift of the steep topographic front of the Longmen Shan also appears to have begun at ~5-12 Ma, at a time with only minor upper crustal shortening (Kirby et al., 2002; Burchfiel et al., 1995). Pliocene-Quaternary deformation in eastern Tibet is dominated by left-lateral strike-slip faults that commonly displace the topographic gradient of the margin as well as the older structures (Burchfiel et al., 1995; Wang and Burchfiel, 1998). The active left-lateral Xianshuihe fault has accumulated ~60 km of displacement since at least 12 Ma (Wang et al., 1998; Roger et al., 1995). Cenozoic plutonism in the region appears confined to the northern end of the Gongga Shan Massif, where a two-mica granite was emplaced at ~12 – 16 Ma (Roger et al., 1995). Active faulting in the Longmen Shan region is largely confined to margin parallel faults with right-lateral and a

small component of thrust motion. These faults commonly parallel and may reactivate Mesozoic thrust faults.

Normal faulting of possible Cenozoic age has been recognized in the Longmen Shan region, occurring along structures west of the Pengguan and Baoxing Massifs, around the Kangding antiform, and on northern boundary of the Gezong dome (Burchfiel et al., 1995). This paper discusses in detail the extensional faults associated with the Danba Antiform and Gezong Dome.

Gezong Dome

The Gezong dome is cored by undeformed Precambrian granites and granitic gneisses and bounded on all sides by zones of ductile shear that dip away from the center of the dome (Figure 3). The interior of the dome is cut by numerous sub-vertical mafic dikes. The dikes and the surrounding granitic rocks are undeformed, except at the margins of the dome, and the granite in the core of the dome gives an average U-Pb age of 864+/-8 Ma (Zhou et al, 2002). The dikes may be related to the Permian Emei Shan flood basalts (Song et al., 2004) but their emplacement has not been dated. The only ages available are Cretaceous $^{40}Ar/^{39}Ar$ ages, which most likely reflect later cooling and not the timing of intrusion (see below).

On the northern boundary of the dome, a well exposed, accessible succession consists of undeformed granite grading northward into fractured and sheared granitic rocks, and then into ~100m of mylonites, including a mylonitized dike, and finally into the overlying succession of Paleozoic schist. North of the boundary, within the metasedimentary rocks, small, brittle fractures and shear zones dip northward. Fabric in

the metasedimentary rocks indicates a top-to-the-south (thrust) sense of shear, probably related to the ~200 Ma metamorphism and deformation. In the mylonitic rocks, S-C fabrics indicate a top to the NW (normal) sense of shear. Foliation surfaces in the mylonite zone strike 205° and dip 51° west, and generally parallel the foliation of the overlying schists, which strike 210° and dip 35°-46° west. Lineations in the mylonite generally plunge 57° towards 338°. We interpret the mylonite, as well as the isolated zones of top to the NW shear within the schists, as a post ~200 Ma episode of normal faulting along the northern margin of the dome.

The southern boundary of the dome boundary is less well-exposed. Alluvium, buildings, and fields obscure much of the transition from undeformed granite to overlying metasediments. There is a zone of highly sheared rocks, but it is unclear whether they originated as granitic or sedimentary rocks, and the transition from the granitic core of the dome to the mylonite is not exposed. Foliation planes in the mylonite and the overlying schist dip ~60° to the southeast, and the mylonitic lineation plunges 10° towards 170°.

Kangding Antiform

Northwestern boundary

At the nose of the Kangding antiform, the Precambrian crystalline rocks that core the antiform are separated from Sinian sedimentary rocks by a thick zone of faulted rocks, fault gouge, and tectonic breccia (Figure 4). Small shear zones in the Precambrian rocks and folds in the gouge indicate a normal sense of motion with a shallow northwestward dip (~30 degrees) (Figure 5). Basement rocks in the fault zone contain

~100 m of sheared and mylonitic rocks with stretching lineations generally plunging gently to the north (~14-30 degrees). The mylonite is lower greenschist grade, and is dominated by chlorite. Above the mylonitic rocks is a zone of brittlely faulted rocks, overlain by a succession of presumably-Sinian sedimentary rocks, including a blue carbonate breccia, several different massive carbonates, a megabreccia containing a large variety of lithologies, a conglomerate with poorly-sorted, rounded clasts of widely varying lithology and no known local source, and a massive, blue, cliff-forming dolomite. Carbonate at the base of the Sinian section is also highly sheared (both ductile and brittle shear). Chinese maps show the Sinian rocks overlain by Ordovician quartzite, a thick sequence of Silurian and Devonian schist and quartzite (Ministry of Geology and Mineral Resources, 1991).

The hillside where the normal fault between the crystalline rocks and the Sinian sedimentary rocks is exposed also contains what appears to be a landslide deposit, with large un-cemented blocks and mega-breccia. The landslide deposit obscures much of the fault zone and, coupled with the poor exposure, makes it difficult to determine what material is in place.

On the northwestern side of the antiform, the Precambrian rocks are separated from Silurian and Devonian schists and carbonates by a N-S striking vertical fault zone. Lineations are horizontal to gently N-plunging and trend approximate NNW-SSE, with a right-lateral sense of motion. The fault zone contains gouge, tectonic breccia, and a zone of tight isoclinal folds in the sedimentary rocks; the fold axes parallel the lineation, and plunge 10° -24° to the north. West of the fault zone, granitic rocks appear in several small pods within the schist. The relationship between these pods and the main granite body is

unclear although mineralization in the schist surrounding one of the pods suggests that the granite pods are a more recent (post-Devonian) intrusion. Silurian rocks occur in small slivers along the fault zone; elsewhere the fault juxtaposes Precambrian rocks against the Devonian.

Our observations from both of these localities indicate that the metasedimentary cover rocks have moved northward relative to the rocks of the underlying Kangding Granitic Complex.

Kangding region

Within the city of Kangding, steeply westward-dipping mylonitic to brittle shear zones place Triassic clastic sedimentary rocks over the crystalline rocks of the Kangding complex (Figure 6). The shear zones and mylonitic foliation planes trend generally N to NNE, and dip 60° to 75° to the west. The mylonite contains an S-C fabric indicating west-side down displacement, with stretching lineations trending ~280° to 330° and plunging 40° to 70°. The overlying Triassic quartzites and shales strike more to the NE and have a somewhat shallower 44° to 57° westward dip. The Triassic rocks are overlain to the west by Sinian dolomite, juxtaposed across what is probably a thrust fault (Figure 6) (Burchfiel et al., 1995). To the north of Kangding, the Triassic rocks disappear and Sinian carbonate is juxtaposed against the Precambrian crystalline rocks. This contact is probably a continuation of the normal fault exposed in Kangding, but road and building construction made the contact inaccessible. South of the town of Kangding, the Precambrian rocks of the Kangding antiform are truncated by the active left-lateral strike-slip Xianshuihe Fault.

Jintang region

The northern side of the Kangding Antiform is relatively inaccessible and poorly exposed. The only accessible portion of the boundary is near the town of Jintang, where it has been altered by several younger faults, including the active right-lateral Dadu River Fault (Burchfiel et al., 1995). The Dadu River Fault is clearly visible in the morphology of the landscape and as exposed shear zones. To the west of the Dadu River Fault, Precambrian rocks of the Kangding complex are overlain by a succession of Paleozoic sedimentary rocks. The contact between the Precambrian rocks and the overlying sedimentary rocks is not exposed, but outcrops of highly sheared Sinian carbonate have a foliation parallel to the mapped contact (strike 311°-322° and dip 48°-78° NE), consistent with faulting along the contact.

The normal faults described above appear to be Cenozoic features, but their timing has not previously been constrained. We use $^{40}Ar/^{39}Ar$ thermochronology to investigate the cooling history of the Gezong Dome and address the timing of activity along the normal faults described above, and present a collection of new $^{40}Ar/^{39}Ar$ biotite and muscovite ages from the Gezong Dome and Kangding region.

$^{40}Ar/^{39}Ar$ Thermochronology

Samples for $^{40}Ar/^{39}Ar$ analysis were collected from the margins of and within the Gezong Dome (Figure 3), including a suite of samples across the high-angle shear zone bounding the northern end of the granitic dome. The latter were collected at approximately the same elevation (2530 m) and include one sample from relatively

undeformed granite, two from the mylonite zone (one from mylonitized granite, one from the mylonitized dike), and five from the schists in a transect ~1 km in length. We also collected four samples across the southern boundary of the dome, one from the western boundary, and one from the center of the dome. A single sample was collected from the mylonite bounding the western side of the Kangding Antiform in Kangding, in the only locality around the Kangding Antiform with rocks suitable for $^{40}Ar/^{39}Ar$ dating on muscovite or biotite.

When possible, we analyzed biotite and muscovite in each sample. The multiple episodes of metamorphism and deformation that these samples have experienced raises the possibility of multiple populations of grains of different age within a single sample. Therefore we conducted 8-10 total fusion $^{40}Ar/^{39}Ar$ analyses for each sample.

Samples were crushed, sieved, and washed. Following standard mineral separation techniques, the samples were handpicked under a binocular microscope for biotite and muscovite. Grains were loaded into aluminum capsules and irradiated at the McMaster University Research Reactor in Hamilton, Ontario, with Taylor Creek sanidine as the neutron flux monitor. The samples were analyzed at the $^{40}Ar/^{39}Ar$ laboratory at MIT. For each biotite sample, we analyzed 8-10 single grains by laser total fusion. For each muscovite sample, we analyzed 8-10 aliquots of 1-3 grains each to ensure the release of enough gas for smaller grains.

Each single grain or multi-grain aliquot was loaded into a 2mm well in 100-well copper planchets, which were then placed under vacuum and baked out for 8 hours at 320-350 °C. The grains underwent total fusion using an 810 nm Ar-ion laser beam with up to 15 W power for 30 s. The released gas was gettered for 10 minutes with SAES

St101 and St172 getters, then analyzed on a MAP 215-50 mass spec with an electron multiplier detector. Data reduction, blank and fractionation corrections, and age calculations were performed using ArArCalc version 2.40 (Kopper 2002). J values were calculated using the 28.34 Ma Taylor Creek sanidine (Renne et al, 1998) flux monitor.

$^{40}Ar/^{39}Ar$ Results

The weighted mean age and the range of ages for each individual analysis, yielding 27 new $^{40}Ar/^{39}Ar$ ages, are given in Table 1. Agreement between individual grains within each sample is good, although older samples tend to have a higher spread in ages.

Gezong Dome

Biotite $^{40}Ar/^{39}Ar$ data

The relatively small area of the Gezong Dome displays a wide range of ages (Figure 7, 8). The biotite data cluster between 26 and 39 Ma at the northern boundary of the dome's granitic core with the youngest ages from a sample of the mylonitized granitic rocks (28.5 ± 0.59 Ma on sample kc05-20) and from the mylonitized dike (25.9 ± 0.77 Ma on sample kc0519). Young ages were also obtained from small zones of top to the NW shear within metasedimentary schists (30.7 ± 4.3 Ma on sample kc05-23 and 38 ± 3.1 Ma on sample kc07-60). Sample kc05-18, from relatively undeformed granite near the northern boundary, gives an intermediate age of 46.6 ± 2.4 Ma. Older ages were obtained from the metasedimentary schists overlying the mylonitic shear zone (from 57.9

to 193 Ma), from an undeformed dike in the center of the dome (130.8 ± 4.26) and from the southern margin of the dome (78 to 146 Ma).

Muscovite $^{40}Ar/^{39}Ar$ data

Sample kc0519 from the mylonitized dike along the northern boundary of the dome also displayed a young muscovite age of 36 ± 1.8 Ma, while muscovite grains suitable for dating were not present in the mylonitized granite sample. Older muscovite ages were obtained from the undeformed granite just south of the mylonite zone (57 ± 4.5 Ma on sample kc05-18) and from the five schist samples, which cluster between 74 and 93 Ma. In three of these schist samples, the biotite ages are older than the muscovite ages. Older ages were also obtained from samples from the southern margin of the dome (63 to 116 Ma). In two of these samples, the biotite ages are older than the muscovite ages.

Kangding

The single sample of mylonite from the western boundary of the Kangding Antiform gives an average muscovite $^{40}Ar/^{39}Ar$ age of 27.8 ± 1.44 Ma; individual aliquots ranged from 25.3 to 30.1 Ma. This sample did not contain biotite.

Other Studies

The $^{40}Ar/^{39}Ar$ ages measured from samples above and below the zone of normal shear are similar to the few previously measured ages within the Gezong dome. Wallis et al (2003) report four biotite $^{40}Ar/^{39}Ar$ ages ranging from 47 to 94 Ma and three muscovite

$^{40}Ar/^{39}Ar$ ages between 71 and 102 Ma from the interior of the dome (Figure 8). There are no previously reported ages from the mylonitic zones surrounding the dome, where we obtained $^{40}Ar/^{39}Ar$ ages younger than 40 Ma.

Interpretation

The $^{40}Ar/^{39}Ar$ ages measured in this study can be divided into those older than 40 Ma, and those younger than 40 Ma. Samples from the Gezong dome and the overlying schist fall into the first category; here the wide range of $^{40}Ar/^{39}Ar$ ages and the variations of age within individual samples argue for relatively slow cooling within the partial retention zone prior to 40 Ma (~300-340°C for biotite and ~350 °C for muscovite (Hames and Bowring, 1994; Hodges, 2003; Grove and Harrison, 1996)). The wide variation in ages thus results from differences in grain size and composition, among other factors, rather than from first-order differences in thermal history.

The $^{40}Ar/^{39}Ar$ ages from the northern boundary of Gezong dome indicate an episode of localized heating and cooling along this boundary at around 30 Ma, while rocks immediately above and below remained below the closure temperature of Ar in biotite and muscovite. The samples with Oligocene ages were collected from mylonite containing top to the north (normal sense) shear sense indicators and from narrow zones of normal shear embedded in the schist. Adjacent samples gave older ages and were collected from schist that contained predominantly top to the S shear sense indicators, likely due to the ~200 Ma episode of deformation and metamorphism. The rapid changes in age over a short distance across the margin of the dome, and the correlation between fabric and $^{40}Ar/^{39}Ar$ age (Figure 7) suggests that the Oligocene ages are related to

localized heating and cooling in the zones of extensional shear, and are not recording regional uplift and cooling. The sample from the Kangding Antiform suggests Oligocene deformation along the extensional shear zone in Kangding. The muscovite in this sample is very fine-grained, and the 27.8 Ma $^{40}Ar/^{39}Ar$ age may reflect recrystallization or grain size reduction during deformation. We propose that motion along these normal faults took place at ~30 Ma, although we cannot rule out the possibility that normal faulting took place earlier and the 30 Ma ages reflect later fluid flow within the fault zone.

The lack of Oligocene $^{40}Ar/^{39}Ar$ ages on the southern margin of the Gezong dome has several possible explanations: 1) A Cenozoic shear zone exists, but our sampling did not capture it. The zone of young ages in the north was quite narrow; a similar zone could be easily missed due to the poor and discontinuous exposure across the southern margin. 2) We sampled a zone of Cenozoic shear, but the biotite from our sample is contaminated with excess Ar, and therefore gives an anomalously old age. This possibility is hinted at by sample kc05-26, which gives an old biotite age, but a muscovite age 40-50 Ma younger than the surrounding rocks, perhaps reflecting partial heating and Ar loss. 3) A Cenozoic shear zone exists, but did not reset the biotite or muscovite. 4) There was no Cenozoic shear on the southern margin, and the shear zone from the northern margin instead continues up into the metasedimentary rocks above the dome's granitic core.

Danba Antiform

The zones of normal shear bounding both the northern Gezong dome and Kangding antiform do not continue into the metasediments to the east and west, and instead appear to fold around the antiformal and domal structures. Although we did not

sample Oligocene mylonite on the northwestern side of the Gezong dome, the similarity of fractures and fabric suggests that the shear zone continues around the western side of the dome. Similarly, the zones of shear we see around the margins of the Kangding Antiform show a consistent sense of motion between the Precambrian crystalline rocks and the Paleozoic metasedimentary rocks, and appear to represent the same episode of deformation. The folding of this structure indicates that the formation of the Danba Antiform and the uplift of the region relative to the surrounding Triassic flysch postdates, or is synchronous with shear along the dome and antiform boundaries.

The relative timing of extension and rock uplift is further constrained by thermochronology data to the north of the Gezong Dome, from the Danba Domal Metamorphic Terrane (Figure 8), which suggest an episode of regional uplift around the same time as the extensional faulting. Huang et al (2003) measure Biotite Rb-Sr in samples throughout the region and find a cluster of ages around 30 Ma. The ~30 Ma cooling ages are both within the domes and in the surrounding metasediments, confirming that the formation of the northern DDMT migmatite-cored domes took place prior to 30 Ma. Wallis et al. (2003) measure three biotite $^{40}Ar/^{39}Ar$ between 52 and 71 Ma in the same region (Figure 8). The presence of older biotite ages among the 30 Ma Rb-Sr ages suggests that prior to ~30 Ma the region was at a temperature around 300°C – near the closure temperature for biotite Rb-Sr, but below the closure temperature for biotite $^{40}Ar/^{39}Ar$. Huang et al (2003) attribute the Oligocene Rb-Sr ages to regional cooling and uplift, indicating that extension along the boundary of the Gezong Dome and Kangding Antiform was accompanied by regional uplift in at least the northern part of the Danba Antiform.

We see further evidence for uplift synchronous with faulting in the fault bounding the Kangding Antiform, which has both a brittle and a ductile component. All of the locations around the antiform contain both mylonite and fault gouge and breccia, and the brittle and ductile zones have the same orientation and sense of motion. This suggests that as the faulting continued, slip along the fault bounding the Kangding Antiform moved from the ductile to the brittle regime as the region cooled during uplift of the antiform. Because our $^{40}Ar/^{39}Ar$ data only address cooling through ~300 – 350°C, it does not place constraints on the timing of the later stage of shallower brittle faulting around the Kangding Antiform.

The structural and thermochronology data presented above suggest that the formation of the NW-SE trending Danba Antiform coincided with top to the NW motion along a series of extensional faults (Figure 9). The relationship between extension and antiform uplift remains somewhat enigmatic. One possibility is that is that extension is relatively local and small in magnitude. The Danba region contains several NW-SE trending faults that offset metamorphic isograds with a thrust and left-lateral sense of motion (Figure 2) (Huang et al., 2003). Although the ages of these faults are unknown, the Gezong Dome is located between several faults, and extension along the dome boundary is consistent with a right stepover between two left-lateral fault strands. Similarly, extension along the Kangding Antiform may be related to a stepover or releasing bend in one of these left-lateral faults.

Alternatively, the normal faults in the Danba Antiform may be related to more regional-scale processes, as extensional deformation of approximately Oligocene age has

been documented in several other areas of the eastern plateau margin, suggesting that it may be a common characteristic of the regional tectonics at that time. To the southwest of Kangding, the Jianglang Dome (Figure 1) shows evidence for several episodes of extensional deformation, the latest of which appears to be related to the India-Asia collision (Yan et al., 2003), although the timing of extension has not been dated. To the northeast of Danba, near Wenchuan City, the Xuelongbao Dome is bounded on the east by a steeply dipping zone of normal-sense shear. Mylonite within this shear zone has been dated with $^{40}Ar/^{39}Ar$ to ~25-30 Ma (Hames and Burchfiel, 1993).

The $^{40}Ar/^{39}Ar$ data from the Danba area show that the Gezong Dome experienced limited unroofing in the Cenozoic, as ages within the dome reflect slow cooling during the Mesozoic and are similar to ages in the hanging wall farther north. This suggests that the first possibility is more likely and that the magnitude of Cenozoic extension along the northern boundary of the Gezong Dome was relatively small. However, we cannot rule out the possibility that the distribution of cooling ages was also affected by differential motion during Miocene surface uplift of the Danba region (Clark et al., 2005; Ouimet, 2007).

Discussion

The uplift of the Danba Antiform may be part of a broader zone of Middle Cenozoic NE-SW compression. The band of rock uplift associated with the Danba Antiform continues to the southeast into the sedimentary rocks of the Mesozoic foredeep. Proterozoic and early Paleozoic sedimentary and metamorphic rocks are brought up in three NW trending fold and thrust belts (Chengdu Inst. Geol. Min. Res., 2004; Burchfiel

et al., 1995). Cross-cutting relationships suggest that the fold and thrust belts and the Danba Antiform formed during the same period in the Cenozoic, prior to or contemporaneous with motion along the Leng Qi Fault zone (Burchfiel et al., 1995).

To the west a series of NW-SE thrust faults cut rocks as young as Eocene along the Garze-Litang suture, at the eastern boundary of the Yidun Arc, indicating that this boundary was reactivated in the Cenozoic (Clark Burchfiel, personal communication; Chengdu Inst. Geol. Min. Res., 2004). These structures approximately parallel the trend of the Danba Antiform, and although their timing is poorly constrained, we suggest that shortening along these faults may be related to uplift of the Danba Antiform. The two regions are separated by several hundred kilometers of Triassic flysch in which no parallel Cenozoic structures are mapped; however, the extensive deformation and relatively homogenous stratigraphy of the flysch and the lack of younger rocks would make such structures difficult to identify. It is possible that Oligocene deformation was continuous across the region; alternatively, deformation may have been localized by preexisting structures such as the Garze-Litang suture, the Kungdian high, and the Danba Metamorphic Terrane.

The deformation in the Danba region described above coincides with the initiation of motion along several major Cenozoic strike-slip shear zones related to the collision of India and Eurasia. To the south, in Yunnan Province, the onset of slip along the Ailao Shan Shear Zone has been constrained to ~30 Ma (Chung et al., 1997; Leloup et al., 2001). To the north, left-lateral motion along the Altyn Tagh Fault began in the Late Oligocene (Ritts et al., 2004). These faults accommodated the eastward extrusion of

material from the collision zone, and their initiation represents a major change in the tectonics of the Tibetan Plateau.

The similarity in timing between motion along the Ailao Shan and Altyn Tagh Faults, shear along the normal faults described above, and uplift of the Danba Antiform suggests that the deformation that we see in the Danba region can be tied to the onset of eastward extrusion. In the extrusion model of plateau deformation (Tapponnier et al., 1982), deformation following the India-Asia collision was localized along these major shear zones, which accommodated the eastward extrusion of rigid lithospheric blocks. Oligocene deformation on the eastern margin, hundreds of kilometers from the Ailao Shan Shear Zone, indicates that deformation was more widely distributed than predicted by the extrusion model.

Conclusions

We describe extensional faulting along the northern boundary of the Gezong Dome, and the north and west boundaries of the Kangding Antiform. The faults separate Precambrian granitic and metamorphic rocks from variable metamorphosed Paleozoic sedimentary rocks. Faults range from predominantly ductile at the Gezong Dome, to a mix of brittle and ductile around the Kangding Antiform. In all localities, the sense of motion is top (Paleozoic rocks) to the NW.

$^{40}Ar/^{39}Ar$ data of biotite and muscovite from throughout the Gezong Dome, and from mylonite at Kangding, suggest that these faults experienced ductile shear around 25-30 Ma. Data from within the dome and from the metasedimentary rocks to the north and south indicate that the region cooled slowly through the biotite and muscovite closure

temperatures between ~70 and 120 Ma. Extensional faulting was associated with the uplift and formation of the Danba Antiform.

The Danba Antiform appears to be related to parallel shortening structures to the south and west, suggesting a broad area of Oligocene deformation. The presence of Oligocene deformation in this region of the eastern plateau margin indicates that between the collision of India and Eurasia and the uplift of the eastern margin, deformation was not confined to large strike-slip shear zones, and that the regions in between these shear zones were not behaving as rigid blocks.

References

Burchfiel, B.C., Chen, Z., Liu, Y., and Royden, L.H., 1995, Tectonics of the Longmen Shan and adjacent regions, *International Geological Review* 37(8), 661–736.

Chengdu Institute of Geology and Mineral Resources, China Geological Survey, 2004, Geologic Map of the Qinghai-Xizang (Tibet) Plateau and Adjacent Areas, 1:1,500,000 scale, Chengdu Cartographic Publishing House.

Chung, S.-L., Lee, T.-Y., Lo, C.-H., Wang, P.-L., Chen, C.-Y., Yem, N.T., Hoa, T.T. and Wu, G.-Y., 1997, Intraplate extension prior to continental extrusion along the Alao Shan-Red River shear zone. *Geology* 25, 311–314.

Clark, M.K. and Royden, L.H., 2000, Topographic Ooze: Building the Eastern Margin of Tibet by Lower Crustal Flow, *Geology* 28, 703-706.

Clark, M.K., House, M.A., Royden, L.H., Burchfiel, B.C., Whipple, K.X., Zhang, X., and Tang, W., 2005, Late Cenozoic uplift of southeastern Tibet, *Geology* 33, 525-528.

Clark M.K., Bush J.W.M., and Royden L.H., 2005b, Dynamic topography produced by lower crustal flow against rheological strength heterogeneities bordering the Tibetan Plateau: *Geophysical Journal International* 162, 575–590.

Grove, M. and Harrison, T.M., 1996, $40Ar^{*}$ diffusion in Fe-rich biotite. *American Mineralogist* 81, 940–951.

Hames, W.E., and Burchfiel, B.C., 1993, Laser $^{40}Ar/^{39}Ar$ dating of Cenozoic, greenschist-facies shear zones, Longmen Shan, China, *GSA Abstr. with Program*, 25 (6), A-118.

Hames, W.E. and Bowring, S.A., 1994, An empirical evaluation of the argon diffusion geometry in muscovite, *Earth and Planetary Science Letters* 124, 161-167.

Harrowfield, M. J., and Wilson, C. J. L. 2005. Indosinian deformation of the Songpan Garze Fold Belt, northeast Tibetan Plateau. *J. Struct. Geol.* 27, 101-117.

Hodges, K.V., 2003, Geochronology and Thermochronology in Orogenic Systems, *in* Rudnick, R. L., ed., *The Crust: Treatise on Geochemistry*, Amsterdam, Elsevier Science, 263-292.

Huang M., Maas R., Buick I. S., and Williams I. S., 2003, Crustal response to continental collisions between the Tibet, Indian, South China and North China Blocks:

geochronological constraints from the Songpan-Garze Orogenic Belt, western China, *J. Metamorphic Geol.* 21, 223–240.

Huang, M., Buick, I.S., and Hou, W., 2003b. Tectonometamorphic evolution of the eastern Tibet plateau: evidence from the central Songpan-Garze orogenic belt, western China, *Journal of Petrology* 44, 255–278.

Kirby, E., Reiners, P.W., Krol, M.A., Whipple, K.X., Hodges, K.V., Farley, K.A., Tang, W., and Chen, Z., 2002, Late Cenozoic evolution of the eastern margin of the Tibetan Plateau: Inferences from 40Ar/39Ar and (U-Th)/He thermochronology, *Tectonics*, 21, 1001.

Koppers, A.A.P., 2002, ArArCALC—software for $^{40}Ar/^{39}Ar$ age calculations, *Computer and Geosciences 28, 605-619.*

Leloup, P. H., N. Arnaud, R. Lacassin, J. R. Kienast, T. M. Harrison, T. T. Trong, A. Replumaz, and P. Tapponnier, 2001, New constraints on the structure, thermochronology, and timing of the Ailao Shan-Red River shear zone, SE Asia, *J. Geophys. Res., 106(B4),* 6683-6732.

Meng, Q., Wang, E., and Hu, J., 2005, Mesozoic sedimentary evolution of the northwest Sichuan Basin; implication for continued clockwise rotation of the South China Block, *Geological Society of America Bulletin* 117(3-4), 396-410.

Ministry of Geology and Mineral Resources, 1991, G.M., Regional Geology of Sichuan Province: Geol. Publ. House, Beijing, 728 pp.

Mock, C., Arnaud, N.O., and Cantagrel, J.M., 1999, An early unroofing in northeastern Tibet? Constraints from $^{40}Ar/^{39}Ar$ thermochronology on granitoids from the eastern Kunlun range (Qianghai, NW China), *Earth and Planetary Science Letters* 171, 107–122.

Northrup, C.J., Royden L.H., and Burchfiel, B.C., 1995, Motion of the Pacific plate relative to Eurasia and its potential relation to Cenozoic extension along the eastern margin of Eurasia, *Geology* 23(8), 719–722.

Ouimet, W.B., 2007, *Dissecting the Eastern Margin of the Tibetan Plateau: A Study of Landslides, Erosion, and River Incision in a Transient Landscape.* Ph.D thesis, MIT, Cambridge, MA.

Renne, P.R., Swisher, C.C., Deino, A.L., Karner, D.B., Owens, T.L., and DePaolo, D.J., 1998, Intercalibration of standards, absolute ages and uncertainties in 40Ar/39Ar dating. *Chem. Geol., Isot. Geosci. Sect. 145*, 117–152.

Ritts, B.D., Yue, Y.J., and S.A. Graham, 2004, Oligocene–Miocene tectonics and sedimentation along the Altyn Tagh fault, northern Tibetan Plateau: analysis of the Xorkol, Subei, and Aksay basins, *Journal of Geology* **114,** 207–230.

Roger, F., Calassou, S., Lancelot, J., Malavieille, J., Mattauer, M., Xu, Z., Hao, Z., and Hou, L., 1995. Miocene emplacement and deformation of the Konga Shan granite (Xianshui He fault zone, west Sichuan, China): geodynamical implications. *Earth and Planetary Science Letters* 130, 201–216.

Roger F, Malavieille J, Leloup PhH, Calassou S, and Xu Z. 2004. Timing of granite emplacement and cooling in the Songpan–Garze Fold Belt (eastern Tibetan Plateau) with tectonic implications, *Journal of Asian Earth Sciences* 22, 465–481.

Schellart, W.P., and Lister, G.S., 2005, The role of the East Asian active margin in widespread extensional and strike-slip deformation in East Asia, *Journal of the Geological Society of London* 162, 959-972.

Song, X.Y., Zhou M.F., Cao, Z.M., and Robinson, P.T., 2004, Late Permian rifting of the South China Craton caused by the Emeishan mantle plume?, *Journal of the Geological Society,* 161, 773-781.

Tapponnier, P., G. Peltzer, A. Y. Le Dain, R. Armijo, and P. Cobbold (1982), Propagating extrusion tectonics in Asia; new insights from simple experiments with plasticine, *Geology* 10(12), 611-616.

Wallis S, Tsuijimori T, Aoya M, Kawakami T, Terada K, Suzuki K and Hyodo H, 2003, Cenozoic and Mesozoic metamorphism in the Longmenshan orogen: implications for geodynamic models of eastern Tibet, *Geology* 31, 745–748.

Wang, E., Burchfiel, B.C., Royden, L.H., Chen, L., Chen, J., and Li, W., 1998, Late Cenozoic Xianshuihe-Xiaojiang and Red River fault systems of southwestern Sichuan and central Yunnan, China, *Geological Society of America Special Paper 327*, 108 p.

Yan, D.-P., Zhou, M.-F., Songa, H., and Fu, Z, 2003, Structural style and tectonic significance of the Jianglang dome in the eastern margin of the Tibetan Plateau, China, *Journal of Structural Geology* 25, 765–779.

Yue, Y., and Liou, J. G. 1999. A two-stage evolution model for the Altyn Tagh fault, China, *Geology* 27: 227–230.

Yue, Y.; Ritts, B. D.; and Graham, S. 2001. Initiation and long-term slip history of the Altyn Tagh fault. Int. Geol. Rev. 43:1087–1093.

Zhou, M.F., Yan, D.P., Kennedy, A.K., Li Y., and Ding J., 2002, SHRIMP U-Pb zircon geochronological and geochemical evidence for Neoproterozoic arc-magmatism along the western margin of the Yangtze Block, South China, *Earth and Planetary Science Letters* 196, 51-67.

Figure Captions

Figure 1

Simplified geologic map of the eastern margin of the Tibetan Plateau. Geology from Burchfiel et al. (in preparation) and 1:1,500,000 scale map compiled by Chengdu Institute of Geology and Mineral Resources and the China Geological Survey (2004). Black box indicates the location of figure 2. Figure modified from Ouimet (2007). DMT: Danba Metamorphic Terrane.

Figure 2

Geologic map of the Danba Antiform region. Geology from Burchfiel et al. (in preparation) and Chinese 1:200,000 geologic maps (Ministry of Geology and Mineral Resources, 1991). Gray line indicates the location of the cross section in figure 2b.

Figure 3

Geologic map of the Gezong Dome showing sample locations. Geology based on our mapping and Chinese 1:200,000 geologic maps (Ministry of Geology and Mineral Resources, 1991).

Figure 4

Geologic map of the northwestern part of the Kangding Antiform. Geology based on our mapping and Chinese 1:200,000 geologic maps (Ministry of Geology and Mineral Resources, 1991).

Figure 5

Field photographs from the nose of the Kangding Antiform. A) Roadcut showing folds indicating a normal sense of shear, hammer for scale. B) Folds in fault gouge C) Polished fracture surface, notebook for scale.

Figure 6

Field photographs from Kangding. Upper photograph shows the normal fault with Triassic sedimentary rocks and Precambrian granitic rocks and the thrust fault placing Sinian Carbonate above the Triassic rocks. Locations of the faults within the town and on the hilltop are inferred. Letters A through D indicate the locations of the photographs below. A) Carbonate with bedding clearly visible. B) Triassic metasedimentary rocks, pencil for scale. C) Mylonite modified by brittle faulting D) Precambrian granitic rocks.

Figure 7

Plot of $^{40}Ar/^{39}Ar$ ages with distance across the across the northern boundary of the Gezong Dome. Each blue point represents a muscovite aliquot, each red point represents a single biotite grain. Large points show average age of samples for which the individual aliquot ages are not available. The gray bars show regions with normal-sense shear indicators.

The bar below the plot shows changes in lithology across the transect.

Figure 8

Map showing Rb-Sr and $^{40}Ar/^{39}Ar$ thermochronology data from the Danba region. Data are from Huang et al. (2003b), Wallis et al. (2003), and this study.

Figure 9

Schematic cross sections illustrating the evolution of the Danba region. a,b) South-vergent thrusting of Paleozoic and Triassic sedimentary rocks over Precambrian basement during the Mesozoic, accompanied by high grade metamorphism and folding along E-W trending axes. Followed by E-W compression and folding along N-S trending axes to form domes of high grade rocks (Huang et al., 2003; Huang et al., 2003b; Harrowfield et al., 2005; Burchfiel et al., 1995). Thermochronology data indicates slow cooling from ~165 to ~30 (Huang et al., 2003; Wallis et al., 2003). Note the change in scale between a, b and c, d. c) Uplift of the NW-plunging Danba antiform coincides with extension as the Paleozoic schists move to the NW relative to the Precambrian rocks. d) Miocene surface uplift and initiation of rapid exhumation (Ouimet, 2007).

Sample number	Sample type	Lithology	Age (Ma)	± 2σ	Age range (Ma)
KC05-16	Muscovite	mylonite	27.77	1.435	25.25 - 30.13
KC05-18	Biotite	granite	46.57[a]	2.35	
KC05-18	Muscovite	granite	57.08	4.063	53.11 - 63.97
KC05-19	Biotite	mylonite	25.86[a]	0.77	
KC05-19	Muscovite	mylonite	35.91	1.815	33.28 - 41.03
KC05-20	Biotite	mylonite	28.47[a]	0.59	
KC05-21	Biotite	schist	131.33[a]	2.41	
KC05-21	Muscovite	schist	74.39	9.328	62.99 - 88.16
KC05-22	Biotite	schist	102.03[a]	2.38	
KC05-22	Muscovite	schist	93.295	8.21	81.78 - 104.57
KC05-23	Biotite	schist	30.74	4.322	27.18 - 40.92
KC05-24	Biotite	schist	57.94	1.688	55.05 - 60.60
KC05-24	Muscovite	schist	77.74	2.607	74.07 - 82.56
KC05-25	Muscovite	mylonite	113.5	4.992	104.01 - 119.38
KC05-26	Biotite	mylonite	110.21	10.844	99.83 - 130.89
KC05-26	Muscovite	mylonite	63.27	0.768	62.31 - 65.11
KC05-27	Biotite	schist	77.62	2.584	73.69 - 79.40
KC05-27	Muscovite	schist	102.71	9.198	89.23 - 114.43
KC05-30	Biotite	mafic dike	130.81	4.26	127.42 - 141.66
KC07-60	Biotite	schist	38.1	3.054	31.48 - 42.96
KC07-60	Muscovite	schist	84.91	6.174	78.67 - 100.25
KC07-61	Biotite	schist	63.39	3.068	58.41 - 69.01
KC05-61	Muscovite	schist	74.69	4.483	64.68 - 80.19
KC07-62	Biotite	schist	193.2	6.202	182.86 - 201.37
KC07-62	Muscovite	schist	82.19	7.581	68.77 - 90.81
KC07-66	Biotite	schist	146.75	2.285	143.9 - 152.54
KC07-66	Muscovite	schist	116.37	2.637	111.1 - 119.8

Table 1
$^{40}Ar/^{39}Ar$ data. Ages are the mean of individual analyses weighted by uncertainty. Error given is the 2 sigma uncertainty of the weighted mean.
a) Age and uncertainty given by ArArCalc version 2.40

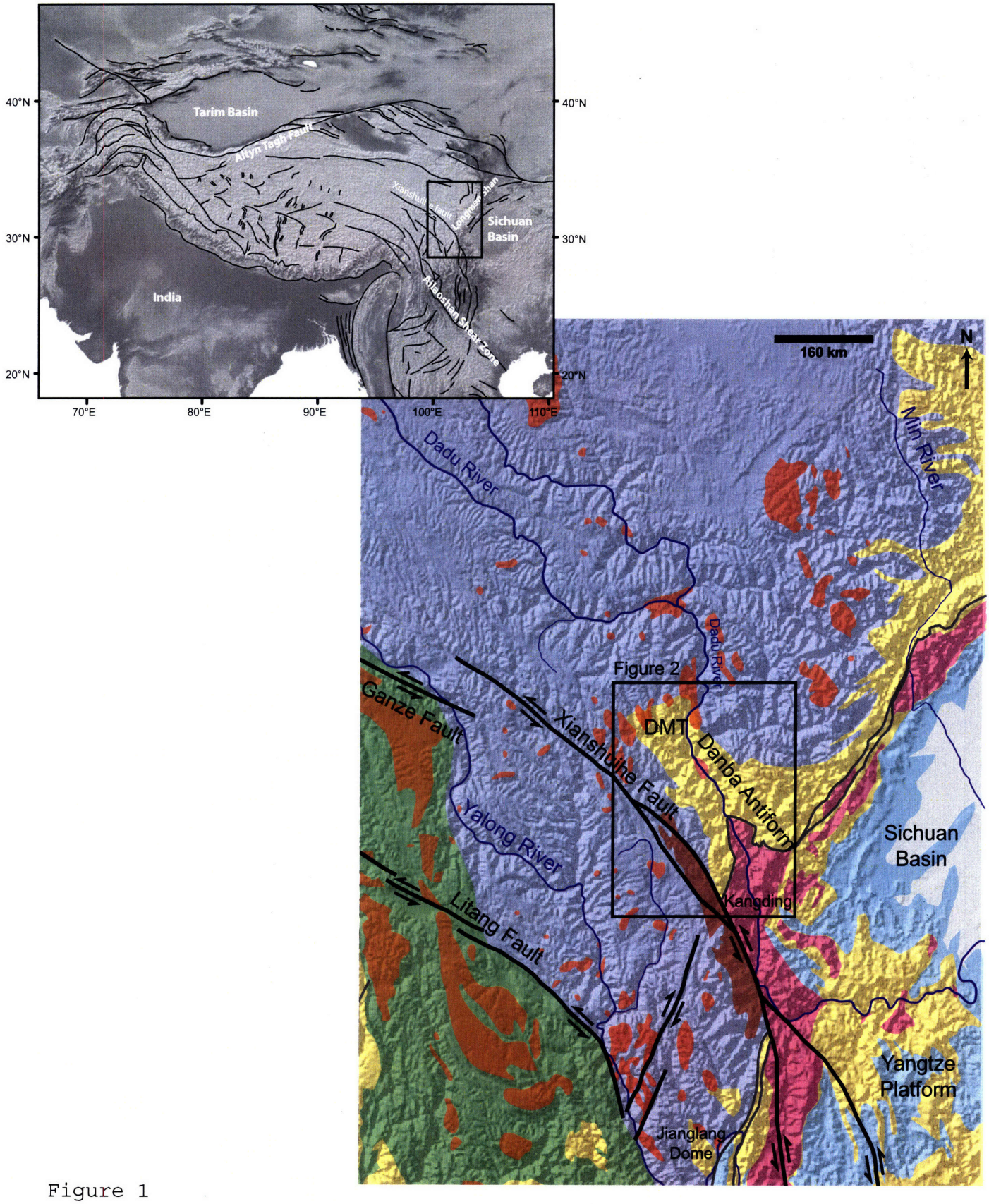
Tarim Basin
Altyn Tagh Fault
Xianshuihe Fault
Longmenshan
Sichuan Basin
India
Ailaoshan Shear Zone
40°N
30°N
20°N
70°E
80°E
90°E
100°E
110°E
160 km
N
Dadu River
Min River
Figure 2
DMT
Danba Antiform
Ganze Fault
Xianshuihe Fault
Yalong River
Litang Fault
Kangding
Sichuan Basin
Yangtze Platform
Jianglang Dome
Miocene Pluton
Cenozoic Sediments
Mesozoic Plutons
Triassic volcanic and sedimentary rocks
Triassic Songpan Ganze flysch
Yangtze Platform Mesozoic rocks
Paleozoic rocks
Precambrian rocks

Figure 1

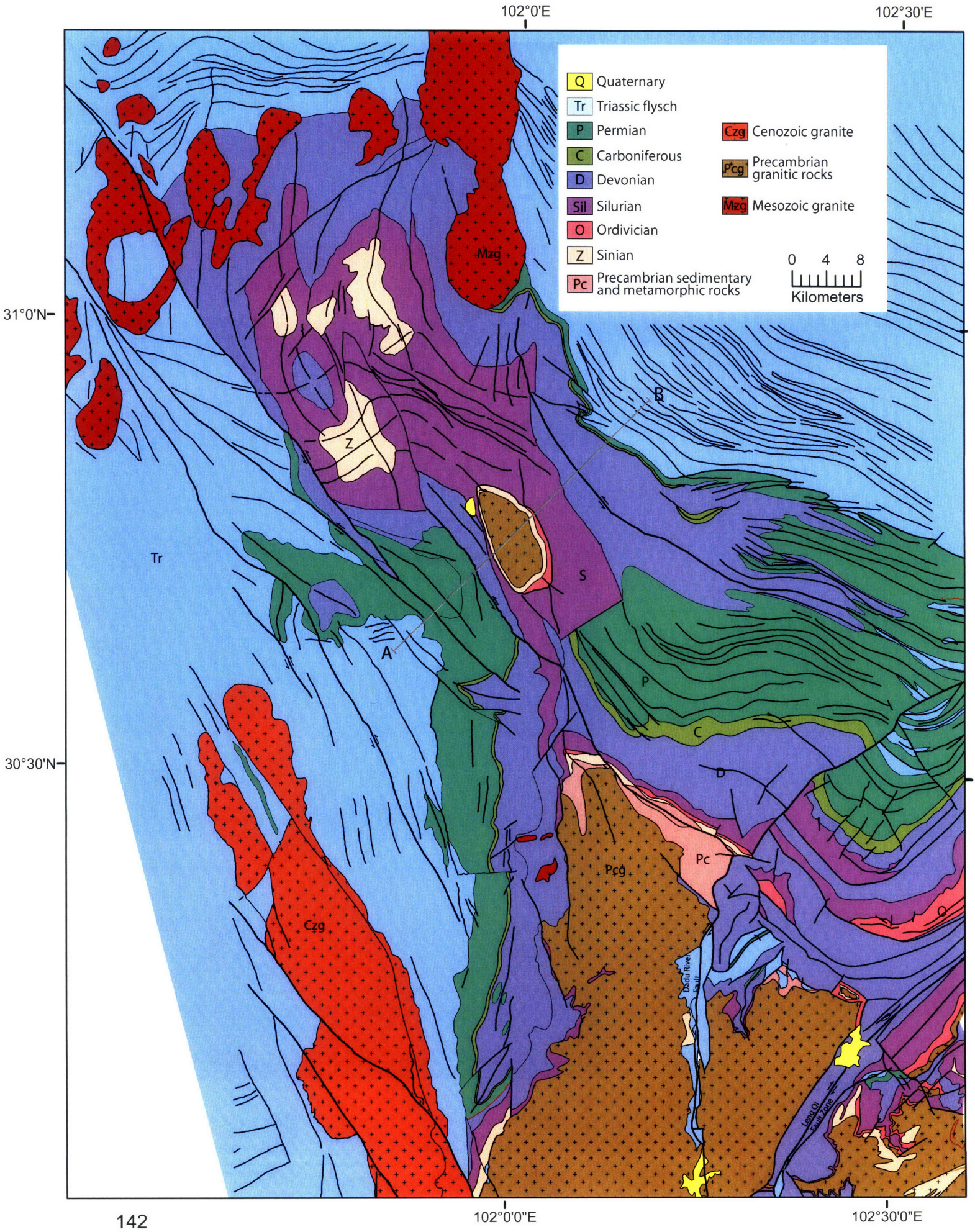
102°0'E
102°30'E
31°0'N
30°30'N
Q Quaternary
Tr Triassic flysch
P Permian
C Carboniferous
D Devonian
Sil Silurian
O Ordivician
Z Sinian
Pc Precambrian sedimentary and metamorphic rocks
Czg Cenozoic granite
Pcg Precambrian granitic rocks
Mzg Mesozoic granite
0 4 8
Kilometers
B
A
Tr
Z
Mzg
S
P
C
D
Pc
Pcg
Czg
O
Dadu River Fault
Lena Qi Fault Zone
102°0'0"E
102°30'0"E

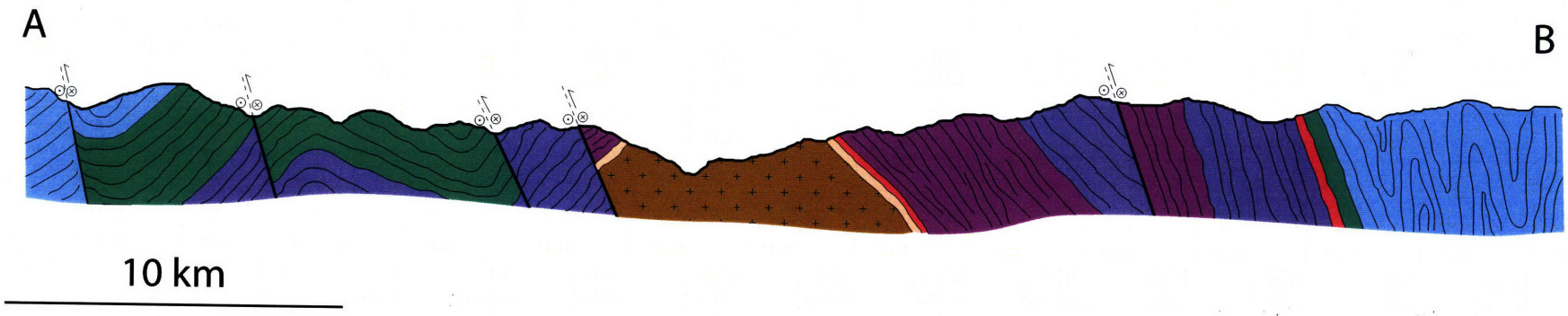
A
B
10 km

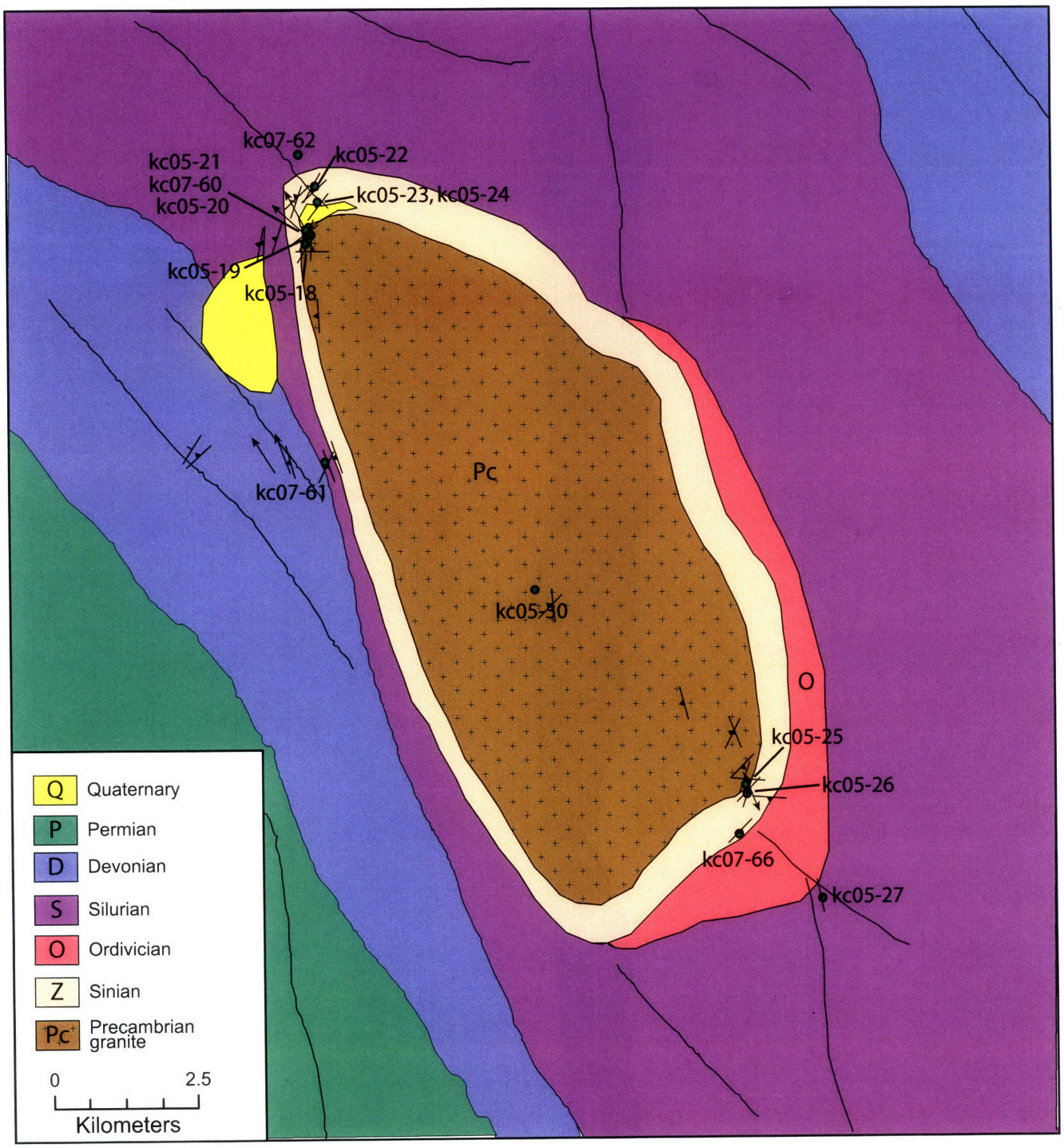
kc07-62
kc05-22
kc05-21
kc07-60
kc05-20
kc05-23, kc05-24
kc05-19
kc05-18
kc07-61
Pc
kc05-30
O
kc05-25
kc05-26
kc07-66
kc05-27
Q Quaternary
P Permian
D Devonian
S Silurian
O Ordivician
Z Sinian
Pc Precambrian granite
0
2.5
Kilometers

Figure 3

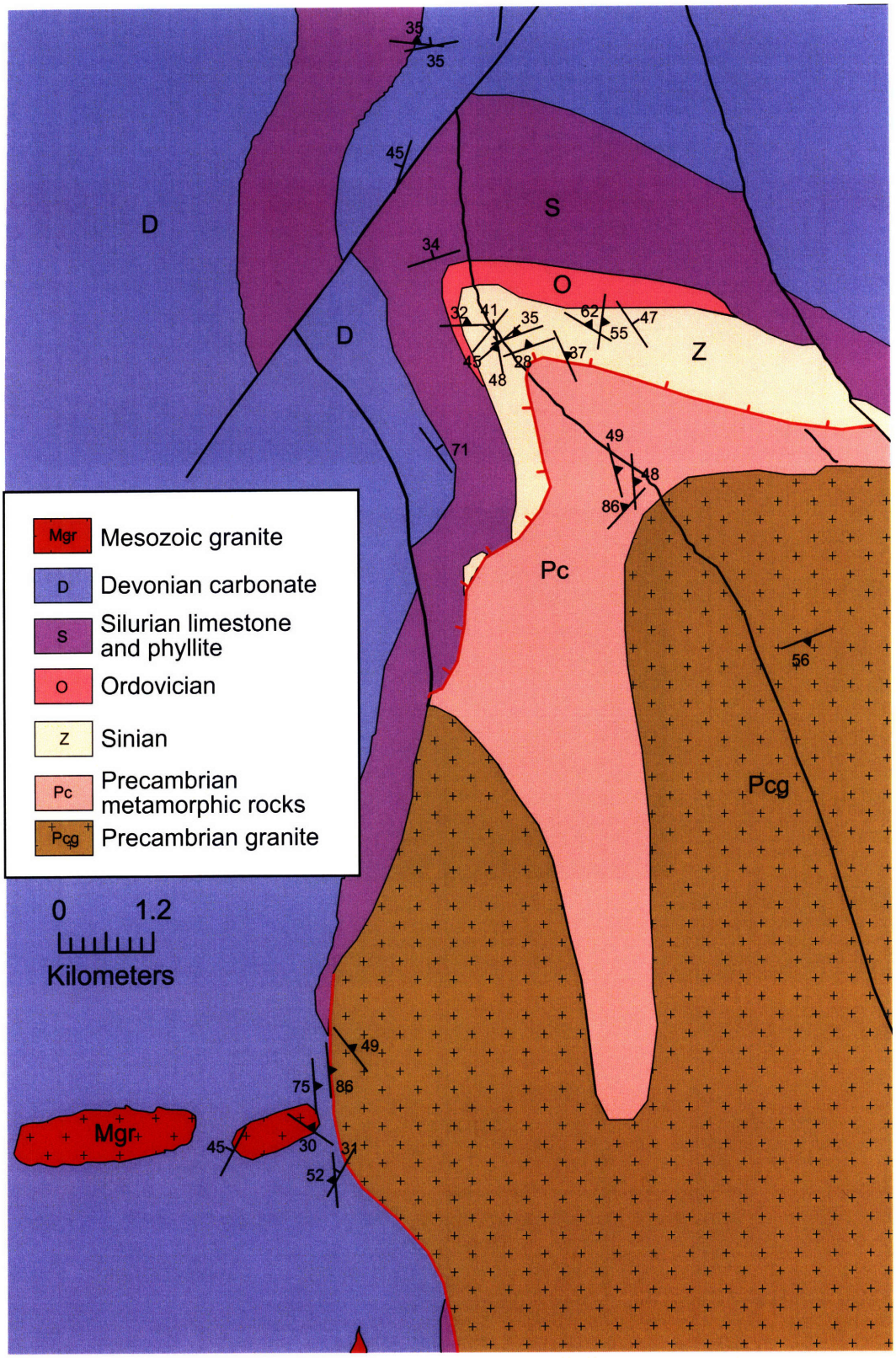
Mgr
Mesozoic granite
D
Devonian carbonate
S
Silurian limestone and phyllite
O
Ordovician
Z
Sinian
Pc
Precambrian metamorphic rocks
Pcg
Precambrian granite
0
1.2
Kilometers
D
S
O
Z
Pc
Pcg
Mgr
35
35
45
34
32
41
35
62
47
55
45
28
37
48
71
49
48
86
56
49
75
86
45
30
31
52

Figure 4

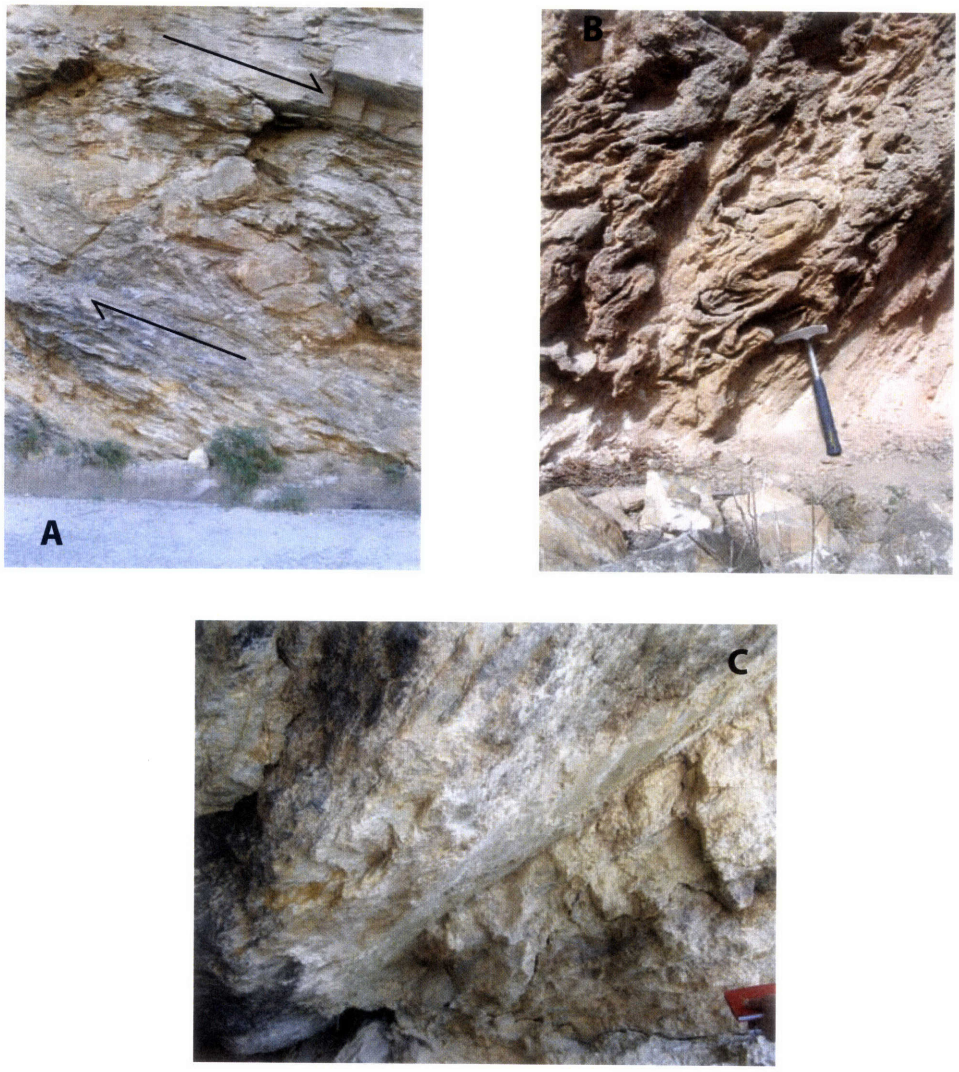

Figure 5

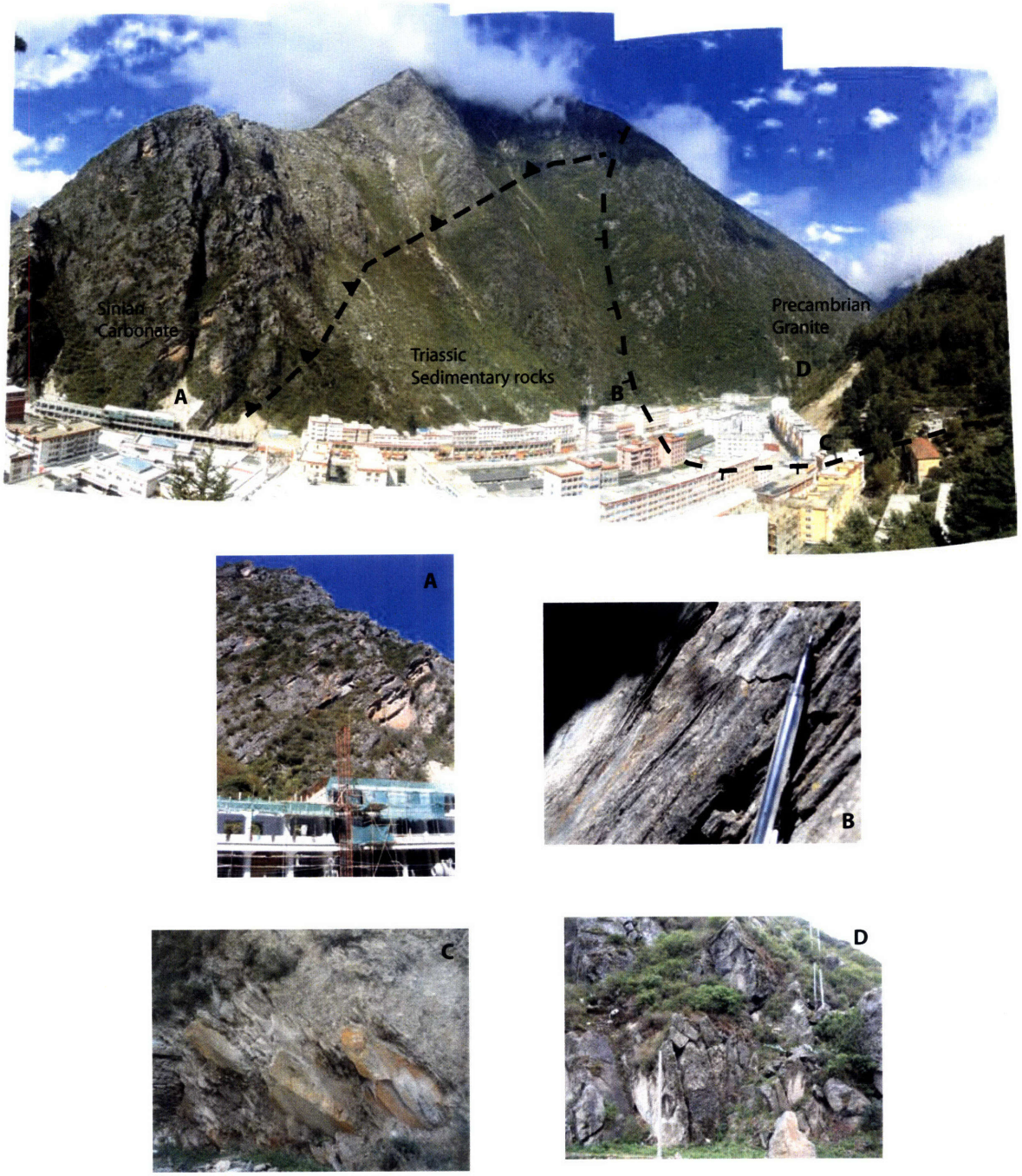
Sinian
Carbonate
Triassic
Sedimentary rocks
Precambrian
Granite
A
B
C
D
A
B
C
D

Figure 6

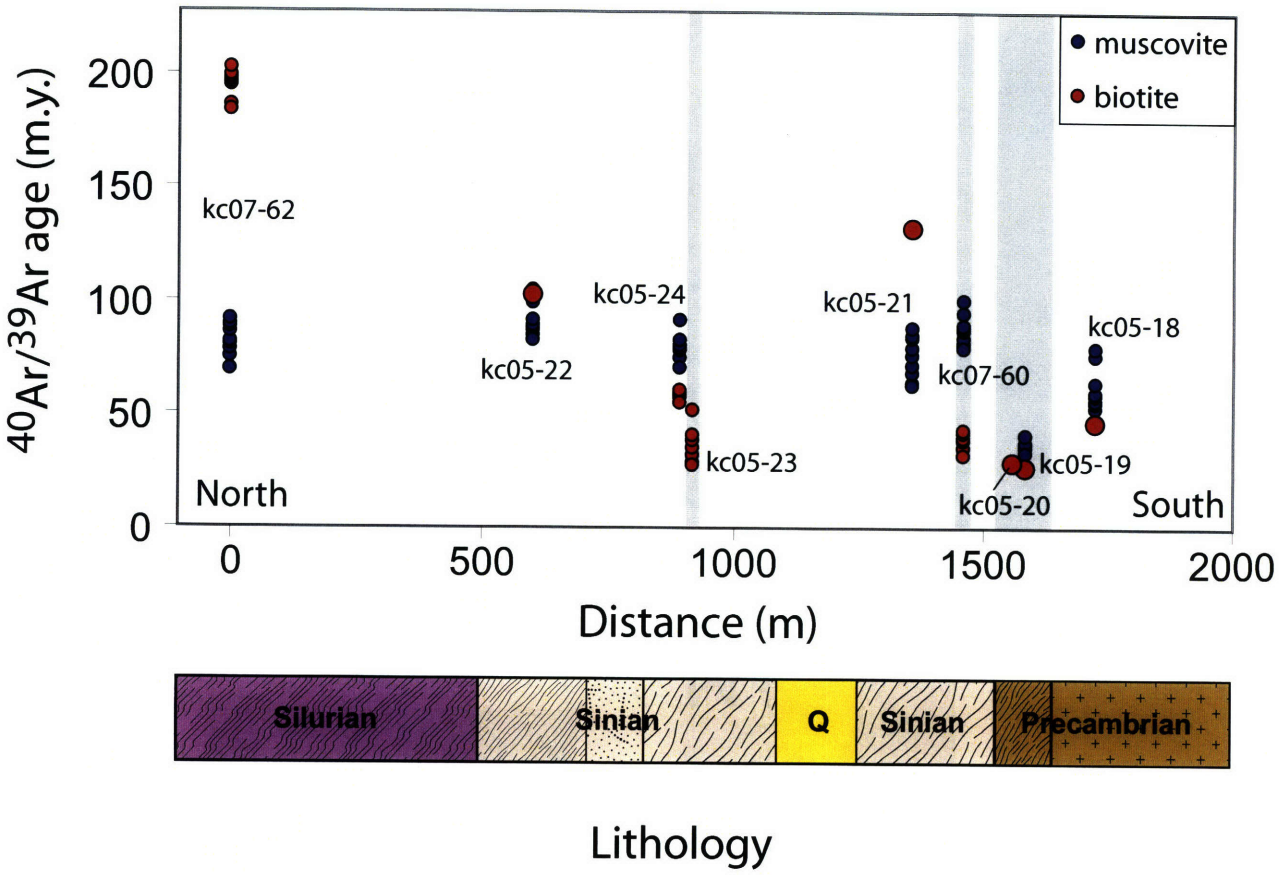
muscovite
biotite
$^{40}Ar/^{39}Ar$ age (m.y.)
200
150
100
50
0
kc07-62
kc05-22
kc05-24
kc05-23
kc05-21
kc07-60
kc05-18
kc05-19
kc05-20
North
South
0
500
1000
1500
2000
Distance (m)
Silurian
Sinian
Q
Sinian
Precambrian
Lithology

Figure 7

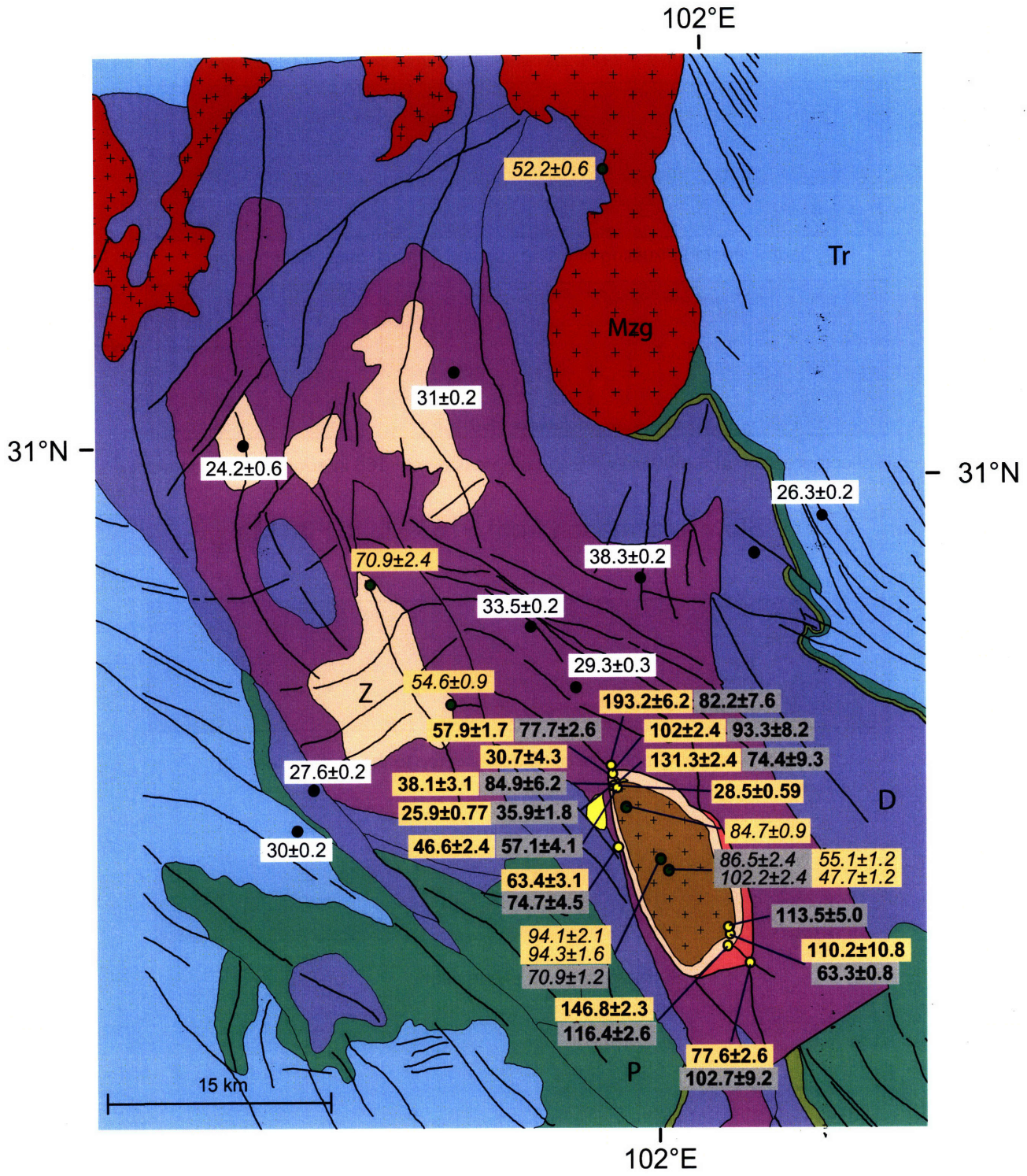

- 24.2±0.6 Biotite Rb-Sr, Huang et al., 2003b
- *70.9±1.2* Muscovite $^{40}Ar/^{39}Ar$, Wallis et al., 2003
- *84.7±0.9* Biotite $^{40}Ar/^{39}Ar$, Wallis et al., 2003
- **74.7±4.5** Muscovite $^{40}Ar/^{39}Ar$, this study
- **63.4±3.1** Biotite $^{40}Ar/^{39}Ar$, this study

Figure 8

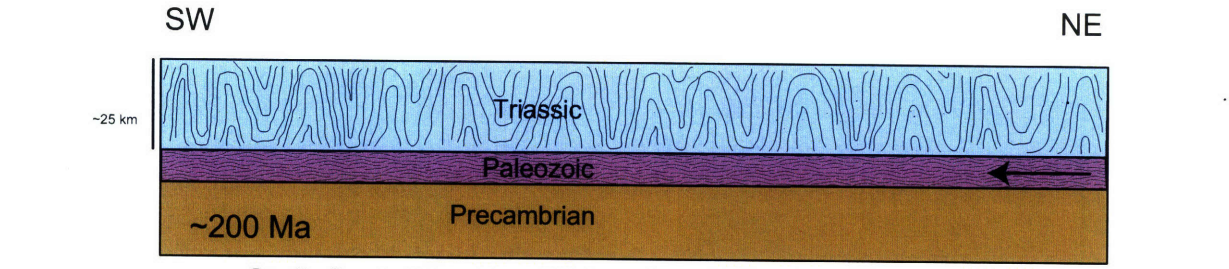

South-directed thrusting of Paleozoic and Triassic over Precambrian

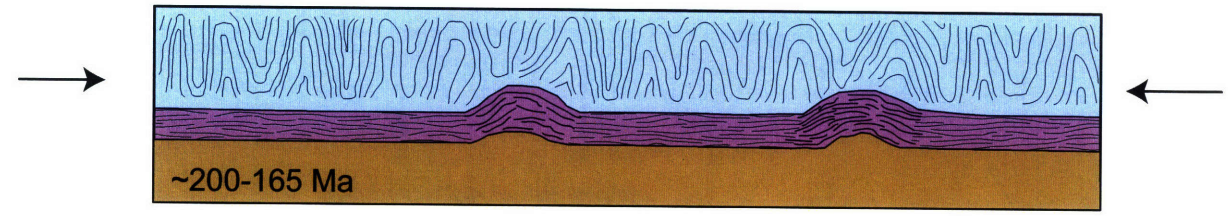

N-S compression at ~200 Ma and E-W compression at ~165 interfere to form domes

Slow exhumation from ~165 Ma to ~30 Ma

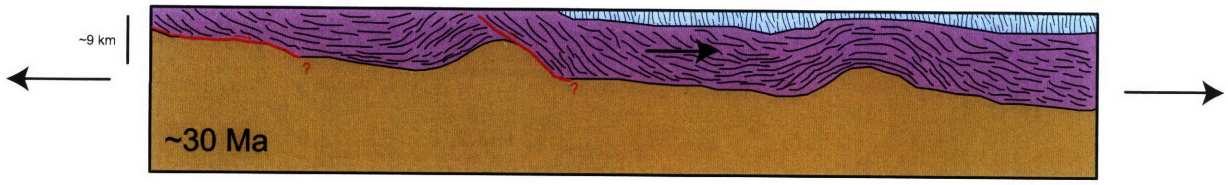

Uplift of N-plunging antiform coincides with top to the north extension

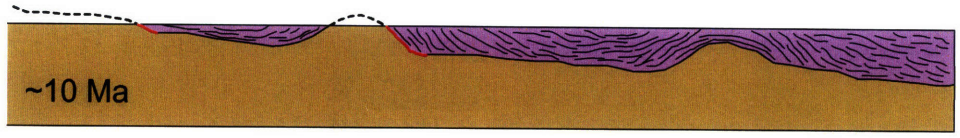

Surface uplift and exhumation

Sample number	Sample type	Lithology	Age (Ma)	± 2σ	Age range (Ma)
KC05-16	Muscovite	mylonite	27.77	1.435	25.25 - 30.13
KC05-18	Biotite	granite	46.57[a]	2.35	
KC05-18	Muscovite	granite	57.08	4.063	53.11 - 63.97
KC05-19	Biotite	mylonite	25.86[a]	0.77	
KC05-19	Muscovite	mylonite	35.91	1.815	33.28 - 41.03
KC05-20	Biotite	mylonite	28.47[a]	0.59	
KC05-21	Biotite	schist	131.33[a]	2.41	
KC05-21	Muscovite	schist	74.39	9.328	62.99 - 88.16
KC05-22	Biotite	schist	102.03[a]	2.38	
KC05-22	Muscovite	schist	93.295	8.21	81.78 - 104.57
KC05-23	Biotite	schist	30.74	4.322	27.18 - 40.92
KC05-24	Biotite	schist	57.94	1.688	55.05 - 60.60
KC05-24	Muscovite	schist	77.74	2.607	74.07 - 82.56
KC05-25	Muscovite	mylonite	113.5	4.992	104.01 - 119.38
KC05-26	Biotite	mylonite	110.21	10.844	99.83 - 130.89
KC05-26	Muscovite	mylonite	63.27	0.768	62.31 - 65.11
KC05-27	Biotite	schist	77.62	2.584	73.69 - 79.40
KC05-27	Muscovite	schist	102.71	9.198	89.23 - 114.43
KC05-30	Biotite	mafic dike	130.81	4.26	127.42 - 141.66
KC07-60	Biotite	schist	38.1	3.054	31.48 - 42.96
KC07-60	Muscovite	schist	84.91	6.174	78.67 - 100.25
KC07-61	Biotite	schist	63.39	3.068	58.41 - 69.01
KC05-61	Muscovite	schist	74.69	4.483	64.68 - 80.19
KC07-62	Biotite	schist	193.2	6.202	182.86 - 201.37
KC07-62	Muscovite	schist	82.19	7.581	68.77 - 90.81
KC07-66	Biotite	schist	146.75	2.285	143.9 - 152.54
KC07-66	Muscovite	schist	116.37	2.637	111.1 - 119.8

Table 1
$^{40}Ar/^{39}Ar$ data. Ages are the mean of individual analyses weighted by uncertainty. Error given is the 2 sigma uncertainty of the weighted mean.
a) Age and uncertainty given by ArArCalc version 2.40

Chapter 5

Characterizing fluvial incision in the Colorado River system in southern Utah: Integrating regional patterns and local rates

Kristen L Cook[a], Kelin X. Whipple[b], Arjun M. Heimsath[b], and Tom Hanks[c]

[a]Department of Earth, Atmospheric and Planetary Science, Massachusetts Institute of Technology, Cambridge, MA
[b]School of Earth and Space Exploration, Arizona State University, Tempe, AZ
[c]U.S. Geological Survey, Menlo Park, CA

In review at *Earth Surface Processes and Landforms*

Abstract

The Colorado River system in southern Utah and northern Arizona is continuing to adjust to the baselevel fall responsible for the carving of the Grand Canyon. Estimates of bedrock incision rates in this area vary widely, hinting at the transient state of the Colorado and its tributaries. In conjunction with these data, we use longitudinal profiles of the Colorado and tributaries between Marble Canyon and Cataract Canyon to investigate the incision history of the Colorado in this region. We find that almost all of the tributaries in this region steepen as they enter the Colorado River. The consistent presence of oversteepened reaches with similar elevation drops in the lower section of these channels, and their coincidence within a corridor of high local relief along the Colorado, suggest that the tributaries are steepening in response to an episode of increased incision rate on the mainstem. This analysis makes testable predictions about spatial variations in incision rates; these predictions are consistent with existing rate estimates and can be used to guide further studies. We also present cosmogenic nuclide data from the Henry Mountains of Southern Utah. We measured *in situ* ^{10}Be concentrations on four gravel-covered strath surfaces elevated from 1 m to 110 m above Trachyte Creek. The surfaces yield exposure ages that range from approximately 2.5 ka to 267 ka and suggest incision rates that vary between 350 and 600 m/my. These incision rates are similar to other rates determined within the high-relief corridor. Available data thus support the interpretation that tributaries of the Colorado River upstream of the Grand Canyon are responding to a recent pulse of rapid incision on the Colorado.

Numerical modeling of detachment-limited bedrock incision suggests that this incision pulse is likely related to the upstream-dipping lithologic boundary at the northern edge of the Kaibab upwarp.

Introduction

The Grand Canyon is thought to be the result of base level fall caused by the integration of the Colorado River drainage system over the edge of the Colorado plateau. Most of the incision in the Grand Canyon portion of the Colorado appears to have occurred between approximately 6 and 1 Ma (Lucchitta 1990; Hamblin 1994), but the extent to which this base level fall has affected the Colorado upstream of Grand Canyon is not clear. The Grand Canyon is considered to begin at Lee's Ferry, where the river leaves weaker Mesozoic sedimentary units and enters more resistant Paleozoic rocks and abruptly steepens. The large knickpoint at this transition is often interpreted as the upstream extent of Grand Canyon related incision, implying that the river upstream of the Lee's Ferry has not yet felt the effects of the large base level fall, and that the incision signal propagates upstream through the migration of this large knickpoint (eg. Karlstrom 2004, 2005; Wolkowinsky and Granger, 2004). In contrast, rapid incision in the Colorado River upstream of Lee's Ferry would suggest that the upper reaches of the Colorado are responding to the lowering in the Grand Canyon and that the knickpoint at Lee's Ferry is not the upstream extent of the incision signal, but may reflect a lithologic influence on channel gradient. Thus, the incision history of the region upstream of Lee's Ferry is critical for evaluating how the Colorado River is responding to the incision of the Grand Canyon, and may provide insight into how large river systems adjust to downstream perturbations.

The advent of surface and burial dating techniques using cosmogenic radionuclides has allowed estimates of incision rates from a number of sites on the Colorado River and its tributaries on the Colorado plateau. Comparing these rates with

estimates of Quaternary incision from within the Grand Canyon should help to determine the nature of the knickpoint at Lee's Ferry and how the signal of Grand Canyon incision is transmitted upstream. However, reported rates vary widely, and their implications are difficult to determine without a regional framework to guide interpretation. In order to provide such a framework, we undertook an analysis of Colorado River incision between Lees Ferry and Cataract Canyon based on tributary longitudinal profiles. This analysis, in combination with new incision rate estimates from a tributary to the Colorado River in the Henry Mountains helps to resolve the regional incision pattern and demonstrates that a pulse of rapid incision has occurred upstream of the Lees Ferry knickpoint since around 500 ka. We also present a simple model of detachment-limited bedrock incision that relates this incision pulse to the interaction between an upstream-dipping lithologic boundary at Lee's Ferry and the propagation of Grand Canyon-related incision up the Colorado River.

Grand Canyon and southern Colorado Plateau incision rates

Incision rates have been measured within the Grand Canyon and in several places on the Colorado and its tributaries upstream of the Grand Canyon in northern Arizona and southern Utah (Figure 1, Table 1, the following location numbers refer to Table 1 and the points marked on Figure 1). Within the Grand Canyon, incision rates range from ~140 m/m.y. in the Eastern Grand Canyon (location 9) to <72-92 m/m.y. west of the Hurricane/Toroweap Fault zone (location 11) (Pederson *et al.*, 2002, 2006). Lava flows on the upper Little Colorado River (location 8) suggest incision at 90-100 m/m.y. since 510 ka (Damon 1974). Terraces near Lee's Ferry (location 4) yield rates ranging from 310 m/m.y. to 480 m/m.y. over the past 80-500 ka (Lucchitta *et al.*, 2000). Cosmogenic exposure ages from gravel covered pediment surfaces draping Navajo Mountain (location 2) suggest that the Colorado River cut most of Glen Canyon over the past ~500 k.y. at

rates of 400±150 to 700±120 m/m.y. (Garvin *et al.*, 2005; Hanks *et al.*, 2001). Terraces at Bullfrog Basin (location 3) suggest 418±11 m/m.y. over the past 480 ka (Davis *et al.*, 2001). Data from the Fremont River north of the Henry Mountains (locations 5 and 6) suggest rates of 300 to 850 m/m.y. (Repka *et al.*, 1997; Marchetti and Cerling, 2001) over the past 150 to 200 k.y. In contrast, a much slower rate of 110±14 m/m.y. over the past 1.36 Ma was measured on the San Juan River near Bluff, Utah (location 7) (Wolkowinsky and Granger, 2004). This low rate, and its similarity to those from the upper Little Colorado (Damon 1974) was interpreted as evidence that the incision of the Grand Canyon has not yet affected the San Juan River. Farther up the system, on the Gunnison River near the Black Canyon of the Gunnison, incision rates range from ~300 m/m.y. downstream of a significant knickpoint to ~100 m/m.y. upstream of the knickpoint (Sandoval *et al.*, 2006). Basalt flows at Glenwood Canyon, farther to the northeast on the Colorado, suggest that the incision rate here has accelerated, increasing from 24 m/m.y. between 7 and 3 Ma to 240 m/m.y. averaged over the past 3 Ma (Kirkham *et al.*, 2001). These incision rate estimates are variable and the sites are geographically widely spaced, making it difficult to infer a coherent regional pattern. Each incision rate has at times been interpreted as representative of the entire region; however, the range of values highlights the non-uniform character of regional incision. We note that these incision rate estimates may also have a high degree of epistemic uncertainty, as the rate that is obtained depends on the model used to interpret the data, and therefore a number of assumptions whose influence may be difficult to quantify. The rates cited above represent the interpretations preferred by the authors of each study.

Analysis of Regional Incision Pattern

In addition to measuring incision rates at individual sites, one can also investigate the degree of response throughout the system by examining topographic data and the longitudinal profile forms of channels. The form of a river's longitudinal profile may

provide information about the presence of a transient response in the river. In a simple model of detachment-limited bedrock channel incision, the response of a channel to a sudden perturbation results in a knickpoint that migrates upstream (Howard, 1994; Whipple and Tucker 2002). In this model, an increase in incision in the Colorado would result in a base level fall for its tributaries, which may be preserved in the long profiles of tributaries as knickpoints. The location of each knickpoint on the long profile will then mark the boundary between the adjusted and unadjusted reaches of the channel (eg. Wobus *et al.*, 2006; Crosby and Whipple, 2006; Schoenbohm et al., 2004).

In a real system, such as the Colorado River, a perturbation will likely result in a more complicated signal that may evolve in complex ways as the landscape continues to respond. The region of the Colorado Plateau that has potentially been affected by the behavior of the Colorado River is quite large and encompasses a range of lithologies, climatic conditions, and underlying structures. Differences in erosional efficiency due to climate, sediment load, or bedrock properties, as well as variations in uplift rate may also result in knickpoints in a channel profile. However, knickpoints due to base level fall may exhibit a systematic pattern in their distribution of elevations and the extent of their retreat along the tributaries (Wobus *et al.*, 2006).

We use USGS Digital Elevation Models (DEMs) of the region with 90m resolution to extract longitudinal profiles of the Colorado and its tributaries, and to characterize the distribution of relief and slopes throughout the region. The construction of the Glen Canyon dam and the presence of Lake Powell have obscured the channel profiles in a significant portion of the area studied. The DEMs do not provide any information about the former course of the Colorado and its tributaries underneath Lake Powell. To supplement these data, we used USGS 7.5 min topographic maps that show the bathymetry of the lake bottom along with topographic maps made prior to the construction of the dam to manually construct portions of the longitudinal profiles under the lake (Figure 2).

All channels extracted from the DEM were examined to ensure that the extraction algorithm did not cut off any meander bends and artificially steepen the profile. The two channels that failed this check were re-extracted using USGS 10m and 30m DEMs. A comparison between the Colorado, San Juan, and Green River profiles calculated from the 90m DEM data and profiles that were manually surveyed in the field (1924 USGS river survey, B. Webb, T. Hanks, pers. comm.) shows that the two methods yield very similar profiles (Figure 2). Thus we are confident that the DEM-extracted profiles faithfully represent the channel forms at the scale of interest.

Morphology of Channel Profiles

As figure 2 illustrates, the long profiles clearly indicate that most of the tributaries downstream of Cataract Canyon do not have the smoothly concave profile typically observed in well-adjusted channels (e.g., Hack, 1957; Flint, 1974). Instead, most tributaries steepen prior to entering the Colorado, and the transition into the lower, oversteepened portion of each channel is marked by either a distinct knickpoint or a broad convex knickzone. The oversteepened reaches extend all the way to the confluence with the Colorado. The elevations of the knickpoints are remarkably similar, and are consistent with the pattern expected from a transient signal of base level fall (Wobus *et al.*, 2006). Notable exceptions to this pattern are the tributaries draining the Henry Mountains. These channels are smoothly concave all the way to the Colorado and will be discussed in more detail below.

In order to estimate the magnitude of incision represented by each knickpoint or convexity, we fit concavity and steepness indices (e.g. Wobus *et al.*, 2006; Schoenbohm *et al.*, 2004) to the upper unadjusted part of the profile, then extrapolate the fit downstream of the rollover and measure the difference between the reconstructed pre-incision elevation and the actual elevation of the channel where it joins the Colorado (Figure 3). The precision of these measurements is limited by the presence of Lake

Powell. However, this method yields a consistent estimate of 150-190m of recent incision for most of the drainages (table 2). The extremely large knickpoint in Dark Canyon is likely structurally controlled, as the steep section occurs where the channel follows the slope of the Monument Upwarp, and the abrupt change in slope corresponds to a change in the orientation of the channel relative to the underlying structure. The knickpoint on the Dirty Devil/Fremont River is at a slightly lower elevation than the other knickpoints and corresponds to a smaller magnitude of incision; this may be due to a more complicated incision signal, and will be discussed further below.

Stationary knickpoints can also form due to differences in the strength or erodibility of the underlying bedrock. A geologic map of Utah (Hintze *et al.*, 2000) indicates that the steep sections do not consistently correspond to more resistant lithologies. On several channels the steep sections pass through a range of lithologies of varying strength, and the top of the knickzone often does not occur near a lithologic contact (Figure 4). For example, the knickpoint on Last Chance Creek is located within the Straight Cliffs Formation, far from the contact with the underlying Tropic Shale or the overlying Wahweap Sandstone (Figure 4b). The knickpoints occur in different lithologies in different tributaries, and it seems unlikely that the pattern observed could be due to lithology alone. It is likely that the lithology plays a role in determining the form of knickpoints and perhaps their propagation speed; however, the consistent presence and height of the convexities, and the lack of convincing correlation with lithology suggest that they are related to a pulse of incision on the Colorado and are not primarily an expression of lithologic contrasts.

The Little Colorado River provides useful point of comparison to the tributaries farther upstream, as the Little Colorado enters the Colorado River downstream of the large convexity at Lee's Ferry, in a reach of the Colorado that has clearly experienced Grand Canyon-related incision. The similarity between the profile of the Little Colorado and the elevation of its knickpoint and the profiles and knickpoints of the tributaries

upstream of Lee's Ferry implies that both have been affected by the same process – the lowering of the Colorado River.

The extent to which the most recent pulse of incision has affected the landscape can be evaluated by examining the geographic pattern of the knickpoints and their relationship to topography and relief. The locations of the knickpoints superimposed on a map of local relief (calculated over a 1.5 km radius moving window) (Figure 5) show that for many drainages there is a correlation between the location of the knickpoint and the distribution of relief along the channel. The reaches downstream of the knickpoints are typically characterized by deeply incised canyons, while the top of the step often corresponds with a reduction in local relief.

Comparison with Published Incision Rate Estimates

When the incision rate estimates are reexamined in light of the regional incision pattern suggested by our analysis (Figure 1), some of the apparent discrepancies in rates can be resolved. Bluff is located upstream of the convexity in the San Juan, so the slow incision rates measured at Bluff (Wolkowinsky and Granger, 2004) are characteristic of a reach that has not experienced the recent incision pulse. In contrast, the rates from Glen Canyon near Navajo Mountain (Garvin *et al.*, 2005; Hanks *et al.*, 2001) were measured downstream of the knickpoint, and therefore reflect the passage of the incision pulse through these reaches.

The fast incision rates measured on the Fremont River (Repka *et al.*, 1997) are not as easily explained, as the knickpoint marked on figures 1 and 2 is located downstream of the study site. However, as noted earlier, the size of this knickpoint is smaller than the rest, and there are additional knickpoints farther upstream on both the Fremont River and Muddy Creek. It is possible that the propagation of the signal up this drainage has been heavily influenced by lithology. The incision rates were obtained from a reach of the

Fremont River that has incised into weak, easily erodable Mancos shale. The lower knickpoint may represent part of the signal that has hung up below the shale, while the rest of the incision may have propagated very rapidly upstream through the shale. Such a scenario is illustrated with our channel incision model and discussed further in that section. Additional incision rate estimates from Muddy Creek and the Fremont and Dirty Devil Rivers are required to evaluate this hypothesis. This style of knickzone separation into upper and lower steps has also been noted in other landscapes with perturbed channels in layered bedrock (e.g., Crosby and Whipple, 2006)

Trachyte Creek Incision Rates

Our simple stream profile analysis suggests that Colorado River in the region between Lee's Ferry and Cataract Canyon (and perhaps farther upstream) has experienced a recent pulse of incision. However, as noted above, the profiles of Trachyte Creek and Bullfrog Creek are smoothly concave; unlike other tributaries in the region, these channels do not contain knickpoints. Trachyte Creek and Bullfrog Creek both drain the Henry Mountains (a group of 5 peaks formed by the mid-Tertiary intrusion of diorite laccoliths into sedimentary units of the Colorado Plateau (Jackson, 1997)), and enter the Colorado in Glen Canyon (Figures 1, 2). Our stream profile analysis predicts that these channels have been affected by an increase in incision of the Colorado River, yet the profiles of the Henry Mountains channels show no evidence of a transient incision pulse. Knowledge of the incision rates on these tributaries will provide an important test of our proposed regional incision pattern, and may help to resolve the nature of response in these drainages. Fast incision rates over recent timescales would imply that that the channels are currently responding to an incision pulse without the development of discrete knickpoints. Fast rates in the past and slow rates on more recent timescales would imply that the channels have fully responded. Slow rates over all time periods

would suggest that the channels have not experienced an incision pulse and would contrast with the regional incision pattern developed above.

Trachyte Creek Surfaces

The Henry Mountains region was studied extensively by G.K. Gilbert (1877) and later Hunt (1953), who both noted that lower slopes flanking the mountains are covered with extensive gravel-covered pediment surfaces of varying height above adjacent channels (Figure 6). In addition, many of the drainages in the area are flanked by series of smaller gravel-covered strath terraces. We use *in situ* cosmogenic nuclides to date the abandonment of a series of these surfaces and determine an incision rate for Trachyte Creek. The use of cosmogenic nuclides in measuring surface exposure ages has been developed by a number of authors (Anderson *et al.*, 1996; Bierman and Nichols, 2004; Granger and Muzikar, 2001; Hancock *et al.*, 1999; Repka *et al.*, 1997; Perg *et al.*, 2001; Gosse and Phillips, 2001), and these studies can be referred to for a detailed analysis of the methods and assumptions.

Samples for cosmogenic nuclide exposure age analysis were collected from a suite of four gravel-covered strath surfaces that rise from 1m to 110m above the bed of Trachyte Creek, an active stream channel that joins the Colorado river ~22 km downstream of the study area (Figure 7). The terraces are cut into Entrada sandstone, a cliff-forming fine-grained red sandstone, and the edges of each terrace remain well defined (Figure 7). The terraces consist of beveled bedrock surfaces covered with gravel deposits that range from one to eight meters thick (Figure 7b,d). The gravel deposits are primarily (up to 95%) diorite in composition, with some sandstone and quartzite clasts, and significant pedogenic carbonate in the older deposits. The clasts are poorly sorted, and range from fine-grained sand to boulders up to a meter in diameter. The surfaces show little evidence of deflation or erosion, particularly the lower two levels. This suite of terraces was selected for their high degree of preservation, their proximity to an active

drainage of significant size, and the presence of 4 distinct levels, P1-P4, that can be visually correlated across several surface remnants (Figure 6, Figure 7b,c).

We obtain a rough estimate of the minimum age of each gravel deposit from the degree of pedogenic carbonate development in the gravel using the classification scheme of Machette (1985) and the age estimates of Lucchitta *et al.* (2000). It should be noted that disturbance or stripping of part of the deposit can remove accumulated carbonate, so this method can yield only an approximate minimum age.

P1 is the highest level at ~110m above creek and is covered with a gravel deposit up to 8 m thick. The gravel surface has moderate development of desert pavement. There is pedogenic carbonate lag present on the surface, suggesting that some deflation of the deposit has taken place. The gravel contains a thick layer (2-2.5m) of well-cemented carbonate at the base of the deposit that appears be related to groundwater, and therefore cannot be used to estimate deposit age. A correlative surface north of the creek contains carbonate classified as stage IV, indicating a minimum age between 250 ka and 525 ka (Machette, 1985; Lucchitta *et al.,* 2000).

The P2 surface covers a much larger area, and is ~62 m above the creek. Surfaces of this level can be correlated in several places south of Trachyte Creek, but are not observed north of the creek. The gravel deposit is several meters thick and contains a well developed carbonate horizon that corresponds to stage III or incipient stage IV carbonate development and implies an approximate minimum age of 100 to 250 ka. The sampled pediment is quite flat, but there is evidence of deflation, as boulders and carbonate lag are present on the surface. The surface has a moderately well developed desert pavement, in which diorite clasts have accumulated desert varnish, indicating that recent disturbance has been minimal.

The P3 terraces define a laterally extensive level cut into bedrock about 7m above Trachyte Creek. Surfaces of this level are present on both sides of the creek and can be visually correlated along much of the creek (Figure 6, 7). The gravels vary in thickness,

but are typically several meters thick. There is no evidence for deflation or erosion of the gravel deposit; however most of the surface is covered with several cm of red silt, indicating some inflation. There is slight carbonate development in the gravels, characteristic of a stage I carbonate, which suggests that this terrace level is less than 100,000 years old (Lucchitta *et al.*, 2000).

P4 denotes the lowest terrace level. The base of the ~1m thick gravel deposit is about 1m above modern Trachyte Creek. This level is fairly small in area, but can be visually correlated in several places along the creek. The top of the gravel surface is extremely flat and shows no evidence of deflation or erosion. In most places there is a layer of silt/fine sand deposited above the gravels, which increases in thickness away from the creek toward the base of the cliff on the edge of P3. The gravel contains no pedogenic carbonate.

Sample collection and analysis

We collected samples from surface boulders and cobbles on levels P1 and P2. Inherited ^{10}Be concentration in these samples is likely to be small compared to *in situ* ^{10}Be, and the degree of carbonate cementation in the gravel made depth profiles impractical. We collected depth profiles from levels P3 and P4 since inheritance is likely to be significant for these lower surfaces relative to their abandonment ages. Each depth profile consists of 4 or 5 samples, where each sample is an amalgamation of at least 50 clasts (Repka *et al.*, 1997), taken at regular intervals from the surface to the base of the gravel deposit (P4) or a depth of 1.7 m (P3). We also collected a sample from the sandstone bedrock below the base of the P4 gravel, as well as two samples of active bedload from Trachyte Creek.

The extraction of ^{10}Be from the samples and AMS target preparation was performed at the Cosmogenic Radionuclide Laboratory at Dartmouth College following the method of Heimsath *et al.* (2001). AMS analysis was done at Lawrence Livermore

National Laboratory. We use the production rates of Stone (2000) corrected for latitude and elevation using the scaling factors of Dunai (2000). The shielding correction for the surfaces sampled was negligible (less than 1%).

Cosmogenic Data

Results from P1 and P2 surface samples are given in table 3. The three samples from the highest level, P1, range from 205 to 267 ky. The oldest of these can be taken as a minimum for the age of the surface. This minimum age of 267 ± 7.7 ka. is consistent with the 250-525 ka range estimated from pedogenic carbonate development in the gravel deposit. An age of 267 ka for this surface 110 m above the creek corresponds to a maximum incision rate of 412±21 m/m.y.

The three surface samples from P2 yield ages ranging from 159-178 ka. The similarity between these ages suggests that inheritance is either relatively small, or is consistent between the samples. A minimum age of 178 ± 7.9 ka agrees with the 100 to 250 ka range suggested by observations of carbonate development and implies a maximum incision rate of 350±28 m/m.y.

We calculate an age from the P3 depth profile by correcting the production rate for depth below the surface, using $P(d) = P_0 e^{-d\rho/\Lambda}$ with Λ = 160 g cm^{-2} and a density of 2.5 g/cm^3 (where P is the production rate, d is depth below the surface, ρ is the density of the gravel, and Λ is the absorption mean-free path). For a profile with uniform age and average inheritance, the depth-corrected production rate and concentration should have a linear relationship; a fit to the data gives the age and average inherited concentration (Figure 8). The P3 profile suggests an age of 13.3±1.1 ka and an average inheritance of 1.03e5±5.3e3 atoms ^{10}Be/gm quartz. This age is consistent with the degree of carbonate development in the gravel and suggests an incision rate of 527±86 m/m.y. The inherited concentration is equivalent to 6920±496 years of exposure at the sample site, or an

upstream basin-average paleo-erosion rate of 151±15.3 m/m.y., assuming no exposure during fluvial transport (Bierman and Nichols, 2004; Granger *et al.*, 1996). The average inheritance obtained from this fit is similar to the 8.5e4±2.5e3 atoms ^{10}Be/gm quartz measured in modern Trachyte Creek gravel. The ^{10}Be concentration in the creek gravel corresponds to an upstream basin-average paleo-erosion rate of 184±14.5 m/m.y., or 5920±455 years of exposure at the sample site.

The P4 depth profile does not exhibit any consistent relationship between concentration and depth and therefore cannot be used to calculate a reliable age for this surface (Figure 9). This depth profile suggests a more complicated exposure history or distribution of inherited nuclides, as the deepest sample has the highest concentration of ^{10}Be. The gravel deposit does not contain structures that would indicate multiple depositional or erosional events; however, a nearby fill terrace at a similar height above the channel provides evidence for an episode of aggradation and reincision. The deepest sample may therefore represent an earlier depositional event. The ^{10}Be concentration of the upper three samples is only slightly higher than the inherited concentration measured in P3 and the stream sediments, so inheritance is likely overwhelming any age signal that may exist. Although the depth profile cannot be used to date the formation of terrace P4, the sample of bedrock at the base of the P4 gravel deposit yields an age of ~3 ka if no previous exposure and a constant burial depth is assumed. This suggests an upper constraint for the age of this terrace, although it is likely that the amount of gravel cover has varied. The concentration of ^{10}Be measured in the bedrock could accumulate in only ~700 yr of exposure at the surface, so the terrace may be significantly younger than 3 ka. An age of 3 ka corresponds to a minimum incision rate of 330 m/m.y. Although the uncertainty in terrace age and the possible intervals of aggradation render this rate extremely unreliable, there is no data suggesting that channel incision during this most recent time period was significantly slower than the rates obtained from the older surfaces.

The ^{10}Be concentrations measured in the P3 depth profile also deviate slightly from the expected exponential profile, as ^{10}Be concentration does not uniformly decrease with depth. This suggests that either inheritance varies systematically with depth, or that inheritance is highly variable and the amalgamation technique was not sufficient to average out random variations. Recent studies have suggested that variability in ^{10}Be concentration in sediment samples collected from active channels is highly dependent on grain size. Samples made up of pebble sized clasts tend to have lower reproducibility than samples of sand sized sediment, as fewer total clasts are included in the analysis (Bierman *et al.*, 2001, Belmont *et al.*, 2006). The samples collected from the P3 gravel are likely to contain highly variable amounts of inheritance due to the heterogeneity of the gravel clasts. The quartz-bearing lithologies in the gravel include locally derived sandstone that breaks down rapidly in modern streams, as well as more resistant quartzite clasts sourced from farther upstream that may have been in the fluvial system for a longer period of time. Variations in the erosion rate of the source rock, as well as possible recycling of clasts from older terraces may also contribute to the variation in inheritance. The stratigraphy of the deposit does not indicate a change in composition or multiple episodes of deposition. It therefore seems unlikely that there is a systematic variation in inheritance, and suggests that the observed concentrations merely reflect the large random variability inherent in samples of heterogeneous clasts. Although the P3 deposit in Trachyte Creek does not show evidence of multiple deposition events, we did note the presence of fill terraces up to 10m high in Trail Canyon, a channel that drains the Henry Mountains farther to the south and joins Trachyte Creek about 12 km downstream of our study site and 10 km upstream of the confluence with the Colorado River. Thus there has been aggradation elsewhere in the system, and we cannot rule out the possibility that the P3 gravels were deposited in a later depositional event and are younger than the terrace itself. The incision rate of 527±86 m/m.y. obtained from the P3 deposit should therefore be considered a maximum rate.

Implications for Trachyte Creek incision

The surfaces range from at least 267 ka to ~3 ka, and exposure ages increase with elevation of the surfaces. Although the ages for the upper two terraces are minimums and the lower two terraces yield approximate ages, the rates calculated are quite consistent, ranging from 350 m/my to 527 m/my (Figure 10). This suggests that overall, incision has been steady for the past ~270 ky. The rates from Trachyte Creek are similar to those obtained nearby in Glen Canyon (Garvin *et al.*, 2005; Hanks *et al.*, 2001) and at Bullfrog Basin (Davis *et al.*, 2001), and significantly higher than recent rates in the Grand Canyon (Pederson, 2002) and at Bluff, Utah (Wolkowinsky and Granger, 2004). The relatively consistent, rapid incision rates estimated for Trachyte Creek suggest that this channel is in fact responding to the recent rapid incision of the Colorado River, and the lack of a knickpoint in the channel suggests that Trachyte Creek is responding to the incision pulse in a continuous way. The elevation at which these rates were measured also suggests that Trachyte Creek is not responding in a detachment-limited manner. Stream-power based incision models predict that the vertical migration rate of transient knickpoints should be uniform throughout a simple detachment-limited system (ie. Niemann *et al.*, 2001; Whipple and Tucker, 2002). The study location on Trachyte Creek is at an elevation of ~1450 m – about 200 m higher than the knickpoints seen in the other channels in this region (Table 2); the presence of rapid incision at this site since at least ~270 ka suggests that the incision pulse was able to rapidly advance up the channel without forming a discrete knickpoint. Both theory and landscape evolution models predict that transport limited, or dominantly alluvial, channels will rapidly smooth out knickpoints and maintain a regular, concave profile even as they respond to perturbations (Whipple and Tucker, 2002; Crosby *et al.*, 2007, Whipple 2004) and that such perturbations will rapidly sweep upstream. The combination of extremely durable diorite gravel and weak, easily abraded bedrock in the Henry Mountains channels may drive them towards an essentially

transport-limited condition (Johnson *et al.*, in review). Johnson et al. (in review) refer to these channels as sediment-load dominated bedrock channels. Channels that tap into a source of diorite typically contain a high sediment load that is dominated by diorite clasts. Johnson *et al.* (in review) show that diorite-rich channels in the Henry Mountains tend to not have the knickpoints due to lithologic variations that are seen in nearby diorite free channels. We infer that knickpoints have likewise not formed in response to the recent pulse of baselevel fall on the Colorado river along these bedload-rich channels; with the greater availability of abrasion tools (hard diorite clasts; Sklar and Dietrich, 2004) incision of these channels has been able to more closely keep pace with the rate of baselevel fall. This highlights the importance that sediment supply and lithology can have in determining the response of a channel to perturbations.

Channel incision Model

To further investigate the interaction between lithologic variations and transient knickpoints, we follow an approach similar to that of Stock et al. (2004), and model channel evolution using a detachment-limited model of bedrock channel incision based on the equation $E = K_{eff} A^m S^n$ (where E is the incision rate, A is the drainage area and S is the slope at each point). Our model includes both a critical shear stress and a stochastic distribution of precipitation and discharge through the K_{eff} term. K_{eff}, calculated each timestep at each point, is a complex function that incorporates a number of different parameters, including the critical shear stress, the frequency and magnitude of precipitation events, the slope at each point, and the effect of lithology on erodability (eqn 7 in Snyder et al., 2003; eqn 23 in Tucker, 2004). For a full derivation and discussion of the equations used in this model, see Tucker (2004).

We seek to illustrate how key elements of the Colorado River system are expected to influence both its longitudinal profile, the distribution of knickpoints in the Colorado

and its tributaries, and the spatial and temporal variations in incision rate. Accordingly, we use the configuration of the Colorado River to guide model setup. However, we emphasize that our model is intentionally kept simple – sufficiently well elaborated to provide novel insight, but admittedly inadequate to accurately reproduce the modern river profile and its incision rate history. In other words, our modeling is exploratory in nature and we do not attempt to use observations to quantitatively constrain model parameters. We assign a simple distribution of lithologies; in the first case we use two flat-lying layers of different strengths, and in the second case a lithologic distribution suggested by sections along the Colorado River (ie. Karlstrom, 2005). The initial channel profile was obtained by running the model with the given lithologic distribution until the profile reached a steady state and incision was balanced with a background uplift rate of 100 m/m.y. This uplift rate is suggested by incision rates on the upper Little Colorado (Damon 1974), the upper San Juan (Wolkowinsky and Granger, 2004) and recent rates within the Grand Canyon (Pederson *et al.*, 2002, 2006). We then impose an abrupt, discrete base-level fall on the initial profile and allow the profile to adjust. Because several of the model parameters are amalgamations of different factors, their value is difficult to determine physically; we tuned the values of these parameters to best match the slope of the Colorado River and the rates of incision in the Glen Canyon region. Values for the parameters describing the stochastic distribution of precipitation were suggested by Tucker and Bras (2000).

As figure 11a illustrates, a perturbation in layered rocks where the lower layer is more resistant than the upper layer can split into two discrete knickpoints that propagate upstream at different rates. The lower knickpoint is controlled by the lithologic boundary, and moves upstream much more slowly than the upper knickpoint, which can rapidly sweep upstream through the weaker rock. Because the knickpoints in this model are in response to a single discrete pulse of incision, rather than a lasting change in rock uplift rate or rate of base-level fall, the portions of the channel above the upper knickpoint and

below the lower knickpoint are incising at the same rate. This type of knickpoint partitioning may explain our observations of the Dirty Devil/Fremont River.

In the context of the Colorado Plateau, a more realistic scenario is the presence of an upstream-dipping lithologic contrast such as the contact between the resistant units of the Kaibab upwarp and the weaker rocks upstream (Figure 11b). In this case, a single knickpoint propagates upstream until it reaches the contact between rocks of contrasting strength. The signal is then divided into two parts. The lower knickpoint remains localized on the lithologic boundary, and because the boundary is dipping upstream, the knickpoint lowers in elevation as it moves upstream. This provides a prolonged signal of relative base-level fall to upper section of the channel. The upper knickpoint sweeps rapidly through the weaker bedrock until, in the model illustrated here, it encounters the more resistant bedrock again and propagation slows. As the profile evolves, the upper knickpoint grows while the lower knickpoint shrinks, and the incision rate in the reach between the two knickpoints remains high and is controlled by the retreat rate of the lower knickpoint and the dip of the resistant unit. This simple example illustrates that not only is the relative strength of the bedrock important, but that the orientation of strength contrasts also play a very important role in determining the way in which incision is distributed in space and time along the river. These results suggest that the late incision pulse (initiation at ~500 k.y.) we see upstream of Lee's Ferry is related to the interaction of a knickpoint propagating up through the Grand Canyon with the upstream-dipping boundary of the Kaibab uplift.

We reiterate that this modeling is not intended to reproduce the Colorado River and its incision history, or to predict incision rates, but instead to isolate and therefore illustrate the effect of dipping lithologic boundaries. The models illustrated in Figure 11 describe a strictly detachment-limited system; however the Colorado River contains reaches that are likely closer to a gravel-bedded transport-limited system. This could cause the incision pulse to diffuse out upstream of Lee's Ferry and prevent the formation

of a discrete upper knickpoint, and may result in a steeper channel downstream of the lower knickpoint as incision is distributed over a broader zone. We also ignore a number of other factors that influence and tend to steepen the profile of the Colorado, particularly in the Grand Canyon region, including the effect of tributary debris flows (Hanks and Webb, 2006), possible lithologic effects associated with incision into crystalline basement, and motion along the Toroweap Fault (Pederson *et al.*, 2002).

Discussion

Timing and extent of incision pulse

Both the channel profiles and our new incision rates for Trachyte Creek indicate that the Colorado River in the Glen Canyon region has experienced a recent pulse of rapid incision. The timing of the incision pulse in this region is not well constrained. Surfaces as old as ~500 ka yield high incision rates, suggesting 500 ka as a minimum age for the onset of rapid incision (i.e., Hanks *et al.*, 2001). However, these rates are averaged over the age of the surfaces, and therefore don't preclude the possibility of a post-500 ka acceleration in incision. The initiation of rapid incision around 500 ka is consistent with the magnitude of the incision pulse that we see in the Glen Canyon region and the incision rate estimates in the region. 500 k.y. of incision at an average rate of 350 to 450 m/m.y. results in a total of 175 to 225 m of incision. This is similar to the knickpoint heights of 150 to 200 m that we measured in our analysis of channel profiles, and further supports our interpretation that these knickpoints are related to a pulse of rapid incision in the past 500 k.y., which our modeling suggests is the time when an advancing knickpoint associated with Grand Canyon incision breached the Kaibab Upwarp.

The upstream extent of this signal in the Colorado itself is unclear. There is a large knickpoint of similar size on the Colorado at Cataract Canyon; however, Webb *et al.* (2004) suggest that this knickpoint is the result of a rapid input of sediment due to frequent debris flows in the Holocene, and not due to transient bedrock incision. The

relationship between the large knickpoint and relatively fast incision rates on the Gunnison River, a major tributary that enters the Colorado upstream of Cataract Canyon (Sandoval *et al.*, 2006) and the incision pulse in southern Utah is likewise unclear. The knickzone in the Black Canyon of the Gunnison is of similar magnitude (~200m) and the incision rate is similar, but there is no corresponding knickpoint on the North Fork of the Gunnison and the Black Canyon knickzone may reflect local structural uplift (Sandoval et al., 2006). Berlin and Anderson (2007) also note large knickpoints on tributaries to the Colorado draining the Roan Plateau. However, incision rates on these tributaries have not been directly measured. These knickpoints are heavily influenced by lithologic strength contrasts and are too large (~800m above the Colorado) to be attributed solely to the incision pulse discussed here. In addition, the tributary reaches downstream of the knickpoints grade smoothly into the Colorado River (Berlin and Anderson, 2007). This suggests that these knickpoints are related to incision over a much longer timescale than the incision pulse seen farther downstream, as suggested by Berlin and Anderson (2007).

In order to further characterize the timing and spatial extent of this incision pulse and define its relationship to the knickpoints shown in Figures 1 and 2, more estimates of incision rates upstream and downstream of the knickpoints on these drainages are necessary. Our analysis provides a framework for the collection of further incision rate data from tributaries of the Colorado. Understanding the context of incision rate estimates is crucial for extrapolating those rates upstream/downstream or to other parts of the system.

Regional Implications

As more incision data becomes available throughout the region, we can better constrain the spatial and temporal variations in incision rates, and can asses the importance of forcings such as localized deformation, regional uplift, base level fall, and climate. For example, Pederson et al. (2007) suggest that recent rapid incision on the

Colorado Plateau is primarily related to a "bullseye" of regional epeirogenic uplift, rather than the propagation of incision up the Colorado River. This assumes that the rivers are in equilibrium with the landscape, so that incision rates are in balance with uplift rates, but the pattern of knickpoints described above suggest that the upper and lower reaches of the channels are not in equilibrium and that the system is in a transient state. While regional uplift may be contributing to the incision on the Colorado Plateau, it does not explain the pattern that we observe in the channel profiles in southern Utah.

Our observations may also help resolve the nature of the large knickzone at Lee's Ferry – whether it is primarily a response to the transition from weak sedimentary rocks in the Glen Canyon region to the more resistant units of the Grand Canyon Group, or primarily a transient knickpoint that is sweeping upstream. The recognition of a recent pulse of incision on the Colorado immediately upstream of Lee's Ferry indicates that this reach of the Colorado River is responding to the incision of the Grand Canyon, and that the Lee's Ferry convexity does not represent the upstream extent of the incision signal. In addition, the difference in incision rates upstream and downstream of Lee's Ferry indicates that this reach of the Colorado River is not in equilibrium, and that the Lee's Ferry convexity is not a static knickpoint solely due to the presence of a resistant lithology. As the modeling results illustrate, the large convexity is likely due to a combination of transient and lithologic effects, where a portion, but not all of the incision signal has become localized at the lithologic boundary near Lee's Ferry.

Our modeling also predicts a relationship between the initiation of rapid incision in Glen Canyon and the slowing of incision in the Grand Canyon. As figure 12a illustrates, rapid incision upstream of Lee's Ferry does not begin until headward incision reaches the boundary between the resistant Kaibab Upwarp and the weaker rocks of the Glen Canyon Group. This corresponds to a slowing of incision in the Grand Canyon in the wake of the transient headward incision signal. After rapid incision in the Glen Canyon region begins, rates downstream of Lee's Ferry continue to drop, while the rates

upstream of Lee's Ferry remain high and fairly constant, as the relative baselevel of the reach is controlled by the retreat rate of the knickpoint and the dip of the lithologic contact (each relatively constant).

Because we are only able to measure incision rates that are averaged over some length of time, it is important to understand how the variation in incision rate through time affects the average rate we measure, particularly in complex transient incision scenarios such as that predicted by our modeling. The curves in Figure 12b show the incision rate at each of the points in Figure 11b averaged between different times in the past and today, illustrating how the incision rate one would calculate at a particular point by measuring a feature, such as a fluvial terrace or cave deposit, varies with the age of that feature. The rates within the Grand Canyon region are highly dependent on the timespan over which they are averaged, reflecting the passage of a pulse of rapid incision associated with an upstream migrating knickpoint. The plot shows that, even though the absolute rate at point 3 (just downstream of Lee's Ferry) is near its maximum at the onset of Glen Canyon incision, the averaged rate has already substantially declined.

As even these simple models illustrate, in a real system, with spatial variations such as multiple lithologies and structures, as well as temporal variations such as climatic effects, the incision signal has the potential to become quite complicated. The variations that we see in the form of the knickzone throughout the study region, and the absence of a visible transient signal in the channels of the Henry Mountains highlight the complexity that results in large natural systems such as the Colorado River drainage.

Conclusions

The Colorado River in the Glen Canyon region has experienced a pulse of incision within the past ~500 ky. Tributaries to the Colorado are continuing to adjust to the more rapid incision of the main stem, as transient knickpoints are preserved at similar

elevations in most of the channels. Incision rates measured below the knickpoints are rapid relative to recent incision rates of the Colorado in the Grand Canyon. Additional incision rates are need both upstream and downstream of the knickpoints to corroborate our interpretation of the pattern observed in the channel profiles. Incision rates on Trachyte Creek, in the Henry Mountains, are of a similar magnitude to the rapid rates measured below the knickpoints in nearby channels, despite the absence of knickpoints in Trachyte Creek and many of the Henry Mountains channels. These observations indicate that, upstream of the Grand Canyon, Colorado River is continuing to adjust in a complex way to the drainage integration and large base level fall responsible for the formation of the Grand Canyon.

References

Anderson RS, Repka JL, Dick GS. 1996. Explicit treatment of inheritance in dating depositional surfaces using in situ ^{10}Be and ^{2}6Al. *Geology* **24**: 47–51.

Belmont P, Pazzaglia FJ, Gosse J. 2006. Using the 10-Be Grain Size Dependency in Alluvial Sediments to Investigate Hillslope and Channel Processes. *Eos Trans. AGU*, 87(52), Fall Meet. Suppl., Abstract H21H-06.

Berlin MM, Anderson RS. 2007. Modeling of knickpoint retreat on the Roan Plateau, western Colorado. *Journal of Geophysical Research* **112**: F03S06, doi:10.1029/2006JF000553.

Bierman PR, Nichols KK. 2004. Rock to sediment, Slope to sea with 10-Be, Rates of landscape change. *Annual Reviews of Earth and Planetary Sciences* **32**: 215-255.

Bierman PR, Clapp EM, Nichols KK, Gillespie AR, Caffee M. 2001. Using cosmogenic nuclide measurements in sediments to understand background rates of erosion and sediment transport. In *Landscape Erosion and Evolution Modeling*, Harmon RS, Doe WM (eds). New York; 89-116.

Crosby BT, Whipple KX. 2006. Knickpoint initiation and distribution within fluvial networks: 236 waterfalls in the Waipaoa River, North Island, New Zealand. *Geomorphology* **82**: 16–38.

Crosby BT, Whipple KX, Gasparini NM, Wobus CW. 2007. Formation of fluvial hanging valleys: Theory and simulation. *J. Geophys. Res.* **112**: F03S10. doi:10.1029/2006JF000566.

Damon PE, Shafiqullah M, Leventhal JS. 1974. K-Ar chronology for the San Francisco volcanic field and rate of erosion of the Little Colorado River. In *Geology of northern Arizona, with notes on archaeology and paleoclimate, Part 1, Regional studies*, Karlstrom TNV, Swann GA, Eastwood RL (eds). Geological Society of America Guidebook, Rocky Mountain Section Meeting: Flagstaff; 221–235.

Davis SW, Davis ME, Lucchitta I, Hanks TC, Finkel RC, Caffee M. 2001. Erosional history of the Colorado river through the Glen an Grand Canyons. In *The Colorado River Origin and Evolution: Proceedings of a Symposium Held at Grand Canyon National Monument*, Young RA , Spamer EE (eds). Grand Canyon

Association Monograph 12. Grand Canyon Association: Grand Canyon National Park, Arizona; 135-139.

Dunai TJ. 2000. Scaling factors for production rates of in situ produced cosmogenic nuclides: a critical reevaluation. *Earth and Planetary Science Letters* **176**: 157-169.

Flint JJ. 1974. Stream gradient as a function of order, magnitude, and discharge: Water Resources Research **10**: 969–973.

Garvin CD, Hanks TC, Finkel RC, Heimsath AM. 2005. Episodic incision of the Colorado River in Glen Canyon, Utah. *Earth Surface Processes and Landforms* **30(8)**: 973-984.

Gilbert GK. 1877. *Report on the Geology of the Henry Mountains (Utah)*. United States Geological Survey: Washington, D.C.

Gosse JC, Phillips FM. 2001. Terrestrial in situ cosmogenic nuclides: Theory and application, *Quaternary Science Reviews* 20: 1475–1560.

Granger DE, Kirchner JW, Finkel R. 1996. Spatially averaged long-term erosion rates measured from in situ-produced cosmogenic nuclides in alluvial sediment. *Journal of Geology* **104(3)**: 249-257.

Granger DE, Muzikar PF. 2001. Dating sediment burial with in situ-produced cosmogenic nuclides; theory, techniques, and limitations. *Earth Planet. Sci. Lett.* 188: 269–81.

Hack JT. 1957. Studies of longitudinal stream profiles in Virginia Maryland. *U.S. Geol Surv. Prof. Pap.* 294–B:97.

Hamblin WK. 1994. Late Cenozoic lava dams in the western Grand Canyon: Geological Society of America Memoir 183, 135 p.

Hancock, GS, Anderson RS, Chadwick OA, Finkel RC.1999. Dating terraces with application to the Wind River, Wyoming. *Geomorphology* **27(1-2)**: 41-60. doi:10.1016/S0169-555X(98)00089-0.

Hanks TC, Lucchitta I, Davis SW, Davis ME, Finkel RC, Lefton SA, Garvin CD. 2001. The Colorado River and the age of Glen Canyon. In *The Colorado River Origin and Evolution: Proceedings of a Symposium Held at Grand Canyon National*

Monument, Young RA , Spamer EE (eds). Grand Canyon Association Monograph 12. Grand Canyon Association, Grand Canyon National Park: Arizona; 129-133.

Hanks TC, Webb RH. 2006. Effects of tributary debris on the longitudinal profile of the Colorado River in Grand Canyon. *J. Geophys. Res* **111**, F02020 , doi:10.1029/2004JF000257.

Heimsath AM, Chappell J, Dietrich WE, Nishiizumi K, Finkel RC. 2001. Late Quaternary erosion in southeastern Australia: A field example using cosmogenic nuclides. *Quaternary International* **83–85**: 169-185.

Hintze LF, Willis GC, Laes DYM, Sprinkel DA, Brown KD. 2000. Digital geologic map of Utah: Utah Geological Survey, Department of Natural Resources, in cooperation with United States Geological Survey, Map 179DM, scale 1:500,000.

Hirschberg DM, Pitts GS. 2000. Digital geologic map of Arizona: a digital database derived from the 1983 printing of the Wilson, Moore, and Cooper 1:500,000-scale map: U.S. Geological Survey Open-File Report 00-409, U.S. Geological Survey, Menlo Park, California.

Howard AD, WE Dietrich, Seidl MA. 1994. Modeling fluvial erosion on regional to continental scales. *J. Geophys. Res.* **99**: 13,971– 13,986.

Hunt CB. 1953. *Geology and Geography of the Henry Mountains Region Utah.* Geological Survey Professional Paper 228, 234 p.

Jackson M.1997. Processes of Laccolithic Emplacement in the Southern Henry Mountains, Southeastern Utah. In *Laccolith complexes of southeastern Utah : time of emplacement and tectonic setting : workshop proceedings*, Friedman JD, Huffman AC (eds). U.S. Geological Survey Bulletin 2158: Washington; 51-59.

Johnson JP, Whipple KX, Sklar LS, Hanks TC. Transport slopes, sediment cover and bedrock channel incision in the Henry Mountains, Utah, USA. in review, *JGR-Earth Surface.*

Johnson JP, Farrow J, Whipple K, Sklar L. 2005. Sediment cover and lithologic feedbacks in bedrock channels and canyons. European Geosciences Union meeting abstract, EGU05-A-03848; GM7-1TU4O-004.

Karlstrom KE, Kirby E. 2004. Colorado River System of the Southwestern U.S.: Longitudinal Profiles, Differential Incision, and a Hypothesis for Quaternary Tectonism at Both Ends. GSA *Abstracts with Programs* **36(5)**: 550.

Karlstrom KE. 2005. Influences of Quaternary tectonism on the profile and incision history of the Colorado River system of the southwestern U.S. GSA *Abstracts with Programs* **37(6)**: 15.

Karlstrom KE, Crow RS, Peters L, McIntosh W, Raucci J, Crossey LJ, Umhoefer P, Dunbar N. 2007. 40Ar/39Ar and field studies of Quaternary basalts in Grand Canyon and model for carving Grand Canyon: Quantifying the interaction of river incision and normal faulting across the western edge of the Colorado Plateau. *GSA Bulletin* 119(11/12): 1283–1312, doi: 10.1130B26154.1

Kirkham R, Kunk M, Bryant B, Streufert R. 2001, Constraints on timing of late Cenozoic incision by the Colorado River Glenwood Canyon, CO. In *The Colorado River: Origin and evolution*, Young RA, Spamer EE (eds). Grand Canyon Association Monograph: Grand Canyon, Arizona; 113-116.

Kohl CP, Nishiizumi K. 1992. Chemical isolation of quartz for measurement of in-situ–produced cosmogenic nuclides. *Geochimica et Cosmochimica Acta* **56**: 3583–3587.

Lucchitta, I. 1990. History of the Grand Canyon and of the Colorado River in Arizona. In *Grand Canyon Geology*, Beus, SS, Morales, M (eds). Oxford University Press: New York; 311-332.

Lucchitta I, Curtis GH, Davis ME, Davis SW, Turrin B. 2000. Cyclic aggradation and downcutting, fluvial response to volcanic activity, and calibration of soil-carbonate stages in the western Grand Canyon, Arizona. *Quaternary Research* **53**: 23–33.

Machette, MN.1985. Calcic soils of the southwestern United States. In: Soils and Quaternary Geology of the Southwestern United States 203, Weide DL (ed), Geological Society of America Special Paper, Boulder; 1–21.

Marchetti, D. W., and Cerling, T. E., 2001, Bedrock Incision Rates for the Fremont River, Tributary of the Colorado River, In *The Colorado River Origin and Evolution: Proceedings of a Symposium Held at Grand Canyon National*

Monument, Young RA , Spamer EE (eds). Grand Canyon Association Monograph 12. Grand Canyon Association, Grand Canyon National Park: Arizona; 125-127.

Niemann JD, Gasparini NM, Tucker GE, Bras RL. 2001. A quantitative evaluation of Playfair's law and its use in testing long-term stream erosion models. *Earth Surface Processes and Landforms* **26(12)**: 1317–1332, doi: 10.1002/esp.272.

Pederson J, Karlstrom K, Sharp W, McIntosh W. 2002. Differential incision of the Grand Canyon related to Quaternary faulting—Constraints from U-series and Ar/Ar dating. *Geology* **30**: 739–742.

Pederson JL, Anders MD, Rittenhour TM, Sharp WD, Gosse JC, Karlstrom KE. 2006. Using fill terraces to understand incision rates and evolution of the Colorado River in eastern Grand Canyon, Arizona. . *J. Geophys. Res* **111**, F02003, doi:10.1029/2004JF000201.

Pederson J, Callahan C, Roy M. 2007. The central Colorado Plateau bullseye – linking patterns of quantified incision, exhumation, and flexure. Geological Society of America *Abstracts with Programs* **39(6)**: 184.

Perg LA, Anderson RS, Finkel RC. 2001. Use of a new 10Be and 26Al inventory method to date marine terraces, Santa Cruz, California, USA. *Geology* **29(10)**: 879–882.

Polyak V, Hill C, Asmerom Y. 2008. Age and Evolution of the Grand Canyon Revealed by U-Pb Dating of Water Table–Type Speleothems. Science **319**: 1377-1380.

Repka JL, Anderson RS, Finkel RC. 1997. Cosmogenic dating of fluvial terraces, Fremont River, Utah. *Earth Planet. Sci. Lett.* **152**: 59–73.

Sandoval M, Karlstrom KE, Asla, A, Kirby E, Granger D. 2006. Incision History of the Black Canyon of the Gunnison. *Eos Trans. AG,* **87(52)**, Fall Meet. Suppl., Abstract T11A-0421.

Schoenbohm LM, Whipple KX, Burchfiel BC, Chen L. 2004. Geomorphic constraints on surface uplift, exhumation, and plateau growth in the Red River region, Yunnan Province, China.: *Geological Society of America Bulletin* **116**: 895–909.

Sklar L. 2003. *The influence of grain size, sediment supply, and rock strength on rates of river incision into bedrock.* PhD thesis. Univ. Calif., Berkeley. 343 pp.

Stock GM, Anderson RS, Finkel RC. 2004. Pace of landscape evolution in the Sierra Nevada, California, revealed by cosmogenic dating of cave sediments. Geology **32**: 193-196.

Stone JO. 2000. Air pressure and cosmogenic isotope production. *J.Geophys. Res.* **105(B10)**: 23753–23759.

Tucker GE, Bras RL. 2000. A stochastic approach to modeling the role of rainfall variability in drainage basin evolution. *Water Resources Research* **36**(7): 1953–1964.

Tucker GE. 2004. Drainage basin sensitivity to tectonic and climatic forcing; implications of a stochastic model for the role of entrainment and erosion thresholds. *Earth Surface Processes and Landforms* **29**: 185–205.

Webb RH, Griffiths PG, Fleming JB, Callegary JB, Fenton CR, Hanks TC. 2004. The Longitudinal Profile of the Colorado River on the Colorado Plateau: How Deep is Alluvium Beneath the River?. Geological Society of America *Abstracts with Programs*, **36(5)**: 550.

Whipple KX, Tucker GE. 1999. Dynamics of the stream-power river incision model; implications for height limits of mountain ranges, landscape response timescales, and research needs, *Journal of Geophysical Research, Solid Earth* **104(B8)**: 17,661–17,674.

Whipple KX, Tucker GE. 2002. Implications of sediment-flux dependent river incision models for landscape evolution. *J. Geophys. Res.* **107(B2)**: 2039, doi:10.1029/2000JB000044.

Whipple KX. 2004. Bedrock rivers and the geomorphology of active orogens. *Annu. Rev. Earth Planet. Sci.* **32:** 151–185.

Wobus C, Whipple K, Kirby E, Snyder N, Johnson J, Spyropolou K, Crosby BT, Sheehan D. 2006. Tectonics from topography: Procedures, promise and pitfalls. In *Tectonics, Climate and Landscape Evolution*, Willett SD, Hovius N, Brandon MT, Fisher
DM (eds), Geol. Soc. Am. Spec. Pap. 398, 55– 74.

Wolkowinsky AJ, Granger DE. 2004. Early Pleistocene incision of the San Juan River, Utah, dated with ^{26}Al and ^{10}Be. *Geology* **32 (9)**: 749-752.

Figure Captions

Figure 1

Overview of the studied portion of the Colorado River system and the surrounding region (inset). Highlighted and labeled tributaries indicate drainages for which long profiles were analyzed. Red circles mark the upstream extent of the steep reach on each tributary and correspond to the knickpoints shown in the channel profiles above. The circle on the Colorado marks the large knickpoint at Cataract Canyon. Gray circles mark the upper knickpoints on Muddy Creek and the Fremont River. The locations of existing incision rate estimates are indicated with stars; numbers correspond to location numbers in Table 1 and in the text, orange indicates a fast rate (greater than ~500 m/m.y.), yellow a medium (between 200 and 500 m/m.y.), and white a slow rate (less than 150 m/m.y.). The black box indicates the location of the Henry Mountains pediment map.

Figure 2

Longitudinal profiles of channels entering the Colorado River between the upper Grand Canyon and Cataract Canyon, obtained using 90 m USGS DEMs. The dashed gray line represents a manually surveyed profile of the Colorado River (1924 USGS river survey, B. Webb, T. Hanks pers. comm.) . The gray dots and dashed black lines are channel positions obtained from USGS contour maps showing bathymetry of Lake Powell. The circles mark the beginning of the steep reach in each channel, and correspond to the knickpoints shown on the maps. The stars mark the locations of selected incision rate estimates, corresponding to the numbered stars in the overview map. The profiles of the San Juan and Little Colorado Rivers have been truncated and locations 5 and 6 are not shown for clarity.

Figure 3

Paria River example of long profile fitting method. We fit concavity and steepness indices to the upper part of the profile, then extrapolate the fit downstream and measure the difference between the expected elevation and the actual elevation of the channel where it enters the Colorado.

Figure 4

A) Geologic map of northern Utah and Southern Arizona, illustrating the location of the knickpoints relative to lithologic boundaries. Black boxes show the locations of Figures 4b and 6. Locations of selected incision rate estimates are marked; locations 7, 10, and 11 are off the map. Geology from USGS digital geologic maps of Utah (Hintze et al. 2000) and Arizona (Hirschberg et al., 2000). B) Close-up of the geology near the knickpoint on Last Chance Creek. Qa: Quaternary, alluvium/colluvium; Qao: Quaternary, older alluvium/colluvium; Qe: Quaternary, eolian deposits; K2: Cretaceous, Wahweap Ss, Straight Cliffs Fm; K1: Cretaceous, Tropic Shale, Dakota Ss; J2: Jurassic, Morrison Fm; J1: Jurassic, Summerville Fm, Entrada Ss; Jg: Jurassic, Glen Canyon Group.

Figure 5

Map of local relief calculated over a circular 1.5 km radius moving window. Many of the knickpoints correspond to an increase in local relief near the channel.

Figure 6

Map of the distribution and inferred relative ages of pediments in the Henry Mountains. Pediments decrease in age from L0 to L9. Mapping is based on aerial photographs and field observations. The blue line marks Trachyte Creek, and the black box shows the location of the studied terraces. The terrace levels defined locally in our sturdy area correspond as follows: P1 corresponds to level L5, P2 to L6, and P3 to L9; P4 is too small in extent and too close to the channel in elevation to map at this scale.

Figure 7

A) Aerial view of studied surfaces. B) Schematic cross section of Trachyte Creek surfaces. Scale is approximate. C) Panoramic view of Trachyte Creek surfaces. D) The

P3 gravel deposit where the depth profile samples were collected. Tape measure is 1.7 m long.

Figure 8

The P3 depth profile. A linear fit to depth-corrected production rate vs. concentration suggests an exposure age of about 13 k.y. and an inherited concentration that is equivalent to approximately 7 k.y. of exposure.

Figure 9

The P4 profile indicates a complicated exposure history or distribution of inherited nuclides, as concentration does not uniformly decrease with depth. The low concentration in the bedrock sample suggests a very young age for terrace formation.

Figure 10

The age of each surface plotted against the amount of subsequent downcutting. Gray bars indicate predicted age ranges based on pedogenic carbonate development in the gravels. Dashed gray lines have slopes of 300 m/m.y. and 500 m/m.y. for comparison.

Figure 11

Numerical models of the evolution of a detachment-limited channel profile in response to a sudden base-level fall. The solid black line is the initial channel profile, and the dashed gray lines show how the profile evolves through time. In both models the background uplift rate is 100 m/m.y. A) Evolution of a channel in flat-lying two-layer bedrock – above 130 m elevation, the bedrock is 5 times weaker (more erodable) than below 130 m. The channel experiences a sudden base-level fall of 200 m at the initiation of the model run. The dashed black line shows the profile after the upper knickpoint has swept through much of the system. Diffusion of the knickpoints is an artifact of the numerical model. This may be analogous to the Dirty Devil River. B) Evolution of a channel in dipping bedrock. Setup is analogous to the Colorado River in the Grand Canyon region. The strong rocks of the Kaibab uplift dip under the Glen Canyon Group near Lee's Ferry, then resurface farther upstream. The channel experiences a sudden 650 m base-level fall at the

initiation of the model run, simulating Colorado River diversion or integration across the Grand Wash Cliffs. The dashed black line is analogous to the modern Colorado River. See text for further discussion. C) Manually surveyed profile of the Colorado River for comparison (1924 USGS river survey, B. Webb, T. Hanks pers. comm.). Simplified lithologic boundaries adapted from Karlstrom (2005).

Figure 12

A) Incision rates with time for the Colorado River incision model. Each numbered curve shows the incision rate at the corresponding point marked in Figure 11B. The rates include a background uplift and incision rate of 100 m/m.y. B) Rates at each point averaged between present and different times in the past. This is analogous to the rate one would estimate from the height of a terrace of a given age above the modern channel. Note that the maximum averaged rate is offset from the actual maximum rate in a manner that varies with position along the river profile.

Table 1

Location	Incsion Rate (m/m.y.)	Approximate Time Period (ka)	Source
1. Trachyte Creek	350 ± 30 to 540 ± 20	270 - present	This study
2. Glen Canyon	700 ± 120; 830 ± 190	240 - present	Garvin et al., 2005
2. Glen Canyon - Oak Island - 4103 surface	420 ± 150	460 - 240	Garvin et al., 2005
2. Glen Canyon - Rainbow Bridge Canyon	500 ± 110; 600 ± 140	120- present	Garvin et al., 2005
2. Glen Canyon - Navajo Mountain	~500	500 - present	Hanks et al., 2004
3. Lake Powell - Bullfrog	418 ± 11	480 - present	Davis et al., 2004
4. Lees Ferry	~250	100 - present	Lucchitta et al., 2000
5. Fremont River - Carcass Creek/Johnson Mesa	380 to 470	200 - present	Marchetti and Cerling, 2004
6. Fremont River - Caineville	300 to 850	150 - present	Repka et al., 1997
7. San Juan River - Bluff	110 ± 14	1360 - present	Wolkowinsky and Granger, 2004
8. upper Little Colorado	103 ± 17	510 - present	Damon, 1974
8. upper Little Colorado	90 ± 12	240 - present	Damon, 1974
9. eastern Grand Canyon	135 ± 17; 144 ± 18	340,280 - present	Pederson et al., 2006
10. Grand Canyon - upstream of Toroweap Fault	133 ± 16	350 - present	Pederson et al., 2002
11. Grand Canyon - downstream of Toroweap Fault	72 to 92	510 - present	Pederson et al., 2002

Table 2

Tributary	step length (km)	step height (m)	Step elevation (m)
Little Colorado	75	386	1247
Paria	32	156	1258
Last Chance	35	189	1375
San Juan	165	150	1293
Escalante	59	147	1356
Bullfrog Creek	n/a	n/a	n/a
Trachyte Creek	n/a	n/a	n/a
White Canyon	22	182	1340
Fremont/Dirty Devil River	40	113	1204
Dark Canyon	39	769	2037

Table 4

Surface	Age (k.y.)	Height (m)	Incision rate (m/m.y.)	±
P1	267	110	412	21.4
P2	178	62	348	28.3
P3	13	7	527	8.4
P4	~3?	1	~330?	19.2

Table 3

Sample ID	altitude (m)	latitude	depth (cm)	production rate$_a$	±$_b$	^{10}Be (atoms/gm quartz)	±	age (k.y.)	±
P2S1	1548	37.96	0	15.42	0.77	2.74E+06	6.24E+04	177.9	7.85
P2S2	1548	37.96	0	15.42	0.77	2.45E+06	5.15E+04	158.6	7.66
P2S3	1548	37.96	0	15.42	0.77	2.53E+06	5.90E+04	164.1	12.19
P1s6	1600	37.95	0	16.05	0.80	3.29E+06	6.30E+04	205.0	6.67
P1s4	1600	37.95	0	16.05	0.80	3.52E+06	6.15E+04	219.1	8.09
P1s7	1600	37.95	0	16.05	0.80	4.29E+06	9.79E+04	267.1	7.65
P4asurf	1451	37.96	0	14.30	0.71	1.41E+05	4.15E+03		
P4a2	1451	37.96	30	8.52	1.19	1.37E+05	4.67E+03		
P4a3	1451	37.96	56	5.44	0.51	1.16E+05	2.84E+03		
P4a4	1451	37.96	88	3.14	0.30	2.39E+05	5.71E+03		
P4aBr	1451	37.96	124	1.69	0.13	1.01E+04	1.57E+03		
P3asurf	1499	37.96	0	14.84	0.74	3.09E+05	5.76E+03		
P3a0	1499	37.96	15	11.46	1.81	2.22E+05	5.73E+03		
P3a1	1499	37.96	50	6.27	0.87	1.36E+05	4.85E+03		
P3a2	1499	37.96	85	3.43	0.84	1.90E+05	5.26E+03		
P3a3	1499	37.96	120	1.88	0.28	1.28E+05	4.67E+03		
P3a4	1499	37.96	165	0.86	0.13	1.22E+05	2.46E+03		
HmTc1$_c$	1444	37.96	0	14.22	0.71	8.46E+04	2.47E+03	5.92	0.46

a) We use the surface production rate of Stone (2000), corrected for altitude and latitude using Dunai (2000).
b) Includes 5% error in surface production rate plus an uncertainty arising from an estimated depth range for each sample
c) Sample of modern sediment from Trachyte Creek

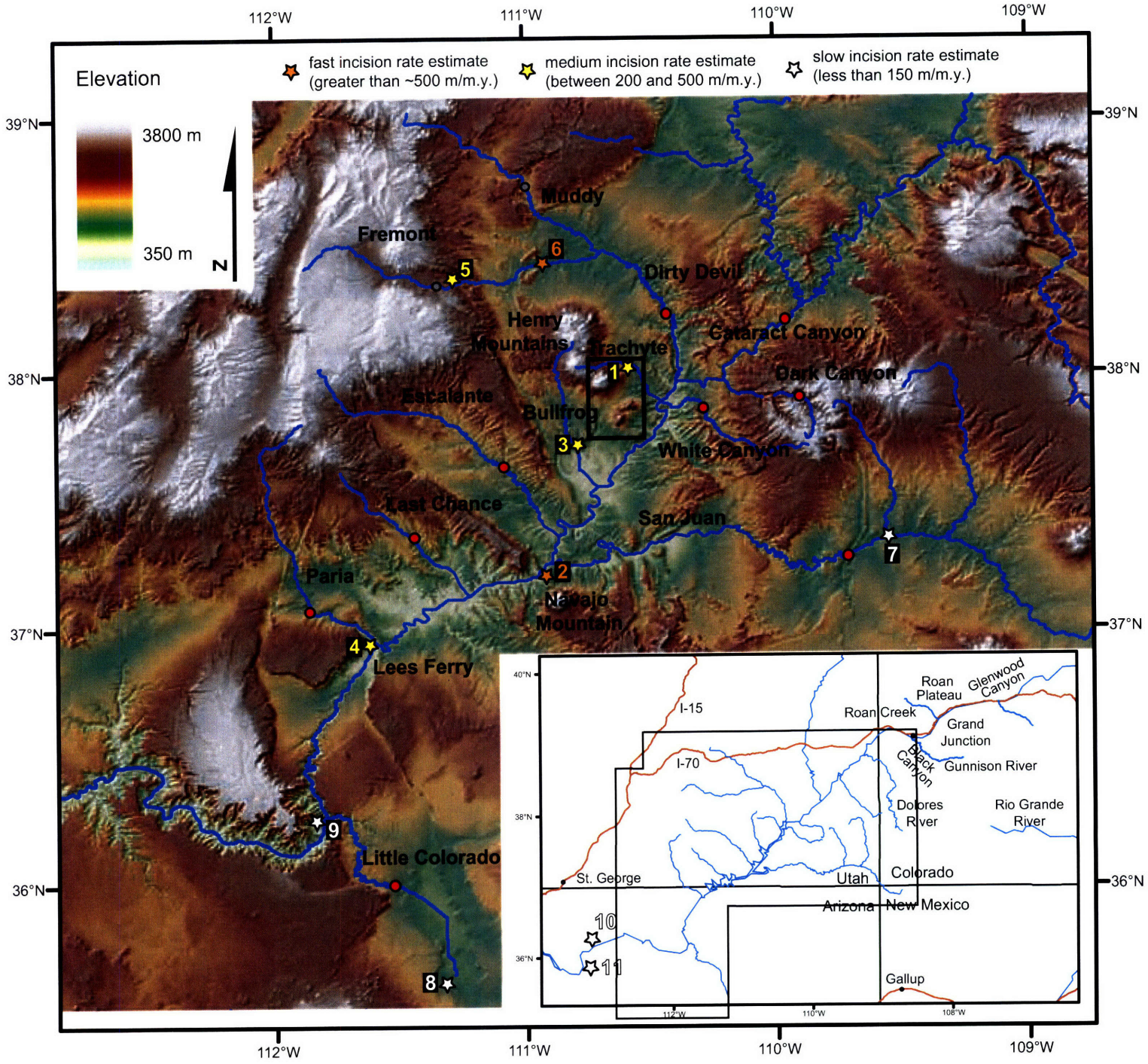
Elevation
3800 m
350 m
N
fast incision rate estimate (greater than ~500 m/m.y.)
medium incision rate estimate (between 200 and 500 m/m.y.)
slow incision rate estimate (less than 150 m/m.y.)
112°W
111°W
110°W
109°W
39°N
38°N
37°N
36°N
Muddy
Fremont
Dirty Devil
Henry Mountains
Trachyte
Cataract Canyon
Dark Canyon
Escalante
Bullfrog
White Canyon
Last Chance
San Juan
Paria
Navajo Mountain
Lees Ferry
Little Colorado
1
2
3
4
5
6
7
8
9
10
11
I-15
I-70
Roan Plateau
Glenwood Canyon
Roan Creek
Grand Junction
Black Canyon
Gunnison River
Dolores River
Rio Grande River
St. George
Utah
Colorado
Arizona
New Mexico
Gallup
40°N
38°N
36°N
112°W
110°W
108°W

Figure 1

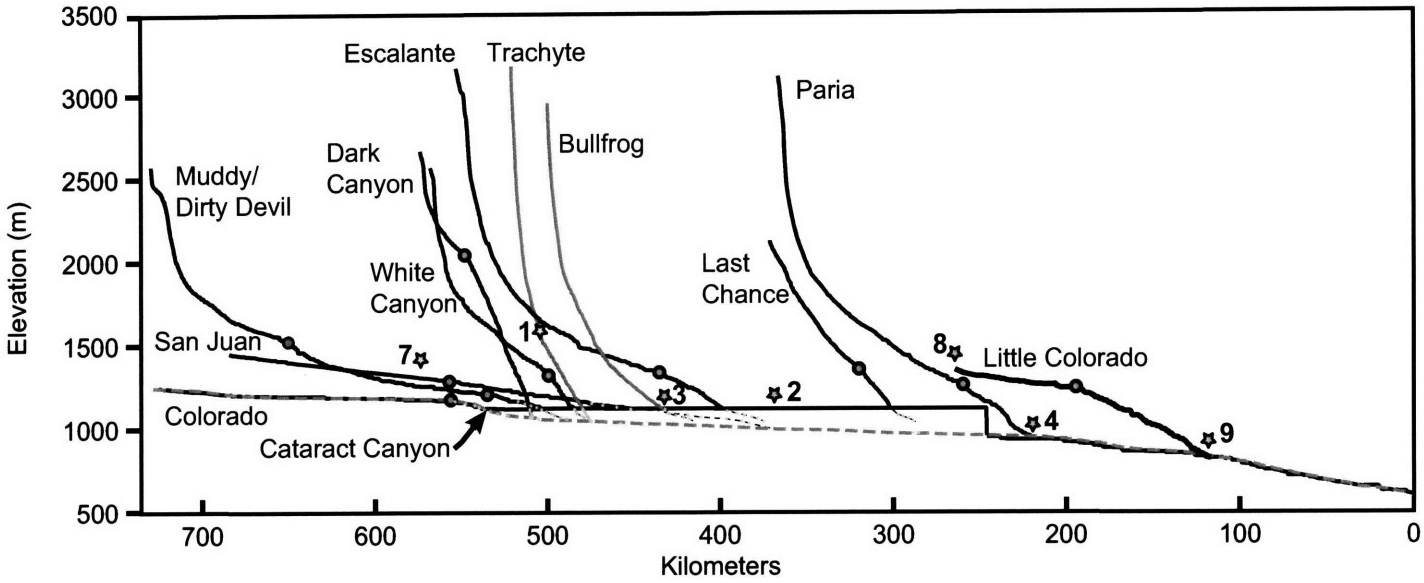
3500
3000
2500
2000
1500
1000
500
Elevation (m)
700
600
500
400
300
200
100
0
Kilometers
Escalante
Trachyte
Paria
Bullfrog
Dark
Canyon
Muddy/
Dirty Devil
White
Canyon
Last
Chance
San Juan
Little Colorado
Colorado
Cataract Canyon
1
2
3
4
7
8
9

Figure 2

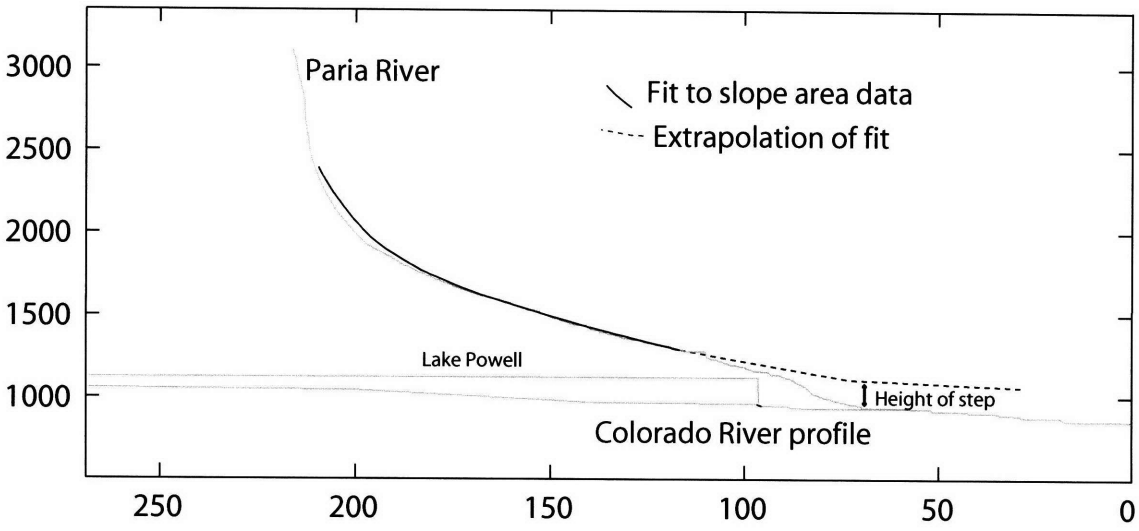
3000
2500
2000
1500
1000
250
200
150
100
50
0
Paria River
Fit to slope area data
Extrapolation of fit
Lake Powell
Height of step
Colorado River profile

Figure 3

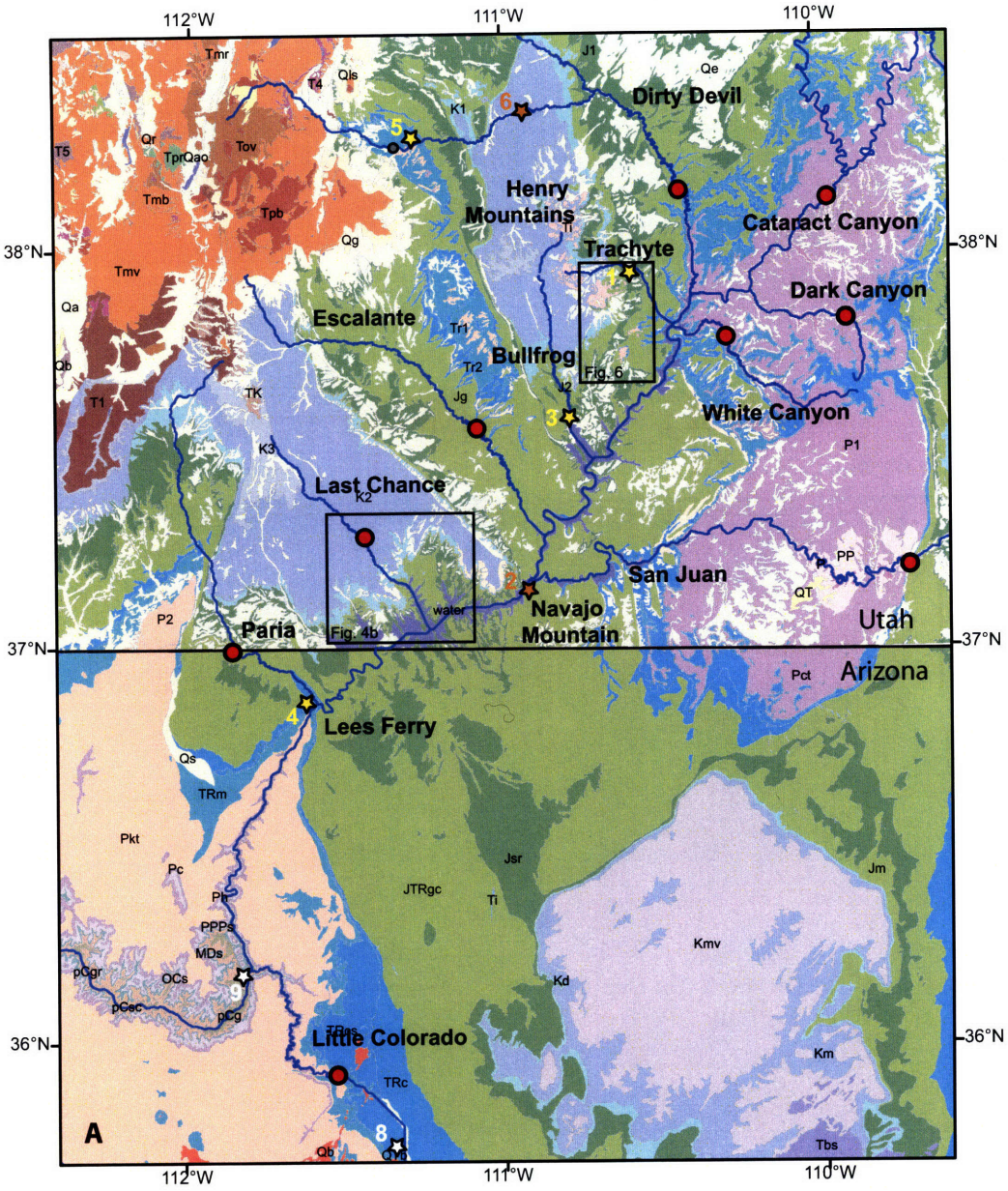
112°W
111°W
110°W
38°N
37°N
36°N
Dirty Devil
Henry Mountains
Cataract Canyon
Trachyte
Dark Canyon
Escalante
Bullfrog
White Canyon
Last Chance
San Juan
Navajo Mountain
Utah
Arizona
Paria
Lees Ferry
Little Colorado
Fig. 4b
Fig. 6
water
A
Tmr
Qls
T4
K1
J1
Qe
T5
Qr
TprQao
Tov
Tmb
Tpb
Qg
Tmv
Qa
Qb
T1
TK
K3
K2
Tr1
Tr2
Jg
J2
P1
PP
QT
P2
Pct
Qs
TRm
Pkt
Pc
Pb
PPPs
MDs
pCgr
OCs
pCec
pCg
TRgs
TRc
Qb
Jsr
JTRgc
Ti
Jm
Kmv
Kd
Km
Tbs
1
2
3
4
5
6
8
9

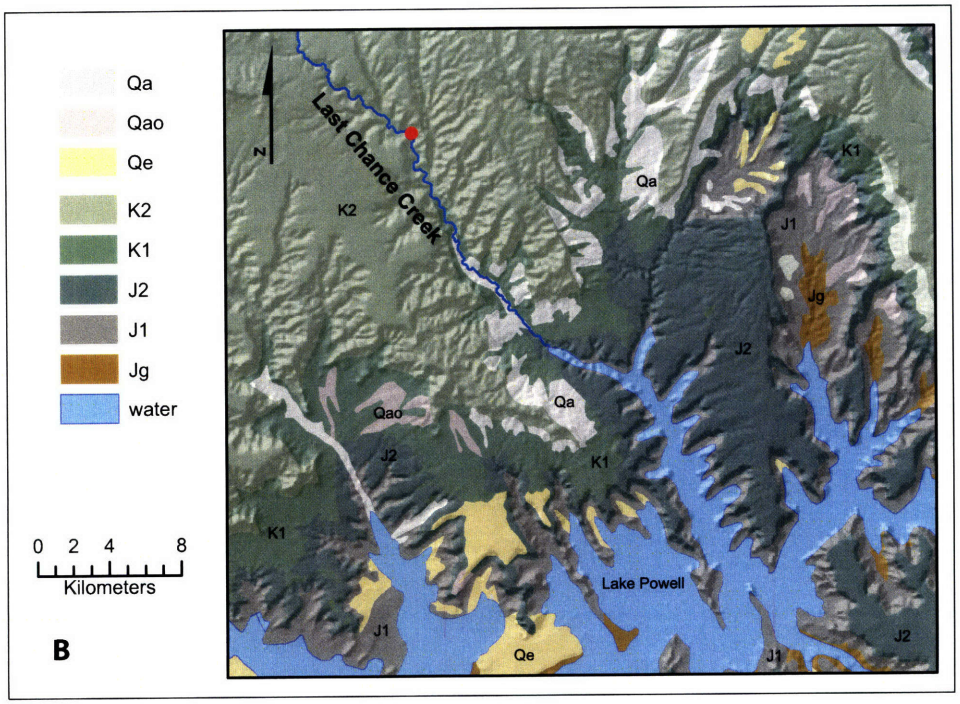
Qa
Qao
Qe
K2
K1
J2
J1
Jg
water
0 2 4 8
Kilometers
B
N
Last Chance Creek
Lake Powell

Figure 4

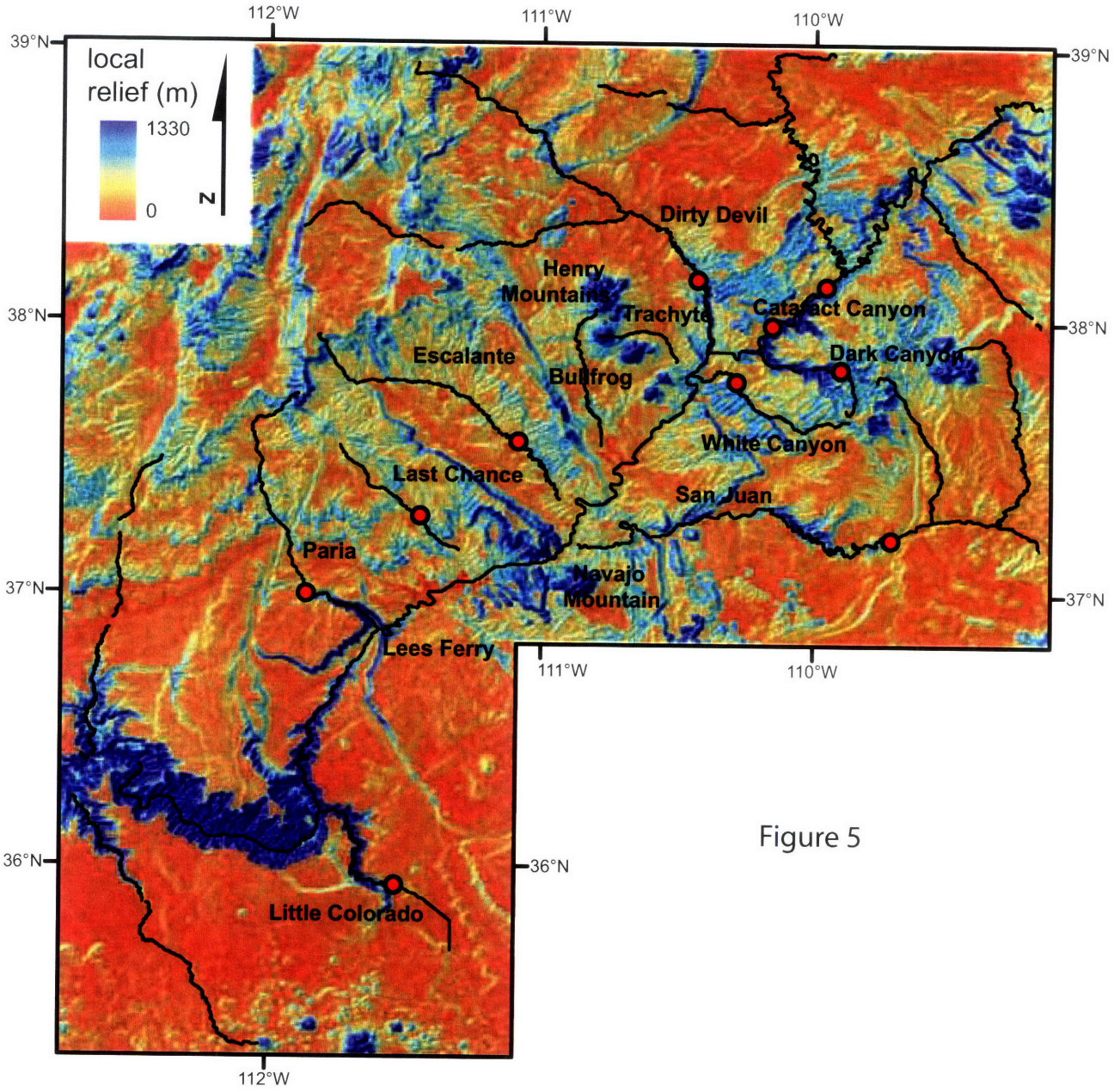
112°W
111°W
110°W
39°N
38°N
37°N
36°N
local
relief (m)
1330
0
N
Dirty Devil
Henry
Mountains
Trachyte
Cataract Canyon
Dark Canyon
Escalante
Bullfrog
White Canyon
Last Chance
San Juan
Paria
Navajo
Mountain
Lees Ferry
Little Colorado

Figure 5

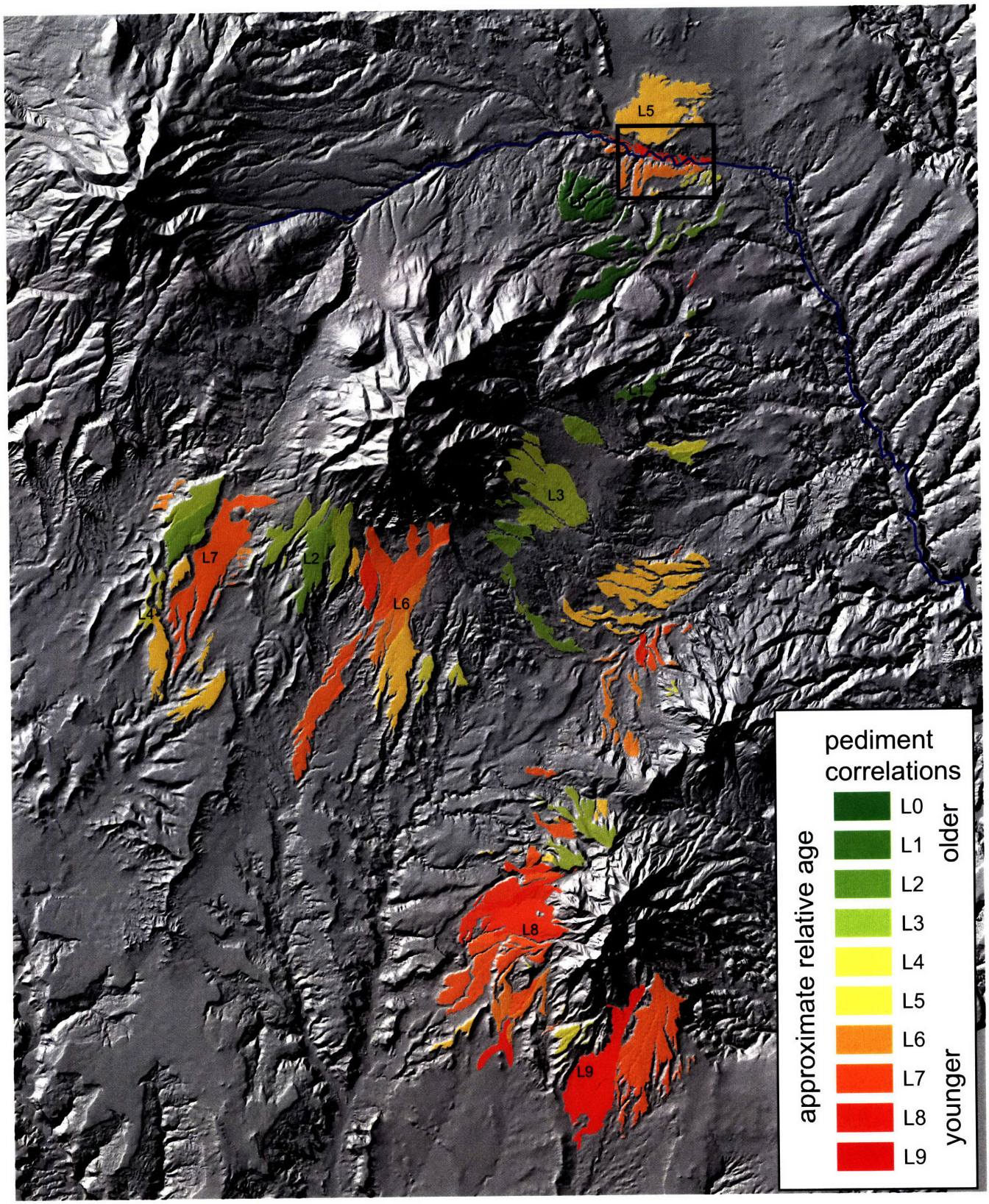
L5
L3
L7
L2
L4
L6
L8
L9
pediment correlations
approximate relative age
older
younger
L0
L1
L2
L3
L4
L5
L6
L7
L8
L9

Figure 6

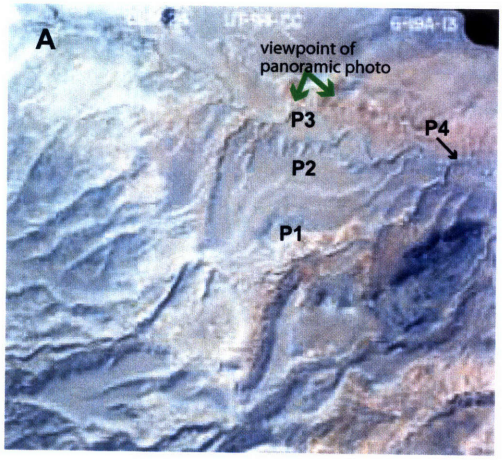
A
viewpoint of
panoramic photo
P3
P4
P2
P1

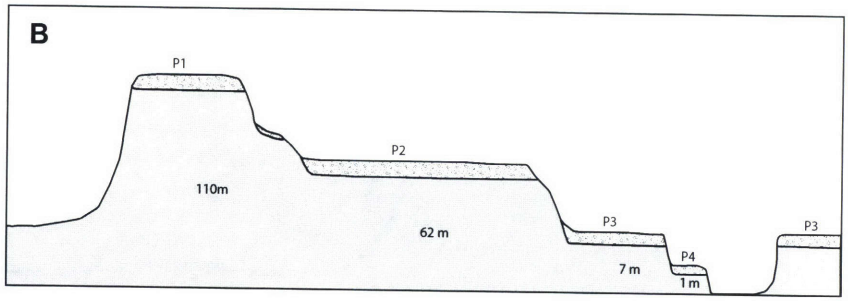
B
P1
P2
110m
62 m
P3
7 m
P4
1 m
P3

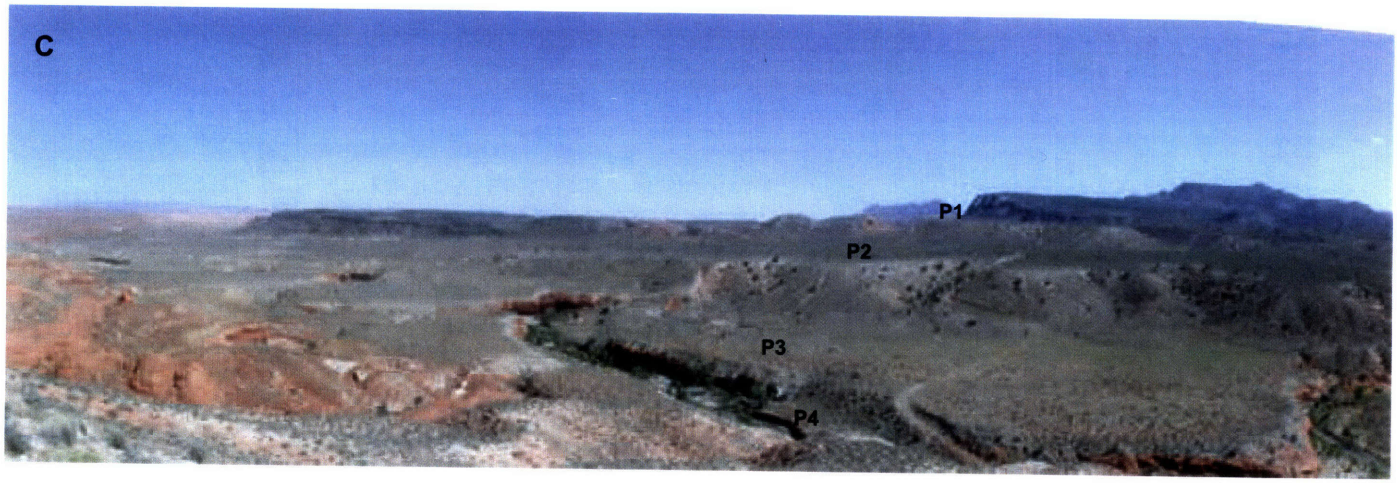
C
P1
P2
P3
P4


D

Figure 7

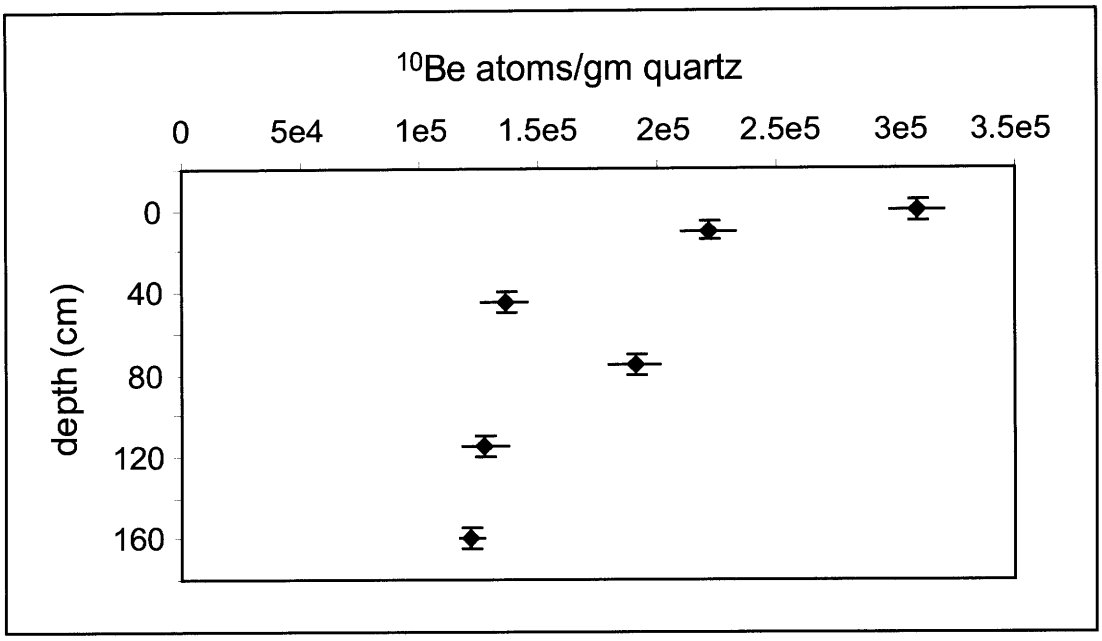
^{10}Be atoms/gm quartz
0
5e4
1e5
1.5e5
2e5
2.5e5
3e5
3.5e5
depth (cm)
0
40
80
120
160

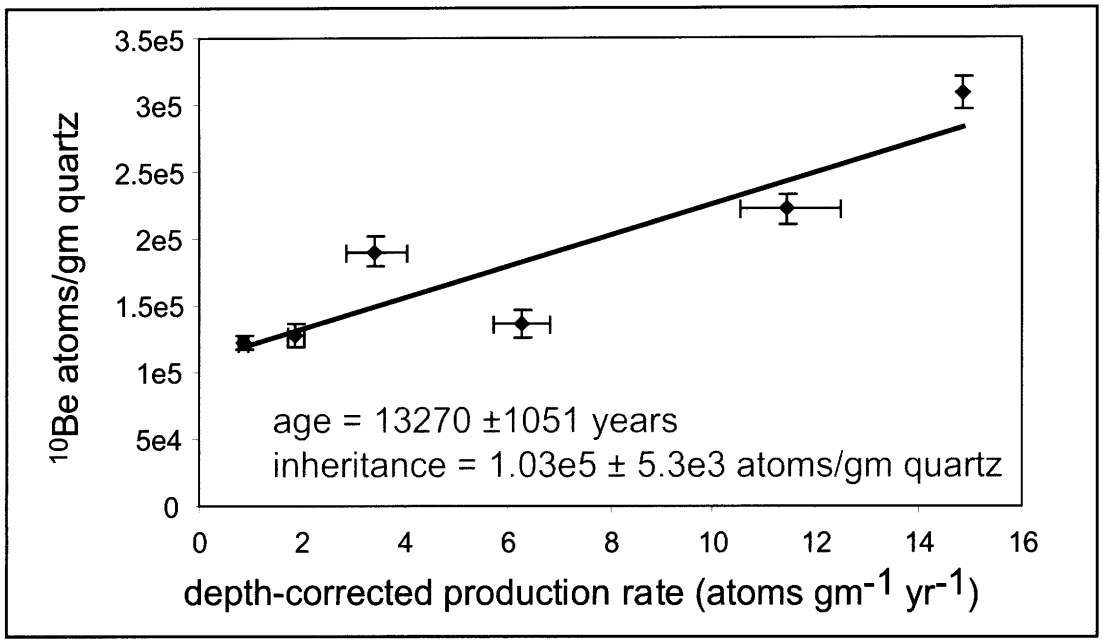
^{10}Be atoms/gm quartz
3.5e5
3e5
2.5e5
2e5
1.5e5
1e5
5e4
0
age = 13270 ±1051 years
inheritance = 1.03e5 ± 5.3e3 atoms/gm quartz
0
2
4
6
8
10
12
14
16
depth-corrected production rate (atoms gm^{-1} yr^{-1})

Figure 8

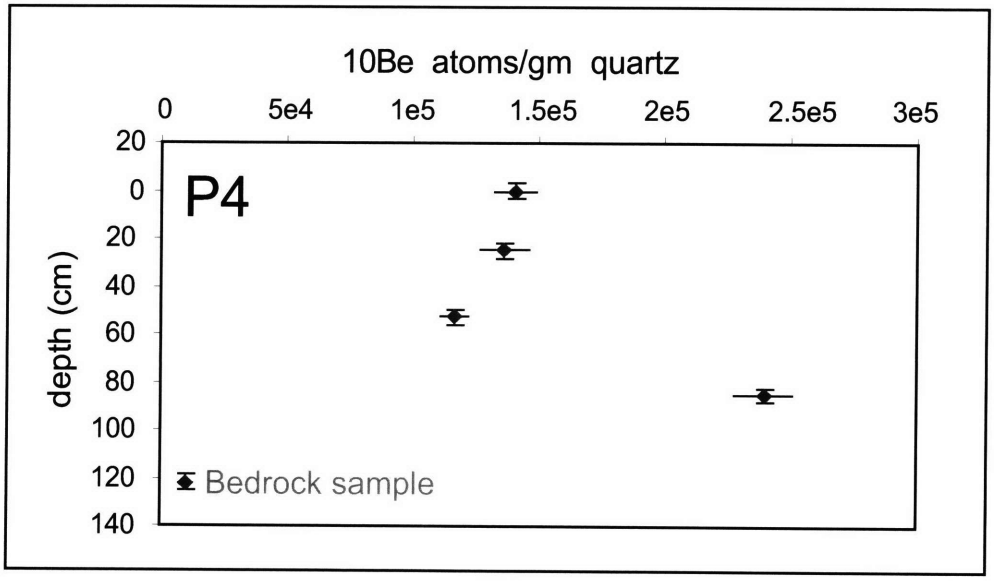
10Be atoms/gm quartz
0
5e4
1e5
1.5e5
2e5
2.5e5
3e5
depth (cm)
20
0
20
40
60
80
100
120
140
P4
Bedrock sample

Figure 9

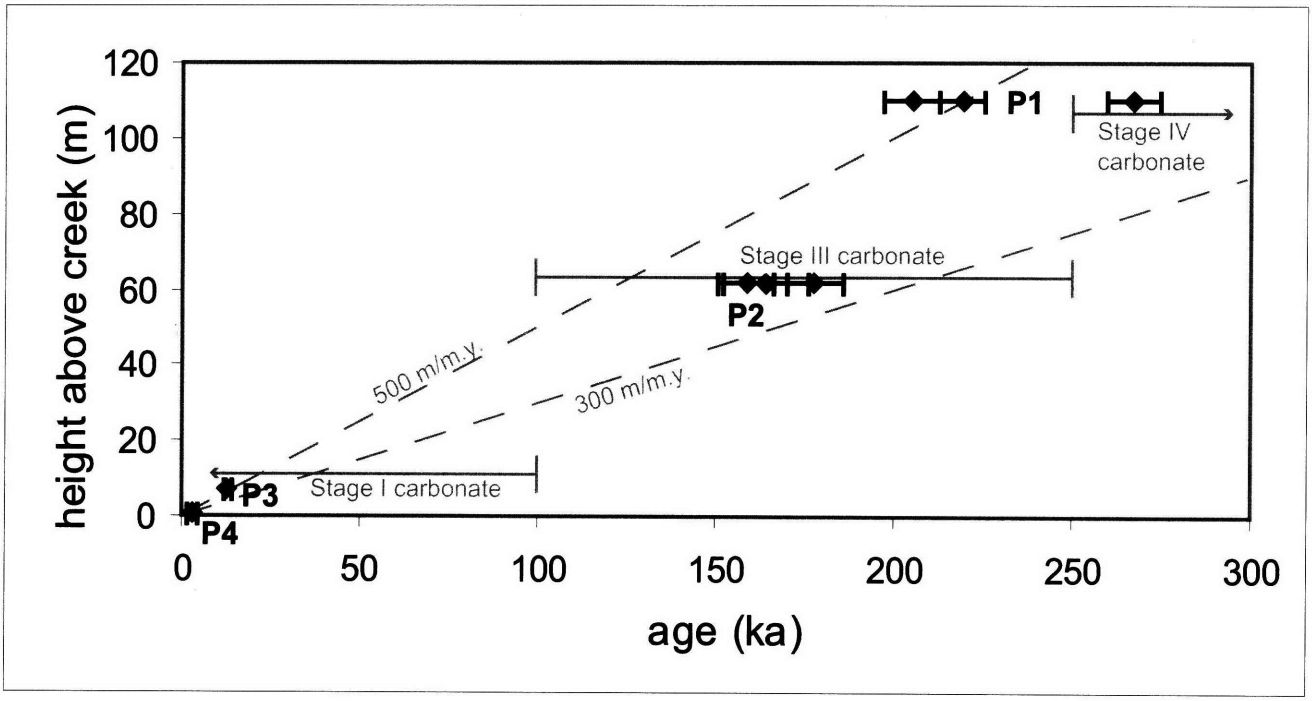
height above creek (m)
120
100
80
60
40
20
0
0
50
100
150
200
250
300
age (ka)
P1
Stage IV
carbonate
Stage III carbonate
P2
500 m/m.y.
300 m/m.y.
P3
Stage I carbonate
P4

Figure 10

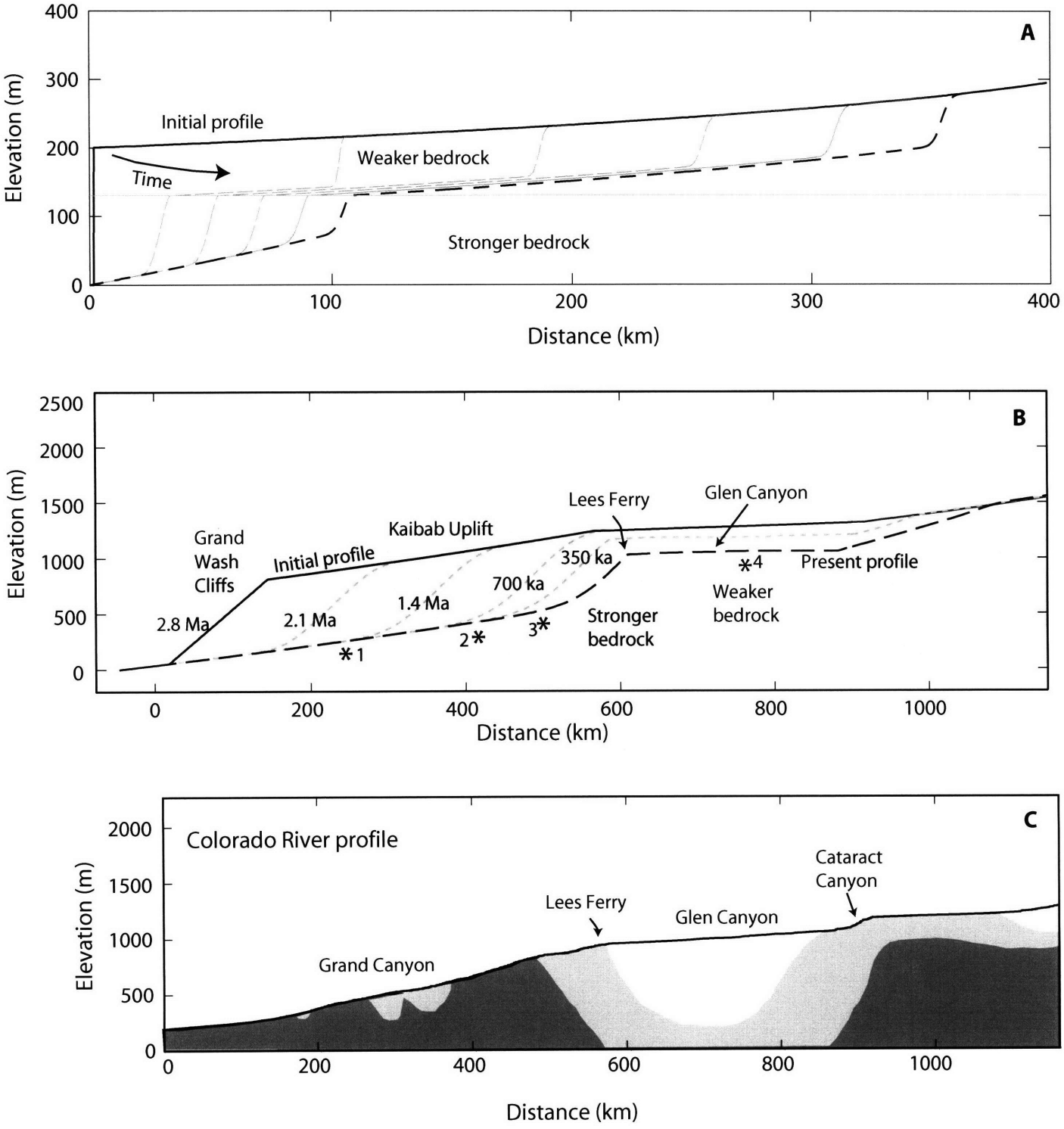
A
Elevation (m)
Distance (km)
Initial profile
Weaker bedrock
Time
Stronger bedrock
B
Grand
Wash
Cliffs
Initial profile
Kaibab Uplift
Lees Ferry
Glen Canyon
2.8 Ma
2.1 Ma
1.4 Ma
700 ka
350 ka
*1
2*
3*
*4
Present profile
Weaker
bedrock
Stronger
bedrock
C
Colorado River profile
Cataract
Canyon
Lees Ferry
Glen Canyon
Grand Canyon

Figure 11

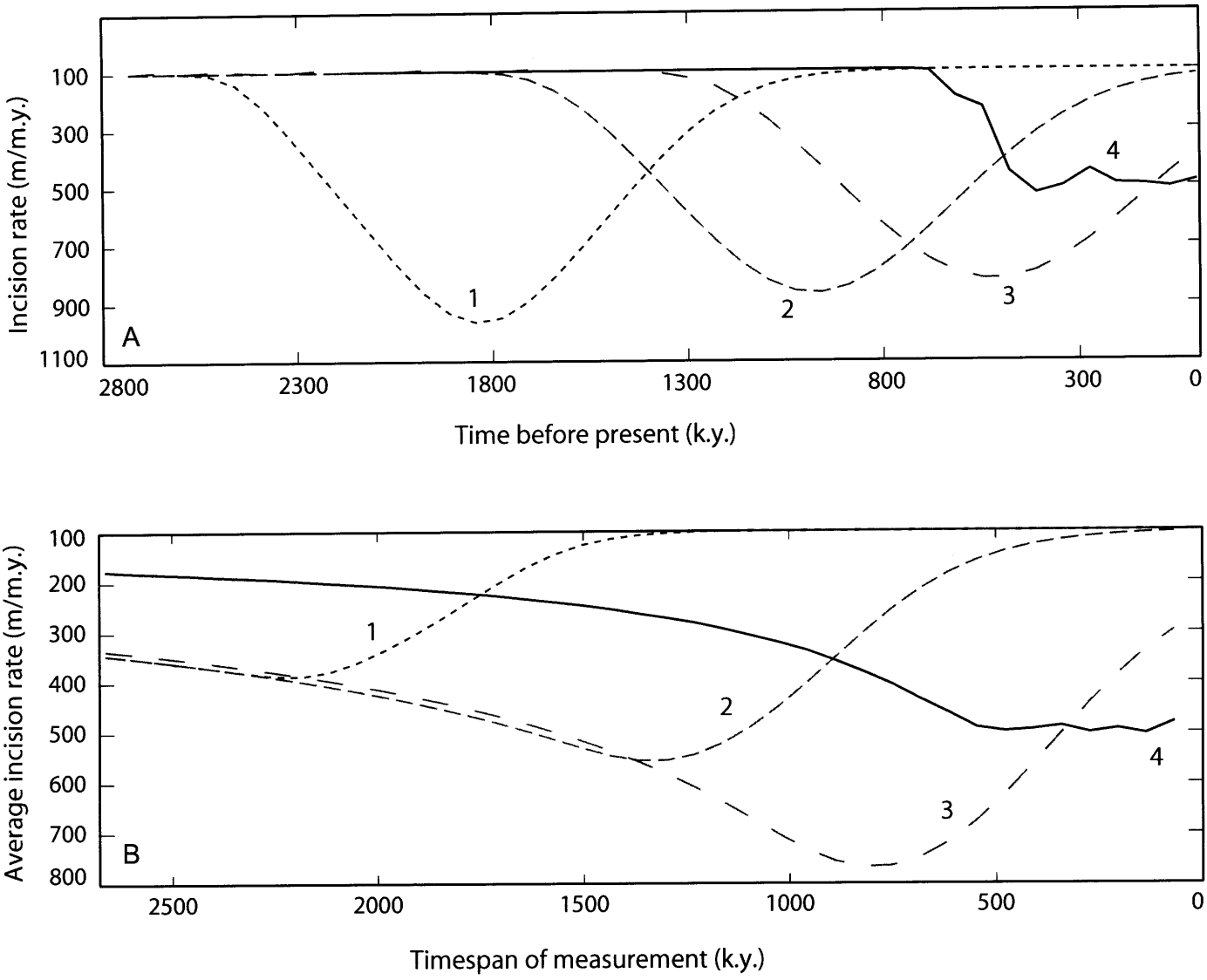
Incision rate (m/m.y.)
100
300
500
700
900
1100
A
1
2
3
4
2800
2300
1800
1300
800
300
0
Time before present (k.y.)
Average incision rate (m/m.y.)
100
200
300
400
500
600
700
800
B
1
2
3
4
2500
2000
1500
1000
500
0
Timespan of measurement (k.y.)

Figure 12

Chapter 6

Summary

The preceding chapters explore several of the many factors that influence continental deformation and the evolution of continental plateaus. In chapter 2 we see that preexisting variations in crustal strength are an important factor affecting the morphology of plateau margins, the localization of deformation, and the pace of plateau propagation. Chapter 3 illustrates how the influence of subduction dynamics and slab dip on mantle temperatures affects the deformation in the overriding crust. In chapter 4, we see an example of deformation in response to a combination of collisional tectonics and the effects of far-field subduction zone dynamics. Chapter 5 addresses the erosion of continental plateaus, and the effect of lithologic variations on the incision of major river systems. Although the studies presented in this thesis address a range of processes and tectonic settings, several common themes emerge between them.

Chapters two and three both explore the role of lower crustal flow in plateau development. In the Tibetan Plateau, preexisting lateral variations in crustal strength play a fundamental role in shaping plateau morphology, while in the Andes, subduction dynamics and the geometry of the subducting slab drive variations in both shortening and crustal strength. These studies illustrate that ductile flow in the middle to lower crust can have a significant effect on the distribution of material throughout a plateau, and that this flux of material in the lower crust may not be reflected in the geology on the surface. The potential for decoupling between deformation on the surface and deformation in the

lower crust and mantle is important to recognize when interpreting geologic observations. Processes in the lower crust can only be inferred indirectly from geophysical data or from studies of exhumed orogens that are assumed to be analogous. Modeling studies such as those presented in chapters two and three predict relationships between lower crustal processes and observable features of orogens, and may allow us to more confidently predict the effect of lower crustal rheology on characteristics that we cannot study directly, such as strain in the lower crust and uplift history.

Chapters two, four, and five address the importance of preexisting heterogeneities in partitioning continental deformation and surface processes. While chapter two focuses on large-scale crustal strength variations, and chapter five shows how lithologic variation can affect river incision, chapter four touches on the influence of preexisting structures. The extensional faults described in chapter four are parallel to and appear to reactivate older zones of shortening. The Cenozoic reactivation of older structures is a common feature of deformation in eastern Tibet, particularly in the Longmen Shan region, where some Mesozoic thrust faults show evidence for multiple episodes of Cenozoic slip in different directions. The reactivation of these faults at the boundary of the Sichuan Basin, as well as the Altyn Tagh at the boundary of the Tarim Basin can be related to both the existence of earlier structures and the presence of large-scale crustal heterogeneities below the Sichuan and Tarim Basins. The recognition of the role of preexisting heterogeneities is particularly important in modeling of continental deformation. Continental crust is often not homogeneous, and in regions such as the Tibetan Plateau that have experienced repeated episodes of deformation the resulting heterogeneity can fundamentally influence future deformation.

Chapters two and three both highlight the importance of a three dimensional evaluation of continental plateaus. In both the Tibetan Plateau and the Altiplano, there may have been a significant flux of material perpendicular to the direction of convergence. In the Tibetan Plateau, chapter two shows how extension in the central plateau may have been triggered by the uplift of the eastern margin, an event far outside the plane of a typical two-dimensional cross-section.

Chapters three and four touch on effects of subduction zone dynamics on continental deformation. The dip of the subducting slab and its effect on temperature and deformation in the lower crust are a primary focus of chapter three. The advancing of the subduction zone between the Nazca and South American Plates, and its role in driving deformation in the Andes is also a fundamental aspect of the modeling in chapter three. Chapter four suggests that retreating subduction far from the India-Asia collision zone may have played a role in the initiation of eastward extrusion and deformation in the Danba region.

The studies presented in this thesis illustrate the importance of taking into account factors such as heterogeneity, three-dimensionality, and far-field influences in the study of continental deformation. The importance of these factors emphasizes the challenge presented by large continental deformation zones. The vast size, inaccessibility, and complexity of these regions suggest that debate over the processes governing plateau uplift and deformation will likely continue for some time. I hope that the work presented here will provide some insight into specific aspects of plateau development and contribute to a more complete understanding of continental deformation.